LIGHT SCATTERING STUDIES OF CLATHRATE HYDRATE FORMING SYSTEMS

By

RALPH KARL ZACHARY

A DISSERTATION PRESENTED TO THE GRADUATE SCHOOL
OF THE UNIVERSITY OF FLORIDA IN PARTIAL FULFILLMENT
OF THE REQUIREMENTS FOR THE DEGREE OF
DOCTOR OF PHILOSOPHY

UNIVERSITY OF FLORIDA

1998

Copyright 1998

by

Ralph Karl Zachary

ACKNOWLEDGMENTS

The author wishes to thank all of those who have contributed to his education at the University of Florida. He greatly appreciates the assistance and advice of his committee chair, Dr. Samuel Colgate, particularly with respect to the design and construction of the Raman scattering cell. The author has had the pleasure of having many enriching conversations with Dr. Colgate not only on matters of chemistry, but on topics ranging from the pleasures of bird-watching to the history of the arts and sciences.

Several past and current members of the Colgate research group also deserve thanks for their conversations and encouragement, particularly Vu Thieu, Johnny Evans, Troy Halvorsen, and Dan Tatro.

Dr. David Micha and the members of his research group, Dr. Keith Runge, Zhigang Yi, Dr. Herbert DaCosta, and Brian Thorndyke, have been very patient and helpful this past year. The author feels certain that they have underestimated their contribution to this project.

Although the final experimental results were obtained using a different instrument, Dr. Martin Vala graciously

offered the use of his lab’s instruments where several preliminary experiments were performed with the help of Dr. Jan Szczepanski.

Special thanks are owed to Dr. Kathryn Williams. She has been extremely generous with lab space and equipment, and even more so with her time. The author has learned a great deal from her while conducting the experiments described here and while assisting her with the physical chemistry and instrumental analysis teaching labs.

A list of all the ways in which Lori Clark has helped would double the length of this dissertation. The Physical Chemistry Division is truly fortunate to have such a competent and generous person on its staff and she will remain on this author’s Christmas list forever.

TABLE OF CONTENTS

ACKNOWLEDGMENTS iii

ABSTRACT vii

1. THE PHYSICAL CHEMISTRY OF CLATHRATE HYDRATES 1

Their Occurrence and Significance 1
Classification of Hydrates 4
Classification by Lattice Structure 4
Thermodynamic Classification 12
Guest Species of SI and SII Clathrate Hydrates . . . 14
The Dynamics of Hydrates 14
Lattice Dynamics 15
Guest Dynamics 20
Hysteresis and the Kinetics of Hydrate Formation 21
Specific Guests of Interest 26

2. LIGHT SCATTERING FROM MOLECULAR LIQUIDS 28

Introduction: Classical Theory of Light Scattering 28
Quantum Mechanical Treatment 32
Spectral Density and Polarizability Fluctuations . 37
Experimental Geometry and General Equations . 37
Special Cases of Interest 41
Models of Polarizability Fluctuations 46
Vibrational Motion: The Harmonic Approximation 46
Low Frequency Rotational and Translational Motion 51
Reduction Procedures and Relationships to Other Methods 57

EXPERIMENTAL DESIGN AND RESULTS 61

Raman Cell 61
Instrumentation and Computer Interface 72
Gases and Chemicals 81
Representative Spectra 82
Light Scattering from Water 82
The Water/THF system 85

MOLECULAR DYNAMICS SIMULATIONS 99

Software and Algorithms 99
Intermolecular Potentials 100
Cluster Simulation Details 104
Bulk Simulation Details 105
Spectral Calculations 107
Results 111

ANALYSIS AND DISCUSSION 117

The High Wavenumber Shift Region 117
Fitting Procedures 117
Spectral Features due to THF 117
Spectral Features due to Water 124
The Low Wavenumber Shift Region 128
Recomendations for Further Study 157

REFERENCES 165

BIOGRAPHICAL SKETCH 173

Abstract of Dissertation Presented to the Graduate School
of the University of Florida in Partial Fulfillment of the
Requirements for the Degree of Doctor of Philosophy

LIGHT SCATTERING STUDIES OF CLATHRATE HYDRATE FORMING SYSTEMS

By

Ralph Karl Zachary

May, 1998

Chairperson: Dr. Samuel O. Colgate
Major Department: Chemistry

The current importance of clathrate hydrates lies primarily in the problems they pose for the oil and gas industry; in the future they may represent an important source of energy. These studies were persued in an effort to determine the utility of light scattering for elucidating changes in the dynamical structure of aqueous solutions that occur prior to hydrate formation. Such an understanding has direct relevance to the kinetics of clathrate hydrate formation, and may contribute to our knowledge of the many other systems in which water plays an important role.

Aqueous solutions of tetrahydrofuran were at the center of this research which included experimental spectroscopic studies of such solutions as a function of temperature and system composition. Light scattering spectra were found to contain important information concerning the extent and nature of hydrogen bonding, and the structural changes that precede hydrate nucleation. Specifically, the OH stretching band due to water and the COC stretch band due to tetrahydrofuran were seen to vary in a predictable manner with changes in the composition, temperature, and thermal history of the system.

Computer simulation studies were performed and used to aid in the interpretation of experimental spectra. Low wavenumber polarizability fluctuations were calculated and found to give reorientation times in good agreement with those found using other methods.

CHAPTER 1
THE PHYSICAL CHEMISTRY OF CLATHRATE HYDRATES

Their Occurrence and Significance

A wide variety of chemical species interact with water at elevated pressures to form a class of solids known as clathrate hydrates. Though similar in appearance to ice, they are readily distinguished by their chemical and physical properties, particularly in their appearance well above the normal freezing point of water. The fundamental origin of these differences lies in the fact that hydrates possess two distinct kinds of chemical interactions: the ice-like water-water interactions of the lattice framework, dominated by hydrogen bonding, and water-guest interactions which are due almost entirely to van der Waals interactions[1].

Although this unusual combination of interactions makes hydrates interesting from a theoretical standpoint, current interest in their properties is primarily the result of their two-fold practical significance. First, several components of natural gas make excellent hydrate guests and the formation of solid hydrates in natural gas pipelines escalates transportation costs dramatically. Second, evidence is rapidly accumulating to suggest that naturally occuring hydrates represent a potentially enormous resevoir of natural gas[2]. In fact, recent geological surveys suggest that the total amount of oxidizable carbon trapped in naturally occuring hydrates may surpass the energy content of the total conventional fossil fuel reserves by as much as a factor of two[3-4].

The term "clathrate" was coined by Powell for "the structural combination of two substances which remain associated not through strong attractive forces but because strong mutual binding of the molecules of one sort makes possible the firm enclosure of the other."[5] In clathrate hydrates the lattice is composed of water molecules and they are bound to one another by hydrogen bonding.

Clathrate hydrates are thus distinct from other types of hydrates in that they are of the host-guest type. They may be distinguished further by the weakness of the interaction between guest and host, as opposed to the semi-clathrates which contain significant hydrogen-bonding interactions between guest and host, and as opposed to ionic hydrates with their large electrostatic interactions[6]. These distinctions are represented schematically in Figure 1-1.

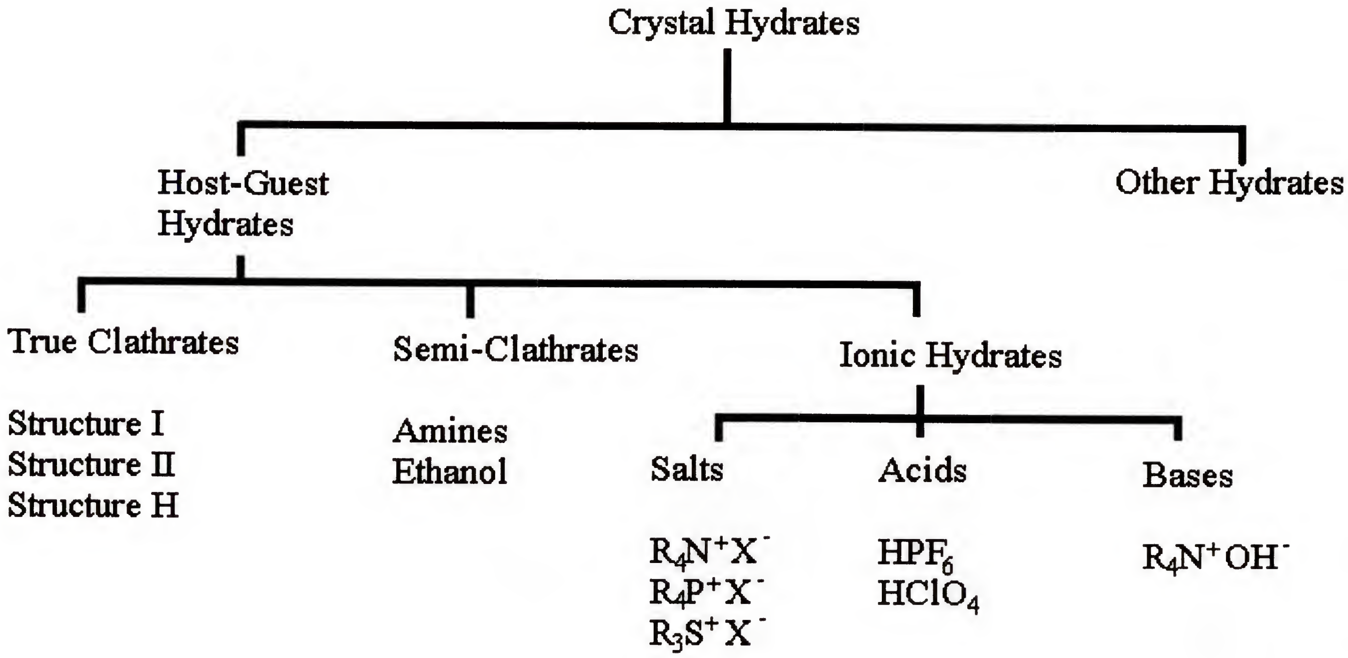

Figure 1-1. Schematic classification of hydrates.

Classification of Hydrates

Clathrate hydrates are classed among inclusion compounds, along with lemellar and channel structures. Structurally they consist of guest molecules trapped in cages of high symmetry which are formed by the host (water) lattice. Thermodynamically they may be viewed as solid solutions of guests within a host lattice. Although they are thus necessarily nonstoichiometric, the variation in guest stoichiometry is restricted to a range limited at one end by the minimum cage occupancy required for thermodynamic stability with respect to ice or aqueous solutions and, at the other end, by complete filling of the appropriately sized cages. This range is significant but rather narrow and complicated early efforts to characterize hydrates[7].

Clathrate hydrates have been classified according to the chemical nature of the guest species, by their thermodynamic properties, and by their crystalline structure. The weakness of the guest-host interaction suggests that the fundamental classification is according to the structure of the water lattice and so this approach will be described first.

Classification by Clathrate Structure

With only two exceptions, all known clathrate hydrates have water-lattices corresponding to one of three types denoted Structure I (SI), Structure II (SII), and the recently discovered Structure H (SH)[8-9]. Their geometry is characterized by specific combinations of nearly spherical voids. There are five types of these voids and all three structures contain pentagonal dodecahedra which, because they consist of 12 pentagonal faces, are frequently denoted 5^{12}. Structure I hydrates also contain tetrakaidecahedra, denoted $6^2 5^{12}$ to indicate their construction from two hexagonal and twelve pentagonal faces. The second cage type in Structure II is the hexakaidecahedron denoted $6^4 5^{12}$. Structure H consists of three cage types: pentagonal dodecahedra, the 20-hedron denoted $6^8 5^{12}$, and the 12-hedron $4^3 5^6 6^3$. The five cage types are illustrated in Figure 1-2 and their geometric properties summarized in Table 1-1.

The water lattice of Structure I hydrates is body-centered cubic and belongs to the space group Pm3n. The unit cell dimension is typically 12 Å and does not vary significantly with variations in the guest molecule. A single unit cell has the formula $2M_1 \bullet 6M_2 \bullet 46\ H_2O$, where M_1 and M_2 refer to the 5^{12} and $5^{12}6^2$ cavities, respectively.

Structure II hydrates posses a diamond cubic water lattice that belongs to the space group Fd3m. Typical cell dimensions are 17 Å on a side and, again, do not depend strongly on the nature of the guest. The unit cell has the formula $16M_1 \bullet 8M_3 \bullet 136\ H_2O$, with M_1 and M_3 the 5^{12} and $5^{12}6^4$ cages, respectively.

Table 1-1. Cavities occuring in clathrate hydrates

Cavity Type	5^{12}	$5^{12}6^2$	$5^{12}6^4$	$4^35^66^3$	$5^{12}6^8$
Average Cavity Radius, Å	3.90	4.33	4.68	4.06	5.71
Coordination Number	20	24	28	20	36
Cavities/ Unit Cell (SI)	2	6	---	---	---
Cavities/ Unit Cell (SII)	16	---	8	---	---
Cavities/ Unit Cell (SH)	3	---	---	2	1

Table 1-2. Properties of the Water Lattices in Clathrates

Structure	I	II
Crystal System	Cubic	Cubic
Space Group	Pm3n (#223)	Fd3m (#227)
Lattice Description	Body Centered	Diamond
Lattice Parameter,	12	17.3
Ideal Unit Cell Formula	$2M_1 \bullet 6M_2 \bullet\ 46\ H_2O$	$16M_1 \bullet 8M_3 \bullet 136\ H_2O$

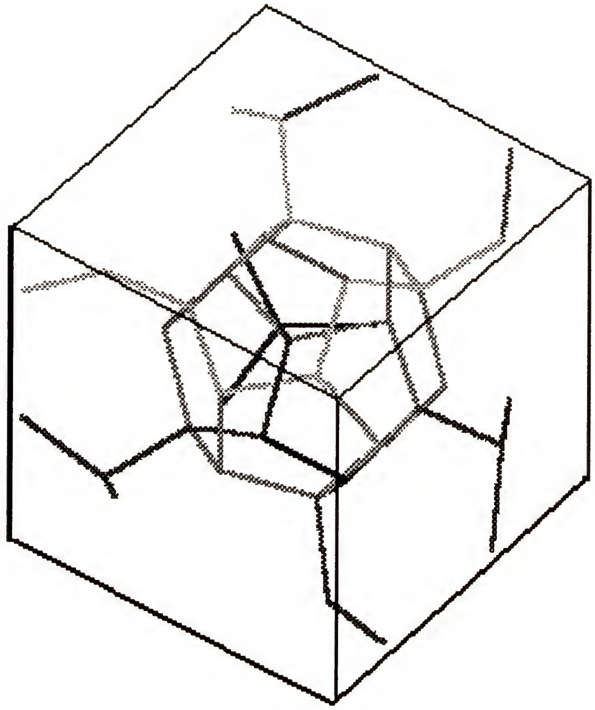

Figure 1-3(a). The SI unit cell.

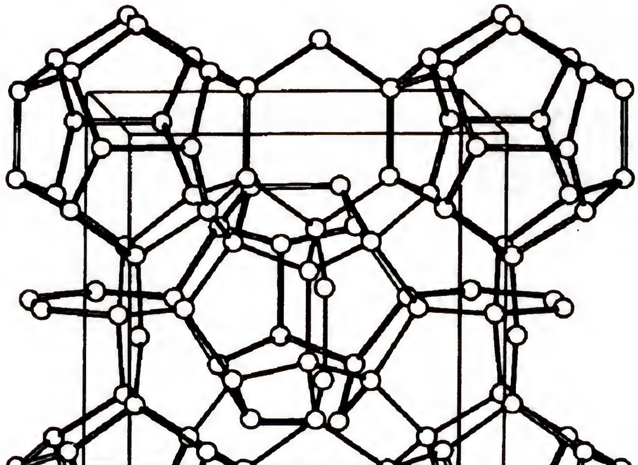

Figure 1-3(b). Projection of the SI lattice.

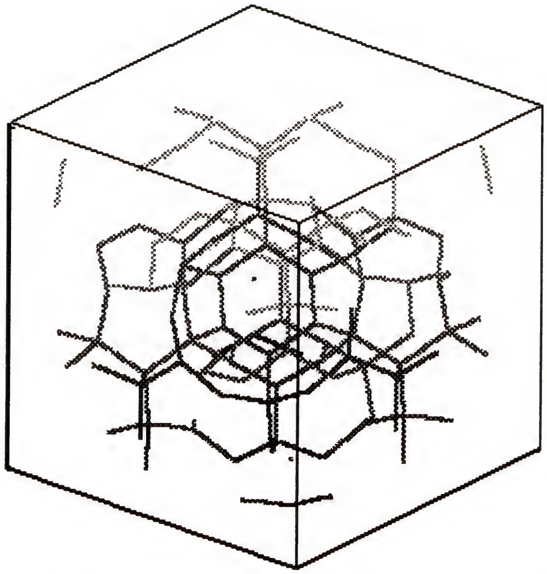

Figure 1-3(a). The SII unit cell.

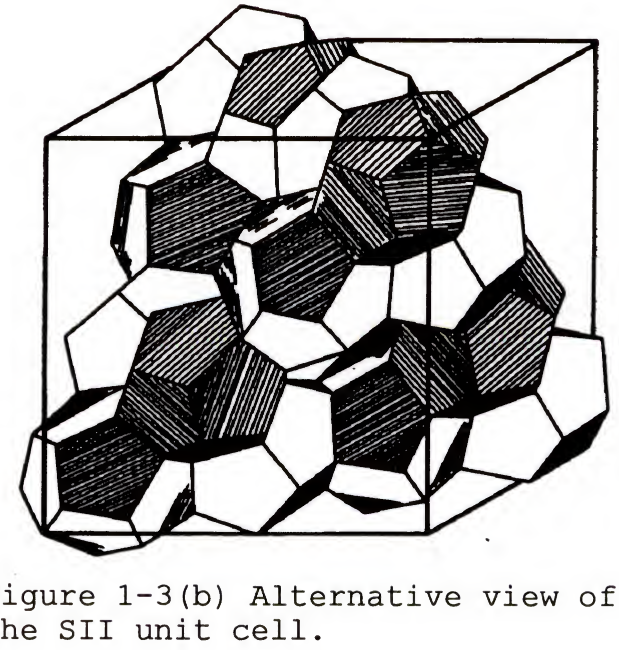

Figure 1-3(b) Alternative view of the SII unit cell.

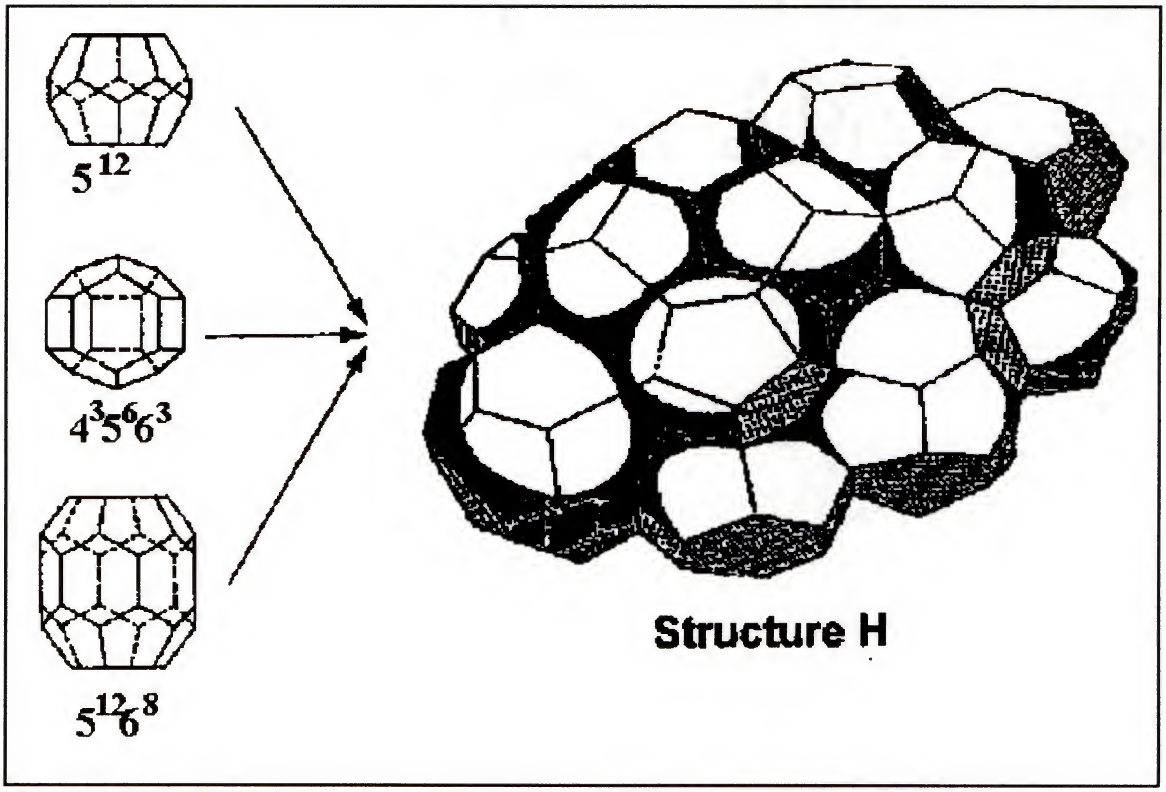

Figure 1-5. The Structure H unit cell.

Structure H hydrates have only recently been discovered and contain a water lattice which is hexagonal in symmetry. The unit cell has the formula $3M_1{\bullet}2M_4{\bullet}M_5{\bullet}34H_2O$ where M_1, M_4, and M_5 are the 5^{12}, $4^35^66^3$ and $5^{12}6^8$ cavities respectively. Structure H hydrates are of only incidental interest to this study.

The unit cells of the three hydrate types are illustrated in figures 1-3, 1-4, and 1-5. Several of their more important features are summarized in Table 1-2.

Clathrate hydrates resemble ice to the naked eye and do so at the molecular level in the sense that each water molecule is hydrogen-bonded to four nearest neighbors, as in all the known forms of ice. The guest molecules play a stabilizing and space-filling role which does not depend strongly on their identity. The average departure of O-O-O angles from the tetrahedral values found in ices I_h and I_c is only 3.7° and 3.0° in structures I and II respectively. This is in contrast to the rather large deviations found in the high-pressure ices II, III, V and VI. The O-O bond lengths on average exceed those in hexagonal ice, where they are 2.76 Å, by only 1% and are comparable to those in most of the other forms of ice[10-11].

Aside from the cages, the most obvious structural feature distinguishing clathrates from the various forms of ice is the predominance of planar (structure II) or nearly planar (structure I) five-membered rings. The less numerous pentagons which occur in ice IX and III are far from planar. The hexagonal rings are also planar in structure I or very nearly so in the case of structure II. This is in marked contrast to the puckered hexagons found in other forms of ice. This planarity means that the three water molecules hydrogen-bonded to the molecule at each end of a hydrogen bond are eclipsed when viewed along that bond, or, to use Bjerrum's terminology, that the arrangement about the bond is mirror symmetric (*ms*). In cubic ice I_c, and probably in ices VII and VIII, the orientations about all bonds are staggered or trans in a center symmetric (*cs*) arrangement. This is the case in ice I_h, except for one-fourth of the bonds, those which lie parallel to the c axis, and about which the arrangement is also *ms*[12].

Bjerrum's analysis hypothesized that the *ms* arrangement was more stable than the *cs* but that it was probably not possible to construct a crystal in which more than one-fourth of the bonds were of the *ms* type. The requirements of ring and cage closure produce some distortions of most bonds in clathrate hydrates from the ideal tetrahedral ms arrangements found around c bonds in I_h. This distortion of angles and bond lengths and the weaker attractive forces between nonbonded neighbors, rather than any fundamental instability of *ms* with respect to *cs* bonding, is what accounts for the low stability of the empty clathrate hydrate lattices with respect to I_h[13].

Pentagonal rings outnumber hexagonal rings in a ratio of 8:1 in structure I and 9:1 in structure II. Both are close to the ratio of 8.62:1 which would make the average angle tetrahedral if all faces were exactly planar. The departures from planarity which do occur are in the direction of equalization of hydrogen bond lengths throughout the structures.

Thermodynamic Classification

A second scheme for the classification of clathrate hydrates is based on the phase behavior of hydrate-forming systems. It is a convenient way of describing the conditions under which a hydrate is stable. Most hydrate forming systems have a phase diagram similar to that of SO_2/H_2O illustrated in figure 1-6 in which h stands for hydrate, g for gas, I for ice, l_1 for the liquid phase rich in water and l_2 the liquid phase rich in hydrate former. Systems with such a diagram are denoted i_2. The region of hydrate stability is bounded by the h-I-g, h-l_1-g and h-l_1-l_2 equilibrium lines[14].

Two invariant points Q_1 and Q_2 mark the coexistence of h, I, l_1, and g on the one hand and of h, l_1, l_2 and g on the other. This phase behavior reflects the sparing solubility of most hydrate-formers in water and such systems are characterized by the temperatures and total pressures at the quadruple points Q_1 and Q_2.

Among the guests which form i_2 systems are the SI formers Cl_2, CO_2, N_2O, H_2S, SO_2, PH_3, AsH_3, C_2H_2, C_2H_6, and CH_3Cl. SII formers include SF_6, C_3H_8, iso-butane, cyclopentene, cyclopentane, and CH_2Cl_2.

The Q_2 point is absent for light gases whose h-l_2-g equilibrium line ends at the l_2-g critical point in the presence of hydrate before it intersects the h-l_1-g. Such systems are denoted i_1, and in them hydrate may exist to indefinitely high temperatures so long as a pressure is maintained that is at least equal to the steeply rising decomposition pressure.

The most important species forming i_1 systems with water all form SI hydrates and include the noble gases Ar, Kr, and Xe in addition to N_2, O_2, CH_3, and C_2H_4.

If the guest species is sufficiently soluble in water there is only one liquid phase and the quadruple point Q_2 is absent. For some hydrates it is replaced (as the maximum temperature of coexistence of hydrate, liquid, and gas) by the congruent melting point. The phase relationships in such a case are more conveniently shown in the temperature-composition projection of the phase diagram. In figure 1-7 such a project is shown for the SI forming ethylene-oxide water system[15].

Guest Species of SI and SII Clathrate Hydrates

Some 100 chemical species are known to form clathrate hydrates. Suitability of a guest is determined primarily by its size: its molecules must be small enough to be contained by the cages available in a particular hydrate structure. The chemical identity of the species is relevant only in so far as the molecules must not contain moieties leading to covalent or ionic bonding with water.

While each cage of a hydrate may contain no more than one guest, they need not necessarily all contain the same kind of guest. This leads to the distinction between simple hydrates,those containing only one type of guest, and the more complex double- and mixed-hydrates[16]. In the latter, the various guest species occupy cages of all available types while in the former guest species of a particular type are found only in one type of cage.

The Dynamics of Hydrates

In the years which immediately followed the 1811 discovery of hydrates by Sir Humphrey Davy[17], most research in the field was devoted to the determination of the composition of various hydrates. This was followed by a period of intense interest in the structure characteristics of clathrates and the phase behavior of clathrate-forming systems[18]. Research along these lines lead to the formulation of an elegant statistical mechanical model of hydrates by van der Waals and Platteeuw[19-20]; a model that has been particularly useful for the oil and gas industry in their efforts to predict the thermodynamic conditions conducive to hydrate formation. Recently interest has shifted toward a more detailed study of the dynamics of hydrates, and into the kinetics of their formation.

Lattice Dynamics

In common with hexagonal ice, and the other disordered forms of ice, the orientational disorder of the water molecules in clathrate hydrates manifests itself in a rotational mobility affecting the dielectric and nuclear magnetic resonance properties at relatively high temperatures[21]. Reorientations of the water molecules result in interchanges among the ~(3/2)N lattice configurations until the temperature becomes so low that the rate of interchange is negligible and the configurational disorder, with its corresponding residual entropy, is "frozen-in."

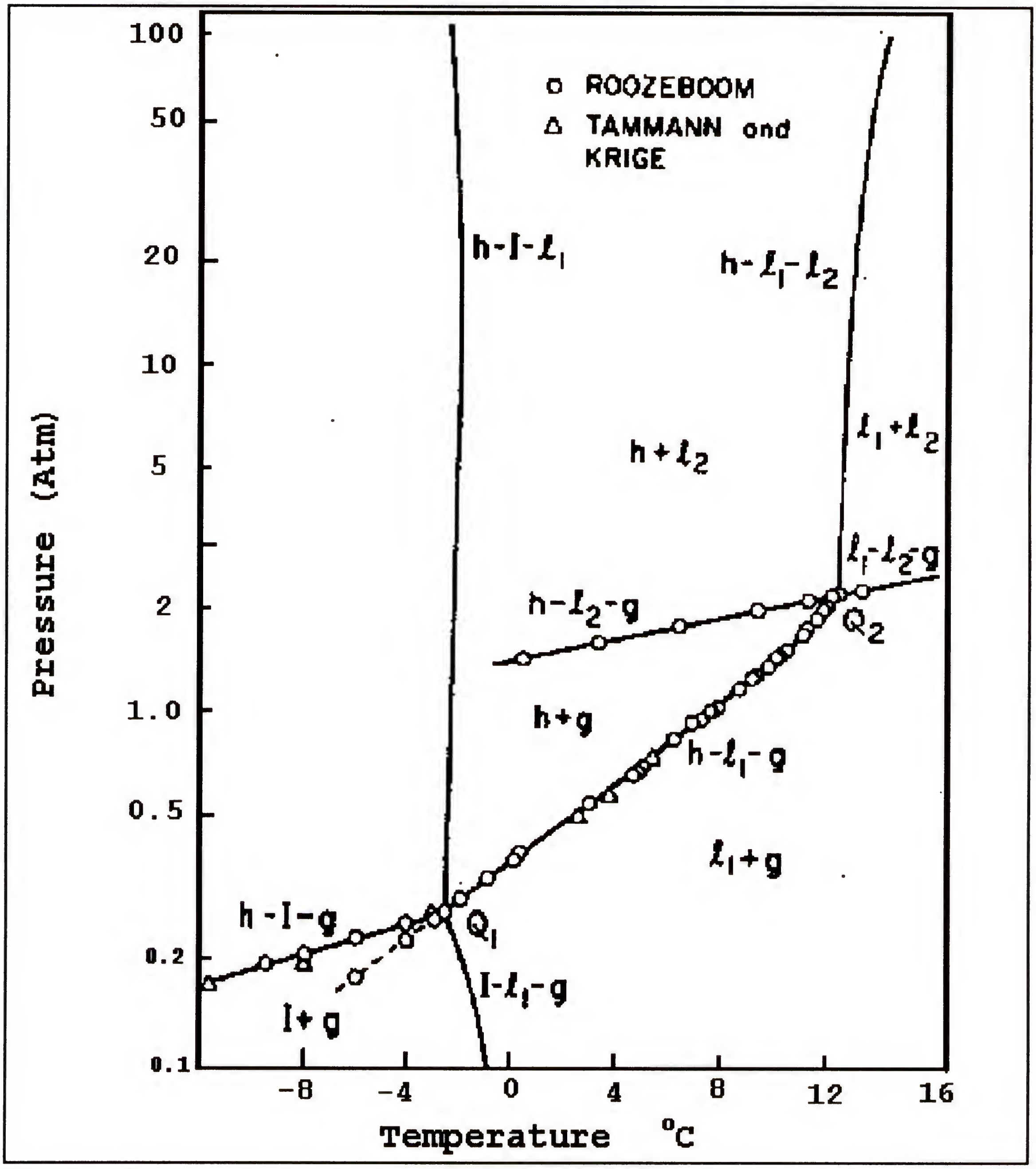

Figure 1-6. Typical phase diagram of an i_2 type hydrate-forming system (SO_2/H_2O).

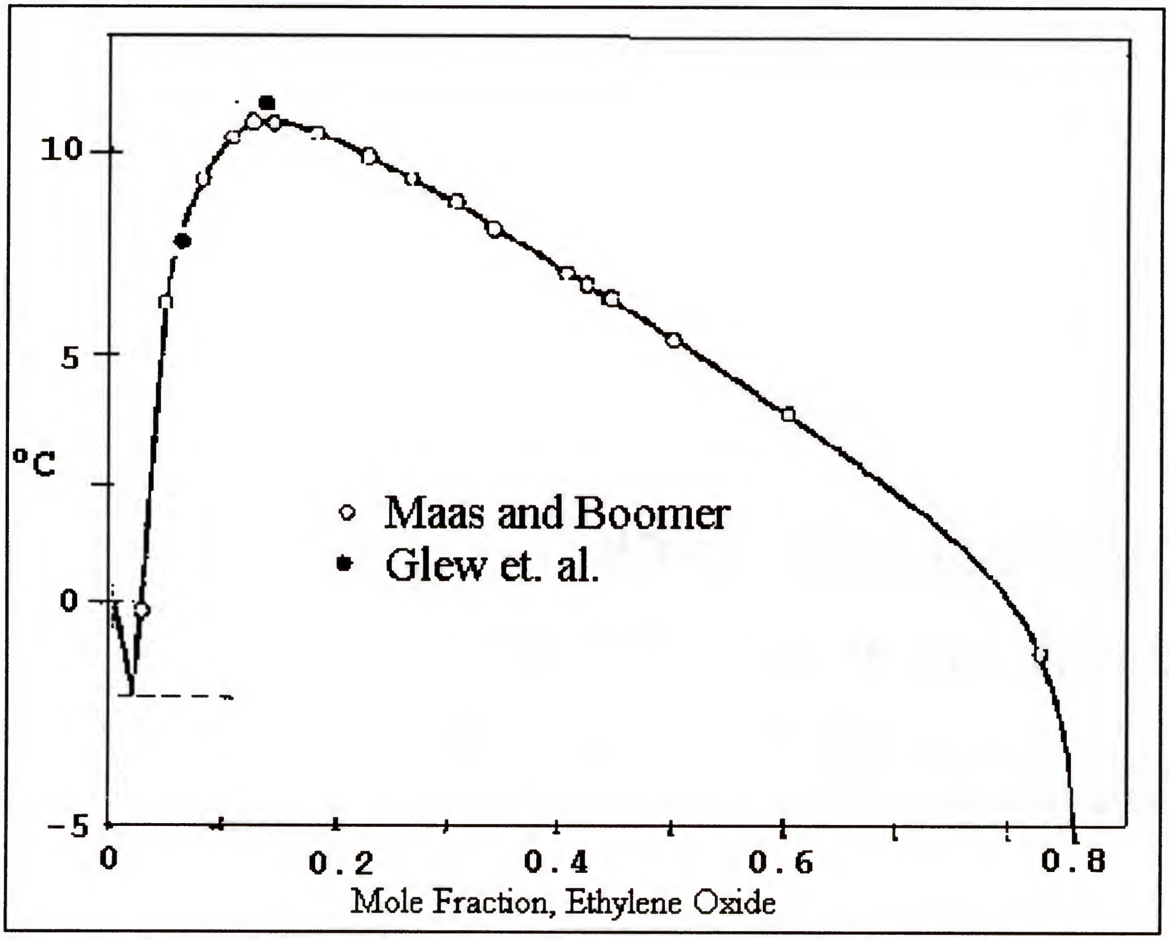

Figure 1-7. Typical phase diagram for a system containing a water soluble hydrate former.

Dielectric measurements, in particular, suggest significant dynamical differences between the ices and clathrate hydrates. The Cole-Cole complex permittivity locus of ice I_h is accurately a semi-circle; i.e., reorientation of the water molecules occurs with a single relaxation time[22]. The temperature dependence of this reorientation time follows Arhenius-like behavior with an activation energy of approximately 13.2 kcal mol^{-1}. The classic analysis of the dielectric properties of ice by Bjerrum models the reorientation of water molecules in the ice lattice as the diffusion of defects originating instrisically from thermal excitation[23].

In contrast, the structure II hydrates have a complex permitivity locus described in terms of a spread of relaxation times about τ_0, the most probable relaxation time, described quantitatively by the parameter α in

$$\epsilon^* = \epsilon' - i\epsilon'' = \epsilon_{\infty 1} + (\epsilon_0 - \epsilon_{\infty 1})/[1 + (i\omega\tau_0)^{1-\alpha}] \qquad [1\text{-}1]$$

In the case of ice I_h, $\alpha = 0$.

Furthermore, denoting the thermodynamic temperature by T, the 1/T dependence of log τ_0 deviates significantly from linearity which is probably due to the increasing predominance at low temperatures of relaxation controlled by Bjerrum defects of extrinsic origin. Although there appears to be a loose correlation of τ_0 with guest polarity, the correlation is not close, suggesting that these differences must be, at least in part, attributed to differences between the water lattices in ice and in clathrates[24].

Results from both proton nuclear magnetic resonance (NMR) spectra and dielectric measurements indicate a second characteristic distinguishing the dynamics of water molecules in ice from their motion in hydrates[25]. In addition to the multiplicity of relaxation processes present in hydrate lattices and discussed above, the rates of water reorientation differ greatly in the two environments. Though hydrate water molecules reorient rapidly relative to molecules in other solids, those reorientation rates are only one-half those in ice.

This difference is particularly significant in that it changes the dynamic relationship between rotation and translation in hydrates. Water molecules in ice diffuse almost an order of magnitude faster than they reorient about a fixed position in the crystal structure. Water molecules in the hydrate lattice reorient 20 times faster than they diffuse[26].

What remains in dispute is the magnitude and kind of influence exerted by the guest molecules over the rotational and translational motion of water in hydrate lattices. Proton NMR studies aimed at elucidating the motion of the guests do not yield evidence of hydrogen bonding, while dielectric studies seem to imply the occasional formation of hydrogen bonds between guest and host molecules so as to inject Bjerrum defects of a specific type into the lattice.

These two methods seem incapable of resolving the dispute since the extent of hydrogen bonding would presumably have to exceed several percent for it to be readily detected by proton NMR, while the dielectric relaxation behavior can be accounted for by supposing only a small fraction of guests to be hydrogen bonded ($\sim 2 \times 10^{-6}$)[27].

Guest Dynamics

What is not in dispute, and which is in distinct contrast to other solid systems, is the remarkable degree of rotational mobility of the guest species. The permittivity measured on the high-frequency side of the dispersion region associated with reorientation of the water molecules reaches a limiting value $e_{\infty 1}$ which depends on the nature of the guest molecule and on the temperature. This limiting value, as measured for structure II hydrates at a fixed, relatively high temperature, is very nearly proportional to the square of the guest molecule's dipole moment. Above about 150 K the value varies linearly with 1/T for most hydrates. Taken together these observations indicate that the guest molecules are undergoing reorientation at rates considerably in excess of the frequencies of the measurements, ~1 MHz, either isotropically or between two or more preferred orientations of similar energy.

A study of the dielectric absorption associated with reorientation of the guest molecules in the hydrates of ethylene oxide, tetrahydrofuran, and acetone gave estimated relaxation times on the order of about 10^{-11} sec at 90 K. The Eyring activation energies (E_A - RT) were estimated at 0.5 kcal mol^{-1} for ethylene- oxide hydrate and 0.3 kcal mol^{-1} for the structure II hydrates.

Also relevant is the observation that, within each structure type, the relaxation rate of the guest decreases and the activation energy increases with increase in size of the guest molecule[28].

Hysteresis and the Kinetics of Hydrate Formation

An important feature of hydrate-forming systems, and one that has plagued efforts to study their phase behavior, is the extreme hysteresis and metastability found in such systems. This feature complicates the precise determination of phase boundaries and renders ambiguous the results from different laboratories.

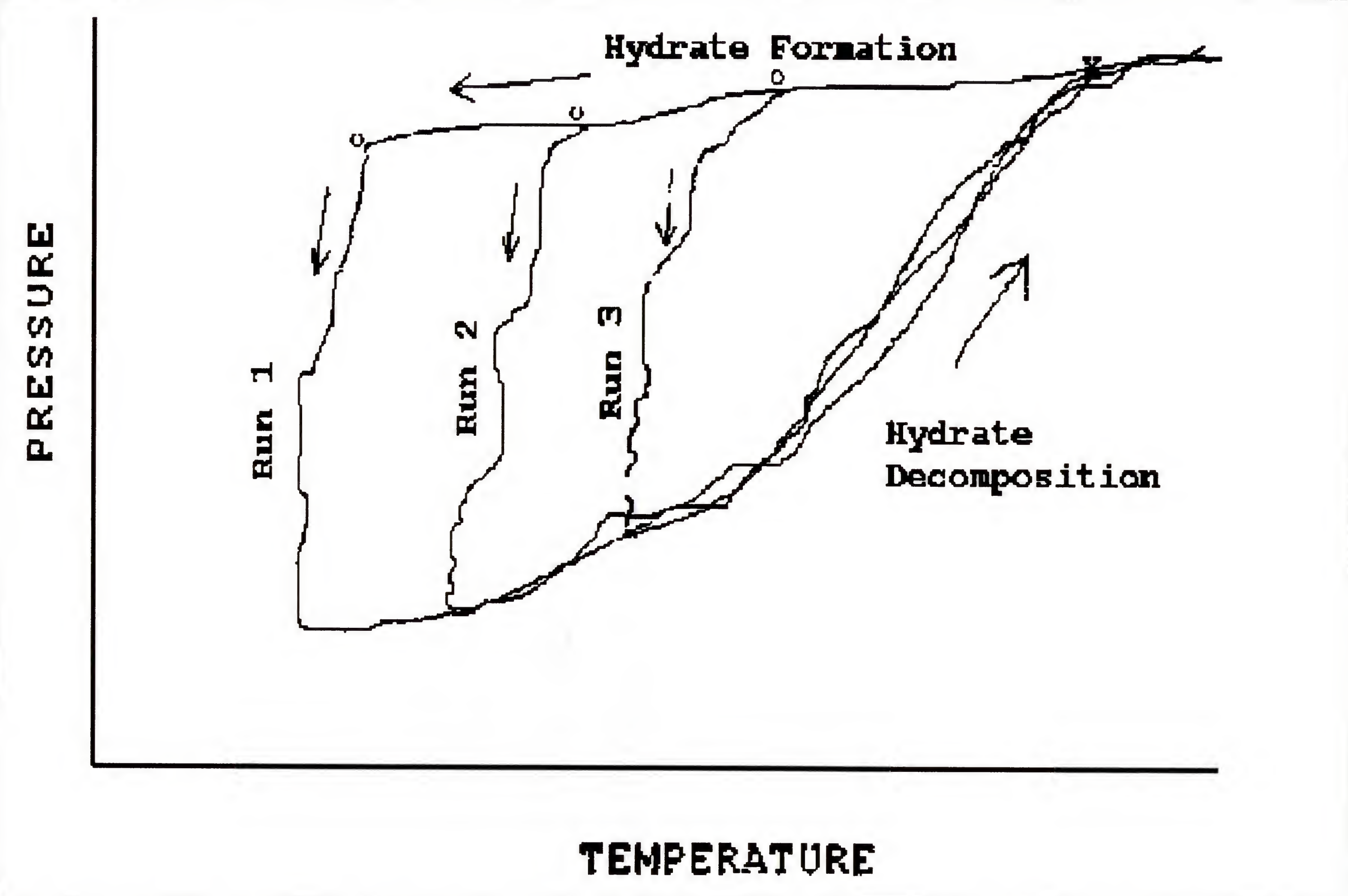

Figure 1-8. Plot of pressure versus temperature for a typical hydrate formation experiment.

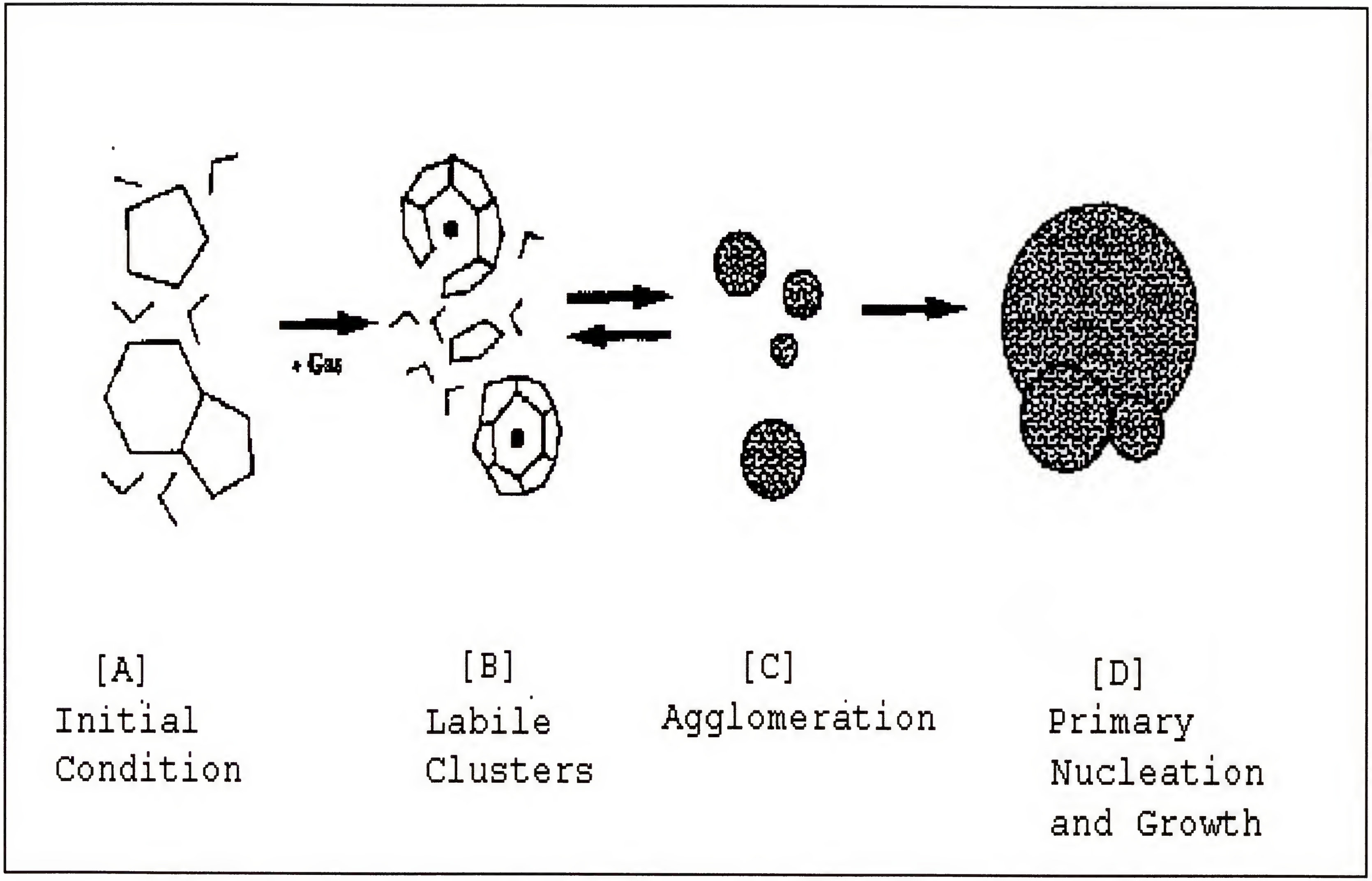

Figure 1-9. Overview of a proposed hydrate formation process.

In figure 1-8 the hysteresis effect is apparent in the isochoric pressure trace of a hydrate formation and hydrate decomposition cycles[29]. The cycle begins with cooling of a hydrate cell containing methane gas and water. The letter O on the plot indicates the start of hydrate formation which was accompanied by a sharp drop in the total pressure. After hydrate ceased to form the temperature of the sample was increased until hydrate decomposition is complete, marked by an X on the plot. The system was then cooled again and it was found that with each successive cooling run of the sample, the temperature at which hydrate formation begins was higher than in the previous trial. Results such as these have been offered as evidence for the existence of metastable hydrate precursors at temperatures well above the ostensible hydrate decomposition temperature.

In common with crystallization, the hydrate formation process may be divided into nucleation and growth phases. In the nucleation or induction phase, hydrate precursors form and disperse within a supersaturated aqueous solution. If these precursors manage to grow to a critical size, the second phase begins and the hydrate nuclei quickly grow into solid crystals. The system's history exerts a powerful influence over the length of the induction time. This complication is largely responsible for the shortage of reliable quantitative kinetic data available for the induction period[30].

Figure 1-9 outlines a hydrate formation hypothesis offered by Sloan[31] in which species are seen to progress from water and small water clusters [A] through labile clusters [B] to metastable agglomerates [C] to stable nuclei [D] which marks the end of the nucleation period and beginning of the rapid growth process.

Heating of such a system will drive the process in reverse and the stable hydrate crystals will dissociate. Yet the evidence suggests that microscopic species, ranging in size from a single labile cluster [B] to agglomerates[C], persist in the solution to temperatures up to about 20 K above the temperature at which bulk hydrate disappears.

What is missing from this hypothesis is a more detailed description of the clusters responsible for the metastability of hydrate forming systems. Research directed along these lines is in its infancy and consists almost exclusively of preliminary NMR and dielectric measurements. The discussion of lattice and guest dynamics given earlier suggests that these techniques will necessarily give an incomplete picture of the relevant dynamic processes and need to be supplemented by other methods.

One class of methods sensitive to the dynamics of liquids concerns the measurement of scattered light. Although the related technique of infrared spectroscopy has been used in the analysis of hydrates, these studies were restricted to solid hydrates[32], solid ice[33], pure water[34], or to the equilibrium properties of aqueous solutions not necessarily relevant to hydrates[35].

There are two published reports in the literature of Raman scattering from solid hydrates[36] and their results are briefly discussed in Chapter 5, but the focus in those studies was on the pressure dependence of certain structural features of hydrates. More relevant are the numerous studies of light scattering from pure water, and from aqueous solutions not involved in hydrate formation, those results will be discussed in more detail in Chapter 5. These pages describe the first known attempt to apply the insights obtained from such studies to hydrate-forming aqueous solutions.

Specific Guests of Interest

Three guest molecules figure prominently in the studies reported here and their chemical structures are given in Figure 1-10. The first, methane, is an important component of natural gas and its simple, tetrahedral geometry makes it convenient for modeling hydrate properties. The methane hydrate has a lattice structure corresponding to Structure I and forms at a temperature of -78.7 °C, at 1 atmosphere pressure[14].

Ethylene oxide, or oxirane, is a gas at ordinary temperatures and pressures and it also forms a Structure I hydrate[14]. Its phase diagram is characterized by a lower quadruple point at -2.1 °C and 1 atmosphere pressure.

A larger cyclic ether, tetrahydrofuran, was chosen for contrast with ethylene oxide. Tetrahydrofuran combines withwater to form a Structure II hydrate at 4.3 °C and 1 atmosphere pressure. It is a liquid at room temperature and totally miscible in water.

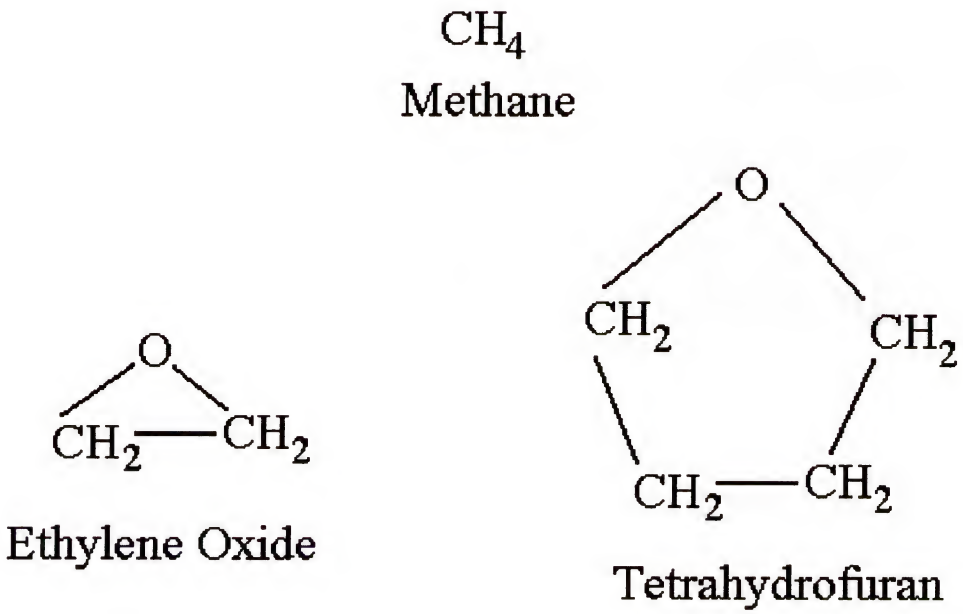

Figure 1-10. Hydrate guests of special interest.

CHAPTER 2
LIGHT SCATTERING FROM MOLECULAR LIQUIDS

Introduction: Classical Theory of Light Scattering

Although a complete description of the interaction of light with matter requires a quantum mechanical treatment, the modern understanding of light scattering can be said to date from Lord Rayleigh's description of the central role played by polarizability fluctuations. With the development of kinetic-molecular theory a classical, yet molecular, theory of light scattering emerged. This led to Lommel's prediction of inelastic light scattering, and the first quantum mechanical treatment by Smekal. The effect was observed experimentally by C. V. Raman and K. S. Krishnan in liquids and, simultaneously, by G. S. Landsberg and L. I. Mandelstam in crystals though neither experimental team was aware of the theoretical predictions[37].

The insight provided by classical theory is sufficiently valuable to warrant a brief review of its essentials. The discussion will be limited to what is sometimes described as "spontaneous" light scattering to distinguish it from resonant and nonlinear phenomena[38-39].

Consider an individual molecule subject to an incident light wave described by, $\mathbf{E} = \mathbf{E_0} \cos 2\pi\nu_0 t$. The dipole moment, μ, induced by this external electromagnetic field is given by,

$$\mu = \alpha \boldsymbol{E} \qquad [2\text{-}1]$$

Where α is the molecular polarizability and, in the general case, is a tensorial quantity. In this section it will be assumed that the electric field and induced dipole moment are parallel to one another such that these three quantities may be treated as scalars.

Continuing with the classical approach, suppose the polarizability is a phenomenological quantity which depends on the distances between the atomic nuclei at any given moment. Denoting by q_v the coordinate describing a particular vibrational mode of the molecule, we may write $\alpha = \alpha(q_v)$. If the displacement is small, the polarizability can be expanded in a power series in q_v around the equilibrium value of this coordinate, $q_v = 0$. That is, we may write

$$\alpha(q_v) = \alpha_0 + \left(\frac{\partial\alpha}{\partial q_v}\right)_0 q_v + \ldots \qquad [2\text{-}2]$$

After substituting $q_v = q_{v0} \sin(2\pi\nu t)$ we have,

$$\alpha(t) = \alpha_o + \alpha_v \cos 2\pi\nu_v t \qquad [2\text{-}3]$$

The expression for the dipole moment becomes,

$$\mu(t) = \alpha_0 E_0 \cos 2\pi\nu_0 t + \alpha_v E_o \cos 2\pi\nu_0 t \cos 2\pi\nu_v t \qquad [2-4]$$

or equivalently,

$$\mu(t) = \alpha_0 E_0 \cos 2\pi\nu_0 t + \frac{\alpha_v E_0}{2} [\cos 2\pi(\nu_0 - \nu_v) t + \cos 2\pi(\nu_0 + \nu_v) t] \qquad [2-5]$$

The significance of this time varying dipole can also be understood within the classical framework since classical electromagnetic theory holds that such a dipole will emit light of the same frequency.

Several important features of light scattering are already apparent even in this minimal treatment. First, the scattered light is a result of forced oscillations of the molecular dipole moment induced by the electromagnetic field of the incident light wave. Rayleigh scattering, represented by the first term of equation 2-5, which consists of light of unaltered frequency, is due to the unperturbed polarizability of the molecule.

Furthermore, we may anticipate the results of the quantum mechanical treatment, by inferring the general features of Raman scattering from the remaining two terms in equation 2-5. The light is primarily scattered by the electronic properties of the molecule and the atomic nuclei are displaced only slightly. The deformability of the electron cloud in the imposed electric field depends on the nuclear configuration at any given moment. As the nuclei oscillate about their respective equilibrium positions, the deformability of the electron cloud varies with the oscillation frequency of the nuclei. On the other hand, deformation of the electron cloud may induce vibration of the nuclei.

The classical treatment correctly predicts that the intensity of the Raman scattering lines is proportional to the square of the derivative of polarizability with respect to the vibrational coordinate[38]. If higher terms in the expansion 2-2 are taken into consideration, the intensities of overtones and combination frequencies can be similarly related to the squares of the higher derivatives.

The Raman shift is $\Delta\nu = \nu_0 - \nu_{scat} = \pm\nu_v$ and, because it is a property of the molecule independent of the incident light's frequency, ν_0, it is treated as the independent variable. At this point a potentially confusing feature of the literature should be mentioned: the Raman shift is almost universally reported as the wavenumber shift, $\Delta\tilde{\nu} = \Delta\nu/c$, but it is often denoted simply ν or ω and, even more unfortunately, is often referred to as "frequency." These pages will reserve ω for angular frequency, ν for frequency, and $\tilde{\nu}$ for wavenumber.

The origin of light scattering may derive from the translational or rotational motion of molecules to the much faster (and higher energy) vibrational motion of nuclei within a molecule and these modes of motion are traditionally treated using different techniques. What these techniques share is a common focus on the fluctuation of the system's polarizability. Detailed treatment of these different techniques will be postponed until after a brief description of the polarizability of a molecule.

Quantum Mechanical Treatment: the Placzek Approximations[40]

Prior to its being perturbed by incident light, an independent molecule exists in one of the stationary states |l> specified by,

$$\hat{H}_0 \, |l\rangle = \epsilon_l \, |l\rangle, \qquad l = 1,2,3... \qquad [2\text{-}6]$$

The introduction of a time varying electromagnetic field, $\mathbf{E}(t) = \mathbf{E}^+ e^{i\omega 0t} + \mathbf{E}^- e^{-i\omega 0t}$, induces the system to undergo a transition to a time dependent state $\psi_l(t)$ which satisfies,

$$[\hat{H}_o - \hat{\boldsymbol{D}}\cdot\boldsymbol{E}(t)]\,|\psi_l(t)\rangle = i\hbar\frac{\partial}{\partial t}\,|\psi_l(t)\rangle \qquad [2\text{-}7]$$

Here, **D** is the dipole moment operator. The time dependent states may be written,

$$|\psi_l(t)\rangle = (\,|l\rangle + |\phi_l^+\rangle)\,e^{i\omega_0 t} + (\,|l\rangle + |\phi_l^-\rangle)\,e^{-i\omega_0 t} \qquad [2\text{-}8]$$

where the states $|\phi^{\pm}\rangle$ are time independent. A relatively simple result is obtained if one neglects terms higher than first order in **E**, uses the completeness of the set of stationary states, and assumes that the laser frequency, ω_0, is not too close to the frequency of transition ω_{ml}:

$$|\psi_l(t)\rangle = \sum_m |m\rangle \frac{\langle m|\,[\hat{\boldsymbol{D}}\cdot\boldsymbol{E}(t)\,|l\rangle}{\hbar(\omega_{ml} \pm \omega_0)} \qquad \omega_{ml} = \frac{\epsilon_m - \epsilon_l}{\hbar} \qquad [2\text{-}9]$$

The shift in frequency characterizing Raman scattering is due to transitions between two quantum stationary states. The induced-transition dipole involved in Raman scattering associated with a transition from state |l> to state |m> is obtained from,

$$\boldsymbol{D}^{ml}(t) = \langle\psi_m(t)|\;\hat{\boldsymbol{D}}\;|\psi_l(t)\rangle \qquad [2\text{-}10]$$

After neglecting the part of the dipole moment responsible for the spontaneous emission, we can see that the jth Cartesian component of the induced dipole associated with this transition is given by, to first order in the electric field,

$$D_j^{ml}(t) = \sum_k [\alpha_{jk}^{ml}(\omega_0)\; E_k^{+}\; e^{i(\omega_0+\omega_{ml})t} + [\alpha_{jk}^{ml}(\omega_0)]^{*}\; E_k^{-}\; e^{-i(\omega_0+\omega_{ml})t}\;] \qquad [2\text{-}11]$$

In equation 2-11, $\alpha^{ml}{}_{jk}(\omega_0)$ is the jk component of the polarizability tensor found from:

$$\alpha^{ml}_{jk}(\omega_0) = \sum_n \left(\frac{<m|D_j|n><n|D_k|l>}{\hbar(\omega_{nl} + \omega_0)} + \frac{<m|D_j|n><n|D_k|l>}{\hbar(\omega_{nm} + \omega_0)} \right) \qquad [2\text{-}12]$$

In equation 2-12, the case where $\omega_{ml} < 0$ corresponds to Stokes scattering, whereas $\omega_{ml} > 0$ corresponds to anti-Stokes scattering.

The intensity of the scattered light is obtained by substituting the induced transition dipole moment into Maxwell's equations and then solving the resulting inhmogenous wave equation. For incident laser light polarized along the k direction, and scattered light observed in the j direction of polarization, the result is:

$$I^{ml}_{jk}(\omega) = \frac{I_0 \omega^4}{4c^4} |\alpha^{ml}_{jk}(\omega_0)|^2 \, \delta(\omega - \omega_0 - \omega_{ml}) \qquad [2\text{-}13]$$

in which I_0 is the incident intensity given by,

$$I_0 = \left(\frac{c}{2\Pi}\right) E_j^+ E_j^- \qquad [2\text{-}14]$$

Although this result is general, it is not convenient for the description of scattering from molecules.

When the transition frequencies for electronic motion are large compared to the separation in vibrational or rotational energies, the approximations introduced by Placzek[39] are appropriate and transform this into a form suitable for the study of vibrational, rotational, and translational motions for many molecular system.

Placzek theory assumes that the adiabatic approximation is valid, and that the molecule is in its (nondegenerate) ground electronic state before and after interaction with incident radiation.

The adiabatic approximation permits[47] us to write the wave function of stationary state |1> in a form that separates nuclear from electronic motion:

$$\psi_{l}(\boldsymbol{x},\boldsymbol{X}^{\mathbf{a}}) = \phi_{l}(\boldsymbol{x};\boldsymbol{X})\,\xi_{la}(\boldsymbol{X}) \qquad [2\text{-}15]$$

Here $\mathbf{x}$ and $\mathbf{X}$ refer to the electronic and nuclear coordinates, respectively; $\phi_1(\mathbf{x};\mathbf{X})$ is the electronic wave function with nuclei fixed in a configuration specified by $\mathbf{X}$; and $\xi_{1a}(\mathbf{X})$ is the nuclear wave function for nuclei in the state specified by the vibrational and rotational quantum numbers collectively represented by a, and in which the electronic state of the molecule is 1.

The energy associated with state |1> is found to be

$$\varepsilon_{la} = \varepsilon_{l}^{0} + W_{la} = \varepsilon_{la}(\boldsymbol{X}) \qquad [2\text{-}16]$$

in which ε_1^0 is the eigenenergy of the electrons with nuclei fixed in the configuration **X** and W_{1a} is the eigenenergy associated with the wave function $\xi_{1a}(\mathbf{X})$.

We may now take advantage of the second approximation, and set the initial state $|1>$ to be $|ga>$ and the final state $|m>$ to be $|gb>$. That is, we have explicitely labeled the ground electronic state by g and have chosen a and b to label sets of quantum numbers describing the state of nuclear motion. Then the expression for the relevant polarizability is given by,

$$\alpha_{jk}^{ba}(\boldsymbol{X}) = \sum_f \frac{<gb|D_j|fc><fc|D_k|ga>}{\hbar(\omega_{fg} + \omega_{ca} + \omega)} + \frac{<gb|D_k|fc><fc|D_j|ga>}{\hbar(\omega_{fg} + \omega_{cb} + \omega)} \qquad [2\text{-}17]$$

If the incident frequency ω_0 is far from any electronic absorption band such that $\omega_{fg} - \omega$ is large compared to the shift of the electronic levels resulting from nuclear motion then we may neglect ω_{ca} and ω_{cb} in the denominator of equation 2-17.

The result of the Placzek approximations may be written,

$$\alpha_{jk}^{ba} = <b|\alpha_{jk}(\boldsymbol{X})|a> \qquad [2\text{-}18a]$$

$$\alpha_{jk}(\boldsymbol{X}) = \sum_f \frac{<g|D_j|f><f|D_k|g>}{\hbar(\omega_{fg} + \omega)} + \frac{<g|D_k|f><f|D_j|g>}{\hbar(\omega_{fg} + \omega)} \qquad [2\text{-}18b]$$

where $\alpha_{jk}(x)$ is considered to be an operator that connects nuclear states $|a>$ and $|b>$. When $\omega << \omega_{fg}$, which is the case for nonresonant scattering, the denominator may be treated as a constant. The great utility of Placzek theory is that it removes the necessity of calculating excited electronic states of molecules.

These approximations permit attention to be directed on the motion of nuclei, and thus precede the harmonic approximation typically described in introductory texts.

Spectral Density and Polarizability Fluctuations

Before proceeding with the mathematical treatment of nuclear motion, it is useful to clarify its connection with measurements made experimentally. The time-correlation function approach that follows also illustrates that, while Rayleigh scattering is an elastic process and Raman scattering an inelastic one, they share a common physical origin in their dependence upon polarizability fluctuations that arise from the motion of nuclei[41].

Experimental Geometry and General Equations.

With reference to Figure 2-1, consider a sample located at the origin. Provided the scattering medium is nonmagnetic and nonconducting, the description of its response to an incident electric field may be given in terms of a local polarizability,

$$\alpha(\boldsymbol{r},t) = \bar{\alpha}\boldsymbol{I} + \delta\alpha(\boldsymbol{r},t) \qquad [2\text{-}19]$$

in which I is the second rank unit tensor, and $\delta\alpha(\mathbf{r},t)$ is the polarizability fluctuation tensor at position **r** and time t. By convention, the polarization of the laser is taken to be along the z-axis. Let the incident electric field be a plane wave of the form

$$\boldsymbol{E_i}(\boldsymbol{r},t) = \boldsymbol{n_i}E_0 \exp\,[i(\boldsymbol{k_i}\cdot\boldsymbol{r_i} - \omega_i t)] \qquad [2\text{-}20]$$

in which $\mathbf{n}_i$ is a unit vector in the direction of the electric field, E_0 is the field amplitude, $\mathbf{k}_i$ is its wave vector and ω_i its angular frequency.

For an experimental arrangment that includes a polarizer admitting scattered light with polarization $\mathbf{n}_f$, and a monochrometer selecting light of angular frequency ω_f, the spectral density of light scattered into the detector will be proportional to,

$$I_{if}(\boldsymbol{q},\omega) = \frac{1}{2\pi}\int_{-\infty}^{+\infty} dt\, \langle\delta\alpha_{if}(\boldsymbol{q},0)\,\delta\alpha_{if}(\boldsymbol{q},t)\rangle \exp[i\omega t] \qquad [2\text{-}21]$$

$$\omega \equiv \omega_{laser} - \omega_{scat}$$

where the brackets indicate the ensemble average, and the subscripts i and f indicate the relevant initial and final coordinate axes in the laboratory frame. The proportionality constant is the product of two factors, the first of which depends on the distance from the sample to the detector, R, the incident light intensity, $I_0 = |E_0|^2$, and the scattering wave vector, $\mathbf{k}_f$, and is given by,

$$\frac{k_f^4 I_0}{16\pi^2 R^2 \epsilon_0^2} \qquad [2\text{-}22]$$

The second factor is not so easily obtained since it depends on experimental details such as the efficiency of the polarizer and detector.

It is convenient, for reasons which will be made apparent shortly, to define two quantities describing the intensity of scattered light at the detector:

$$\begin{aligned} I_{iso}(\omega) &= I_{VV}(\omega) - \frac{4}{3} I_{VH}(\omega) \\ I_{aniso}(\omega) &= I_{VH}(\omega) \end{aligned} \qquad [2\text{-}23]$$

which are known as the isotropic and anisotropic (or depolarized) spectra. The first subscript indicates the polarization of the incident light, traditionally labeled "vertical", and the second subscript indicates the polarization of scattered light at the detector, which may be arranged by the experimentalist to be either vertical or horizontal.

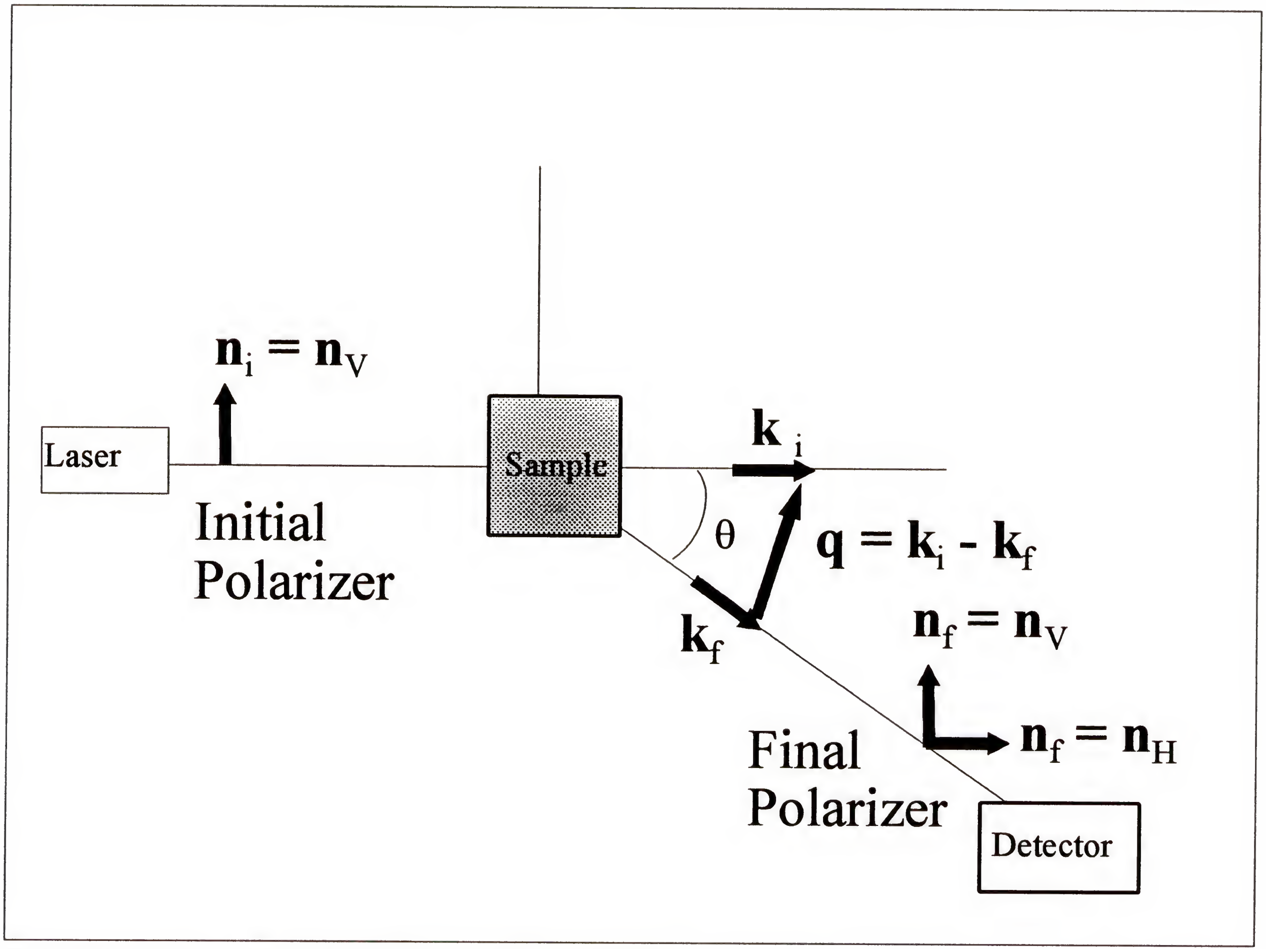
$\mathbf{n}_i = \mathbf{n}_V$
Laser
Initial Polarizer
Sample
$\mathbf{k}_i$
θ
$\mathbf{q} = \mathbf{k}_i - \mathbf{k}_f$
$\mathbf{k}_f$
$\mathbf{n}_f = \mathbf{n}_V$
$\mathbf{n}_f = \mathbf{n}_H$
Final Polarizer
Detector

Figure 2-1. Experimental geometry.

This provides the general approach that is appropriate for the study of Raman scattering from a wide variety of molecules, and the more difficult case of molecular liquids.

Special Cases of Interest

The description of light scattering from molecular liquids quickly becomes complicated by molecular anisotropy and intermolecular interactions. Thus it is useful to have in mind the simpler results of certain special cases.

In the simplest case, the medium consists of independent, isotropic, and structureless scattering centers[42]. The polarizability tensor reduces to a scalar, $\alpha = \alpha\,\delta_{ij}$, and the polarizability fluctuations assume a particularly simple form:

$$\delta\alpha_{if}(\boldsymbol{q},t) = (\boldsymbol{n_i}\cdot\boldsymbol{n_f})\,\alpha\sum_j \exp[i(\boldsymbol{q}\cdot\boldsymbol{r}^{(j)}(t))] \qquad [2\text{-}24]$$

where the sum is performed over the scatterers within the relevant volume. As a result, the (Rayleigh) scattering is determined only by translational motion which, for a system of identical scatterers, can be expressed in terms of density fluctuations in the scattering volume (as indicated by the subscript "SV"),

$$I_{VH}(\mathbf{q},\omega) = I_{HV}(\mathbf{q},\omega) = 0 \qquad [2\text{-}25a]$$

$$I_{HH}(\mathbf{q},\omega) = \alpha^2\int_{-\infty}^{+\infty} dt\, e^{-i\omega t} <\delta\rho^*_{SV}(\mathbf{q},0)\,\delta\rho_{SV}(\mathbf{q},t)> \qquad [2\text{-}25b]$$

$$\delta\rho_{SV}(\mathbf{q},t) = \int_{SV} d^3r\, \delta\rho(\mathbf{r},t)\, \exp[i\mathbf{q}\cdot\mathbf{r}] \qquad [2\text{-}25c]$$

It can be seen that the anisotropic scattering vanishes identically, as expected. To proceed, one typically uses kinetic molecular theory or a hydrodynamic model to calculate these density fluctuations[42].

The significance of the depolarized scattering becomes apparent if we relax the requirement of molecular isotropy, though we will retain the assumption that these molecules do not interact with one another. For such a system of N identical molecules, and assuming the statistical independence of translation and rotation, the time correlation function of interest is[43]

$$I_{if}(\mathbf{q},t) = <N><\alpha_{if}(0)^*\, \alpha_{if}(t)>F_s(\mathbf{q},t) \qquad [2\text{-}26a]$$

$$F_s(\mathbf{q},t) = <\exp[i\mathbf{q}\cdot(\mathbf{r}_j(t) - \mathbf{r}_j(0))]> \qquad [2\text{-}26b]$$

The $\alpha_{if}(t)$ are elements of the molecular polarizability tensor in the laboratory fixed coordinate system and change with time because of molecular reorientation. The **q** dependence can be seen to lie entirely in density fluctuations, formally separated as $F_s(\mathbf{q},t)$.

The tensorial nature of the polarizability can no longer be avoided, but it can be simplified by first choosing a molecule-fixed coordinate system such that the polarizability assumes diagonal form and which contains, as its components, the three principal values of the polarizability, α_1, α_2, α_3. One may then write the tensor as the sum of an isotropic part α_0 and anisotropic part β:

$$\alpha = \alpha_0 \mathbf{I} + \beta \qquad [2\text{-}27a]$$

$$\alpha_0 = \frac{1}{3} Tr[\alpha] \qquad Tr[\beta] = 0 \qquad [2\text{-}27b,\ 2\text{-}27c]$$

In the simplest non-trivial case, that of a cylindrically symmetric molecule, one may label the axis of highest symmetry by $\parallel$, and the remaining two by $\perp$. This gives,

$$\alpha_0 = \frac{1}{3}(\alpha_\parallel + 2\alpha_\perp) \qquad \beta = (\alpha_\parallel - \alpha_\perp) \qquad [2\text{-}28a,\ 2\text{-}28b]$$

The position of the detector with respect to the sample is ordinarily fixed such that the scattering vector **q** is fixed at 90°. The dependence on **q** may be then left implicit and the spectral densities assume particularly simple forms:

$$I_{iso}(\omega) = I_{VV}(\omega) - \frac{4}{3}I_{VH}(\omega) = \langle N\rangle\alpha^2(\omega) \qquad [2\text{-}29a]$$

$$I_{VH}(\omega) = \langle N\rangle\frac{1}{15}\beta^2(\omega) \qquad [2\text{-}29b]$$

Although this discussion has assumed cylindrical symmetry, equations 2-29a and 2-29b are general in the sense that only the depolarized spectrum will contain information about the optical anisotropy, however its precise form will depend on the arrangement of atoms within the particular molecule.

In the final special case, the effects of intermolecular interaction will be considered. At moderate densities, even the ideal gases argon and krypton have been found to depolarize scattered light. The anisotropy responsible for this depolarization is a result of the electron cloud deformation that occurs when two atoms approach one another. If the collisional pair is regarded as a quasilinear molecule for the duration of the collision, we may write the polarizability tensor in the form

$$\alpha(r_{ij}) = \alpha(r_{ij})\boldsymbol{I} + \beta(r_{ij})[\boldsymbol{e}_{ij}\boldsymbol{e}_{ij} - \frac{1}{3}\boldsymbol{I}] \qquad [2\text{-}30]$$

where $\mathbf{e}_{ij}$ is a unit vector in the direction of $\mathbf{r}_{ij} = \mathbf{r}_i - \mathbf{r}_j$. In the limit of infinite separation, and for identical atoms, these terms reduce to:

$$\lim_{r_{ij}\to\infty}\alpha(r_{ij}) = \alpha_0 + \alpha_0 = 2\alpha_0 \qquad [2\text{-}31a]$$

$$\lim_{r_{ij}\to\infty}\beta(r_{ij}) = 0 \qquad [2\text{-}31b]$$

Both terms will reflect the effects of the collision. The depolarized spectrum will be proportional to the Fourier transform of the time correlation function

$$C_{VH}(t) = \langle\sum_{i\neq j}\sum_{l\neq m}\beta(r_{lm}(0))\beta(r_{ij}(t))\ P_2(e_{lm}(0)\cdot e_{ij}(t))\rangle \qquad [2\text{-}32]$$

in which the brackets indicate the ensemble average and P_2 is the Legendre polynomial, $P_2(x) = \frac{1}{2}(3x^2 - 1)$. If one can neglect all but two body collisions, then the symmetry of the colliding system simplifies the result to

$$C_{VH}(t) = \langle\beta(r_{lm}(0))\beta(r_{ij}(t))\ P_2(e_{lm}(0)\cdot e_{ij}(t))\rangle \qquad [2\text{-}33]$$

Equations 2-32 and 2-33 both omit a density-dependent multiplicative constant. These results are the simplest examples of what is denoted "Collision Induced Light Scattering", or CILS[44].

The description of light scattering from liquids containing anisotropic molecules will contain features in common with each of the special cases described above as well as specific models for the molecular motion involved. These models are conveniently classified according to the modes of motion treated.

Models of Polarizability Fluctuations

Vibrational Motion: The Harmonic Approximation[45]

If we exclude resonant light scattering, the type of motion which occurs at the fastest time scales and with the largest changes in energy is vibrational motion. Vibrational motion, which must be treated quantum mechanically, is exhaustively treated in the literature; consequently only the most important features will be discussed here.

Let us assume that the electronic problem for a particular molecule has been solved and its equilibrium geometry found. The Hamiltonian describing vibrational motion for a molecule consisting of n atoms oscillating about their equilibrium positions can be written as

$$\hat{H}_{osc}{}' = \sum_i \frac{p_i^2}{2m_i} + \phi \qquad [2\text{-}34]$$

where $p_i^2/2m_i$ represents the kinetic energy of the atom i and ϕ is the atomic potential which is a function of the instantaneous positions of the atoms.

Provided the oscillation amplitudes of the atoms are small, it is a good approximation to expand ϕ in a power series of the coordinates describing the deviation from the equilibrium positions as

$$\phi = \phi^0 + \frac{1}{2}\sum_{i,j} f_{\alpha\beta}(i,j)\,\xi_\alpha(i)\,\xi_\beta(j) + \cdots \qquad [2\text{-}35]$$

where the repeated indices over α and β indicate summation over those indices, ϕ^0 is the potential energy of the atoms at the equilibrium positions, and $f_{ab}(i,j)$ the generalized force constant given by

$$f_{\alpha\beta} = \left[\frac{\partial^2\phi}{\partial x_{i\alpha}\partial x_{j\beta}}\right]_0 \qquad \alpha,\beta = x,y,z \qquad [2\text{-}36]$$

wwhich forms a 3n x 3n matrix. The quantity $\xi_\alpha(i)$ represents the α component of the coordinate that represents the deviation of the i^{th} atom from the equilibrium position and is known as its vibrational coordinate. The linear terms in the vibrational coordinates vanish because the atoms are in their equilibrium positions.

Since the function ϕ^0 does not depend on the vibrational coordinates it is convenient to define a new Hamiltonian given by

$$\hat{H}_{osc} = \hat{H}_{osc}{}' - \phi^0 = \sum_i \frac{p_i^2}{2m_i} + \frac{1}{2}\sum_{i,j} f_{\alpha\beta}(i,j)\,\xi_\alpha(i)\,\xi_\beta(j) + \cdots \qquad [2\text{-}37]$$

This is simplified further by introducing the mass-reduced coordinates $u_a(i)$ and mass-reduced generalized force constants $g_{ab}(i,j)$ which are given by

$$u_\alpha(i) = \xi_\alpha(i)\,m_i^{1/2} \qquad [2\text{-}38a]$$

$$g_{\alpha\beta}(i,j) = (m_i m_j)^{-1/2} f_{\alpha\beta}(i,j) \qquad [2\text{-}38b]$$

Expressed using these mass-reduced variables, H_{osc} is given by,

$$\hat{H}_{osc} = \frac{1}{2}\sum_i P_i^2 + \frac{1}{2}\sum_{i,j} g_{\alpha\beta}(i,j)\,u_\alpha(i)\,u_\beta(j) + V_a \qquad [2\text{-}39a]$$

$$P_\alpha(i) = \dot{u}_\alpha(i) \qquad P_i^2 = \sum_\alpha P_\alpha^2(i) \qquad [2\text{-}39b,\ 2\text{-}39c]$$

where V_a represents the anharmonic term, i.e., the sum of all those higher-order terms not written out explicitly; the harmonic approximation consists in neglecting this term.

One proceeds by finding a linear transformation from $\{u_a(i)\}$ to a new set of coordinates $\{q_j\}$ such that H_{osc} is expressed as a linear combination of only squares of the new coordinates, the cross-product terms having been eliminated. This is called a canonical form and the coordinates q_j are known as the normal coordinates. In these coordinates the Hamiltonian is given by,

$$\hat{H}_{osc} = \sum_k \left(\frac{1}{2}\pi_k^2 + \frac{1}{2}\omega_k^2 q_k^2\right) \qquad \pi_k = \dot{q}_k \qquad [2\text{-}40]$$

This leads to the well known result that the eigenenergy for the eigenstate $|n_k\rangle$ is given by $E_k = (h/2\pi)\omega_k(n + ½)$ from which the vibrational frequency $\nu = \omega/2\pi$ is readily obtained.

For an ensemble of molecules, the spectral density for the scattered light associated with transition of the nuclear state $|a\rangle$ to $|b\rangle$, observed in the j polarization and with the incident light polarized in the k direction is obtained from equation 2-13, which is repeated here, in a slightly altered form, for convenience:

$$I_{jk}(\omega) = \frac{I_0\omega^4}{4c^4} < |\alpha_{jk}|^2 > \delta(\omega - \omega_0 - \omega_{ab}) \qquad [2\text{-}41]$$

Here the a,b superscripts have been suppressed for brevity, and the brackets now indicate the ensemble average.

By introducing the Fourier representation of the delta function equation 2-41 can be manipulated into a form explicitly indicating the relevant time correlation function[40],

$$\hat{I}_{jk}(\omega) = \frac{1}{C}I_{jk}(\omega) = \frac{1}{2\pi}\int_{-\infty}^{\infty} dt \exp[-i\Delta\omega t]<\alpha_{jk}(0)*\alpha_{jk}(t)> \qquad [2\text{-}42]$$

$$\Delta\omega = \omega - \omega_0 \qquad C = I_0(\omega^4/4c^4)$$

It may be observed that this is formally equivalent to the result given in equation 2-21. The isotropic polarizability time-correlation function is given by

$$G_{iso} = <\alpha_0(0)\alpha_0(t)> \qquad \alpha_0 = \frac{1}{3}Tr[\alpha] \qquad [2\text{-}43]$$

For scattering from a fundamental vibration, the isotropic Raman tensor can be expanded in terms of the relevant normal coordinate q giving,

$$\alpha_0 = [\frac{\partial\alpha_0}{\partial q}]_0\, q \qquad G_{iso}(t) = |[\frac{\partial\alpha_0}{\partial q}]_0|^2 <q(0)q(t)> \qquad [2\text{-}44]$$

These are the appropriate formulae for light scattering from a dilute gas, but the situation becomes more complicated in condensed phases. In general, the effects of intermolecular interaction on the Raman scattering spectrum of the normal mode can be described by the interaction Hamiltonian V given by

$$V = V^0 + \frac{1}{2}\sum_{i,j}(V_{ij}^{(1)}q_i + V_{ij}^{(2)}q_iq_j) \qquad [2\text{-}45]$$

where V^0 does not depend on the normal coordinate and q_i is the normal coordinate associated with molecule i. The interaction potential given here is a function of normal coordinates because of molecular vibration that modulates the intermolecular potential. It is of the form applicable to the intermolecular dipole-dipole interaction, quadrupole-quadrupole interaction, hydrogen-bonding interaction, as well as other types of interactions.

Low Frequency Rotational and Translational Motion

Although the quantum mechanical treatment of rotational motion is well known, a discussion of its results is not appropriate here, as a glance at the experimental spectra will confirm: in molecular liquids, the inhomogenous line broadening of the vibrational and rotational spectra by intermolecular interactions makes the fine rotational structure of the intramolecular vibrational peaks indistinct.

The strong intermolecular interactions present in a liquid also complicate the low frequency shift region so that two definitions are in order before proceeding. Rayleigh scattering refers to the elastic and quasi-elastic scattering of light by density fluctuations to give a broadened, but unshifted, line whereas Raman scattering refers to the inelastic energy transfer from the incident light into (or from) a quantized energy state to create a new photon frequency shifted from the incident light. In dilute gases these regions are separated by at least 1000 cm^{-1} and they are studied using distinct theoretical and experimental methods.

Under the relatively high-resolution, low-gain experimental conditions of Rayleigh scattering, the Rayleigh wing exhibits distinct non-Lorentzian behavior which under the low-resolution, high-gain conditions of the Raman experiment appears as a weak local maximum on the wing of the intense Rayleigh line. These "peaks" have been observed in essentially all isotropic or anisotropic liquids studied to date. Though there are important differences in the details of their interpretation, their is strong evidence to suggest that for anisotropic liquids the additional depolarized scattering has a predominantly librational origin, while the isotropic spectrum contains effects from both librational and translational motion. The latter is often interpreted in terms of intermolecular vibrational motion while the former may be thought of as a quantized molecular libration much like those that give rise to rotatory Raman lattice modes in the solid phase, or as an incomplete loss of memory after collision in the rotational-diffusional behavior molecules. For spherically symmetric molecules such as CCl_4 and SF_6, Bucaro and Litovitz and Posch and Litovitz have been able to account for the depolarized spectra by considering the polarizability anisotropy caused by both collision-induced frame distortion and dipole-induced dipole mechanisms. Similar approaches have been successful in the description of the scattering from anisotropic molecules, specifically water.

Consequently, this discussion will cover a treatment which is appropriate for molecular liquids and whose formalism can be readily extended to light scattering from both the lower frequency rotational motion of molecules in their ground vibrational state and to their translational motion. The treatment relies heavily on the insight provided by the study of low frequency collision induced light scattering from rare gasses which occurs at moderate densities and is commonly denoted the Dipole-Induced-Dipole (DID) model[46].

The formalism begins by adopting a physically broader perspective which will, unfortunately, require some changes in notation. Consider an element of volume containing a number of scattering centers. From the preceeding discussion we can immediately write the spectral density of the scattered light in terms of the polarizability of the scattering centers,

$$I(\tilde{\nu},\mathbf{n},\mathbf{m}) = \sum_{\alpha,\beta} (n_\alpha)^2 (m_\beta)^2 I_{\alpha,\beta}(\tilde{\nu}) \qquad [2\text{-}46a]$$

$$I_{\alpha\beta}(\tilde{\nu}) = FT\left[\sum_{i,j} \langle P^i_{\alpha\beta}(t)\, P^j_{\alpha\beta}(0)\rangle\right] \qquad [2\text{-}46b]$$

where **n** and **m** are unit vectors in the direction of the incident and observed polarization respectively. Greek subscripts refer to Cartesian components in the laboratory frame and FT refers to the Fourier transform, which is defined by

$$FT[f(t)] = \frac{1}{2\pi}\int_{-\infty}^{\infty} dt \exp[-2\pi i\tilde{\nu}t]\, f(t) \qquad [2\text{-}46c]$$

P^i is the effective polarizability of the i^{th} molecule and is defined by,

$$P^i{}_{\alpha\beta}(t) = \lim_{E^o \to 0} \frac{\partial \mu^i_\alpha(t)}{\partial E^o_\beta} \qquad [2\text{-}47]$$

where μ_i is the total dipole moment on the molecule, and $\mathbf{E}^0$ denotes the incident laser field. An expression for the total dipole moment can be obtained from long-range perturbation theory[47]:

$$\begin{aligned} \mu^i_\alpha = {}^0\mu^i_\alpha + \sum\nolimits_\beta \alpha^i_{\alpha\beta}(E_\beta)^i \\ + \frac{1}{3}\sum\nolimits_{\beta\gamma} A^i_{\alpha\beta\gamma}(E'_{\beta\gamma})^i + \sum\nolimits_{\beta\gamma} \beta^i_{\alpha\beta\gamma}(E_\beta)^i(E_\gamma)^i + \ldots \end{aligned} \qquad [2\text{-}48]$$

in which ${}^0\mu_i$ refers to the permanent dipole moment on the ith molecule. The remaining terms are refered to as the "collision induced" contributions to the total dipole moment. They contain contributions from the permanent molecular polarizability, $\boldsymbol{\alpha}^i$, the first hyperpolarizability, $\boldsymbol{\beta}$, and the dipole-quadrupole polarizability, $\mathbf{A}^i$ due to the influence of $(\mathbf{E})^i$, the local electric field and its gradient, $(\mathbf{E}')^i$. The local field is the effective field experienced by the i^{th} molecule. It is given by the superposition of the external field with those generated by the multipoles of nearby molecules:

$$(E_\alpha)^i = {}^0E_\alpha + \sum_j \sum_\beta T^{(2)}_{\alpha\beta}(ij)\mu^j_\beta + \sum_j \sum_{\beta\gamma} T^{(3)}_{\alpha\beta}(ij)\Theta^j_{\beta\gamma} + \ldots \qquad [2\text{-}49]$$

$\mathbf{T}^{(n)}$ is the n-pole propagator defined by,

$$T^{(n)}_{\alpha_1\alpha_2\ldots\alpha_n}(ij) = (-1)^n[\nabla_{\alpha_1}\nabla_{\alpha_2}\ldots\nabla_{\alpha_n}\frac{1}{|r|}]_{r=R_{ij}} \qquad [2\text{-}50]$$

Θ_ι is the effective quadrupole moment on the ith molecule, defined by,

$$\Theta^i_{\alpha\beta} = {}^0\Theta^i_{\alpha\beta} + \sum_\gamma A^i_{\gamma\alpha\beta}(E_\gamma)^i + \ldots \qquad [2\text{-}51]$$

The final expression for the effective polarizability, is given in Cartesian components to first order in the n-pole propagator and written assuming the Cartesian summation convention, i.e., summation is implied over repeated subscripts:

$$\begin{aligned} P^i_{\alpha\beta} = \alpha^i_{\alpha\beta} + \Pi^i_{\alpha\beta} = \alpha^i_{\alpha\beta} + \sum_{i\neq j} [\alpha^i_{\alpha\gamma}T^{(2)}_{\gamma\delta}(ij)\alpha^j_{\alpha\beta} + \beta^i_{\alpha\beta\gamma}T^{(2)}_{\gamma\delta}(ij)\mu^j_\delta \\ + \frac{1}{3}\alpha^i_{\alpha\epsilon}T^{(3)}_{\epsilon\gamma\delta}(ij)A^j_{\beta\gamma\delta} + \frac{1}{3}A^j_{\alpha\gamma\delta}T^{(3)}_{\epsilon\gamma\delta}(ij)\alpha^j_{\epsilon\beta} + \ldots] \end{aligned} \qquad [2\text{-}52]$$

It has been written to indicate the separate contributions of the permanent molecular polarizability, $\boldsymbol{\alpha}^i$ and an induced part, $\boldsymbol{\Pi}^i$. The resulting expressions for the isotropic and depolarized spectral densities are,

$$I_{iso}(\tilde{\nu}) = < |FT (\sum_i \frac{1}{3}\sum_\alpha P^i_{\alpha\alpha}(t))|^2 > \qquad [2-53]$$

$$I_{aniso}(\tilde{\nu}) = <|FT[\sum_i \frac{1}{10}\sum_{\alpha\beta} [P^i_{\alpha\beta}(t) - \delta_{\alpha\beta}(\frac{1}{3} \sum_\gamma P^i_{\gamma\gamma}(t))]] |^2 > \qquad [2-54]$$

Chapter 4 contains a more detailed description of how these terms may be calculated from configurations generated by a molecular dynamics simulation. The procedure requires using the well-known relationship between properties given in the laboratory coordinate system, labeled by Greek subscripts, and coordinates fixed in the molecular frame, labeled by Latin subscripts. Thus, one may calculate the contribution due to the permanent molecular polarizability using

$$\alpha_{\alpha\beta} = \sum_i \sum_j C_{\alpha i}\, \alpha_{ij}\, C_{\beta j} \qquad [2-55]$$

where **C** is the linear transform specifying the orientation of the two coordinate systems with respect to each other.

Some general comments on the interpretation of these spectral densities are in order here before postponing a discussion of the remaining details until Chapter 4. The time correlation function of the total polarizability tensor can be separated into a sum of terms containing only self-correlations of the permanent molecular polarizabilities and a sum over terms containg cross-correlations. The so-called "allowed spectrum" is the Fourier transform of the sum over self-correlations. It is related to single particle translational motion through the trace of the permanent molecular polarizability, α_0, and to orientational motion through the anisotropy, δ, of the permanent molecular polarizability.

The remaining terms constitute the Collision induced spectrum. The "$\beta T\mu$" and the "αTA" are the most important of these terms. The former includes terms involving "$\alpha T\alpha$", which is due to isotropic part of polarizability alone and is relatively large, and two lesser contributions, "$\alpha T\delta$" and "$\delta T\delta$", which are much smaller and are due, in part, to the optical anisotropy.

Reduction Procedures and Relationships to Other Methods

The dynamical region probed by spontaneous light scattering overlaps those probed by other techniques, particularly infrared (IR) spectroscopy, and inelastic neutron scattering (INS). This is one of the motives for recasting the expressions for the scattered intensity into a form suitable for comparison with these other techniques. The second motive is the desire to distinguish the low frequency inelastic processes from the much more intense contribution of elastic or Rayleigh scattering[48].

The Raman spectral density, $I(\omega)$, is given by the Fourier transform of the total polarizability time correlation function and can be expressed as the sum of the intensities on the Stokes side, $I^{st}(\omega)$, and the anti-Stokes side, $I^{as}(\omega)$:

$$I(\omega) = I^{st}(\omega) + I^{as}(\omega) \qquad [2\text{-}56]$$

where ω is the shift in angular frequency. A function $R(\omega)$ can be defined according to,

$$R(\omega) = \omega[I^{st}(\omega) + I^{as}(\omega)] \qquad [2\text{-}57]$$

According to the principle of detailed balance,

$$I^{as}(\omega)/I^{st} = \exp[-h\omega/2\pi kT] \qquad [2\text{-}58]$$

which, on substitution into equation 2-57, gives us:

$$R(\omega) = \omega\{1-\exp[-h\omega/2\pi kT]\}\ I^{st}(\omega) \qquad [2\text{-}59]$$

Taking into account the dependence of the scattered intensity on the fourth power of the real frequency the final expression for what is commonly termed the "reduced" representation of the spectrum is,

$$R(\omega) = (\omega_0 - \omega)^{-4}\,\omega\{1 - \exp[-h\omega/2\pi kT]\}\; I^{st}(\omega) \qquad [2\text{-}60]$$

where ω_0 is the frequency of the laser. Typically, the angular frequency shift is converted to the wavenumber shift. The R(ω) function has been interpreted as the energy absorbed in the scattering process.

In one common variation, the reduced representation is reported in the mathematically equivalent form:

$$R(\omega) = I^{st}(\omega)\;(\omega_0 - \omega)^{-4}\omega\,\tanh(h\omega/4\pi kT) \qquad [2\text{-}61]$$

In the low-frequency region the relative intensity dependence upon the fourth-power term is not important. For example, using an Argon-ion laser at 514.5 nm as the exciting source, as is the case for the experimental results reported in this work, the influence of this factor in the region 10 to 200 cm^{-1} is around 4%. Neglecting the fourth-power term and expanding the exponential, keeping on the first term linear in ω, gives an approximate expression for R(ω) that is in common use:

$$R^{approx}(\omega) \propto \omega^2\, I^{st}(\omega) \qquad [2\text{-}62]$$

Ordinarily, one measures only the Stokes intensity and the superscript is suppressed.

The R(ω) representation is convenient because it permits direct comparison with the infrared absorption coefficient, $\alpha_{ir}(\omega)$, which has a similar relationship to the dipole correlation function, <μ(0)μ(t)>:

$$\alpha_{ir}(\omega) \propto I_{ir}(\omega)\ \omega \tanh(h\omega/4\pi kT) \qquad [2\text{-}63a]$$

$$I_{ir}(\omega) = \int_{-\infty}^{\infty} dt\ e^{-i\omega t} <\mu(0)\mu(t)> \qquad [2\text{-}63b]$$

The reduced representation is also useful for coping with the enormous intensity of the central Rayleigh line that is a serious problem in studies of low-frequency Raman spectra. The time scale for motions giving rise to the Rayleigh line is relatively slow compared to events reflected in the low-frequency Raman region. The correlation function can be expressed as an exponential decay giving rise to a Lorentzian shape for the Rayleigh line. A Lorentzian band centered at a Raman shift of zero cm^{-1} is converted into a rather smooth baseline in the R(ν) representation, thus making the weaker Raman features much more apparent.

CHAPTER 3
EXPERIMENTAL DESIGN AND RESULTS

Raman Cell

A cell appropriate for light scattering at elevated pressures was specially designed and constructed. The cell consisted of a series of concentric cylindrical sleeves that were held in place by chamber heads at each end. Window flanges at the two ends completed the basic assembly. The innermost sleeve was constructed of quartz and had an inner diameter of 0.240 inches, an outer diameter of 0.475 inches, and a length of 2.495 inches; the sample was contained by this sleeve. A brass sleeve (0.484 inches i.d., 0.625 inches o.d.) surrounded the first sleeve and had an overall length of 2.031 inches. A shoulder extended radially from 0.610 inches from center and was 0.065 inches deep from either end. Three slots were cut in this sleeve, each 1/8 inch wide and 1.125 inches long centered longitudinally with their centers 90 degrees apart.

The brass sleeve was followed by a second quartz tube (0.870 inches i.d., 0.988 inches o.d., 2.093 inches in length). Coolant fluid (50% ethylene glycol + 50% water by mass) flowed through the gap between the brass and outer quartz sleeve. A final sleeve was constructed of delrin (1.103 inches i.d., 1.312 inches o.d.) and protected the bundle from outside shock. It had an overall length of 1.956 inches and a shoulder extending 0.306 inches from either end. Three slots were cut into the delrin sleeve to line up with those in the brass sleeve. The slots were 3/8 inches wide, and 1.3125 inches long, again centered longitudinally.

The chamber heads were designed to permit high pressures within the sample container while avoiding compression stress that could shatter the quartz components. This was accomplished by machining a series of concentric shoulders on the side facing the sleeves; they permitted the quartz sleeves to float between the two chamber heads without breaking the seals. The chamber heads were constructed of stainless steel and machined to a thickness of 0.75 inches. The central hole was drilled through to a diameter of 0.245 inches. The innermost shoulder extended radially from the central hole to a diameter of 0.484 inches and was 3/8 inches deep. There followed a shoulder extending radially from the first to 0.614 inches from the center of the piece. Finally a groove for the outer quartz and delrin sleeves was cut to a depth of 0.120 inches; this groove had an inner diameter of 0.854 inches and outer diameter of 1.106 inches.

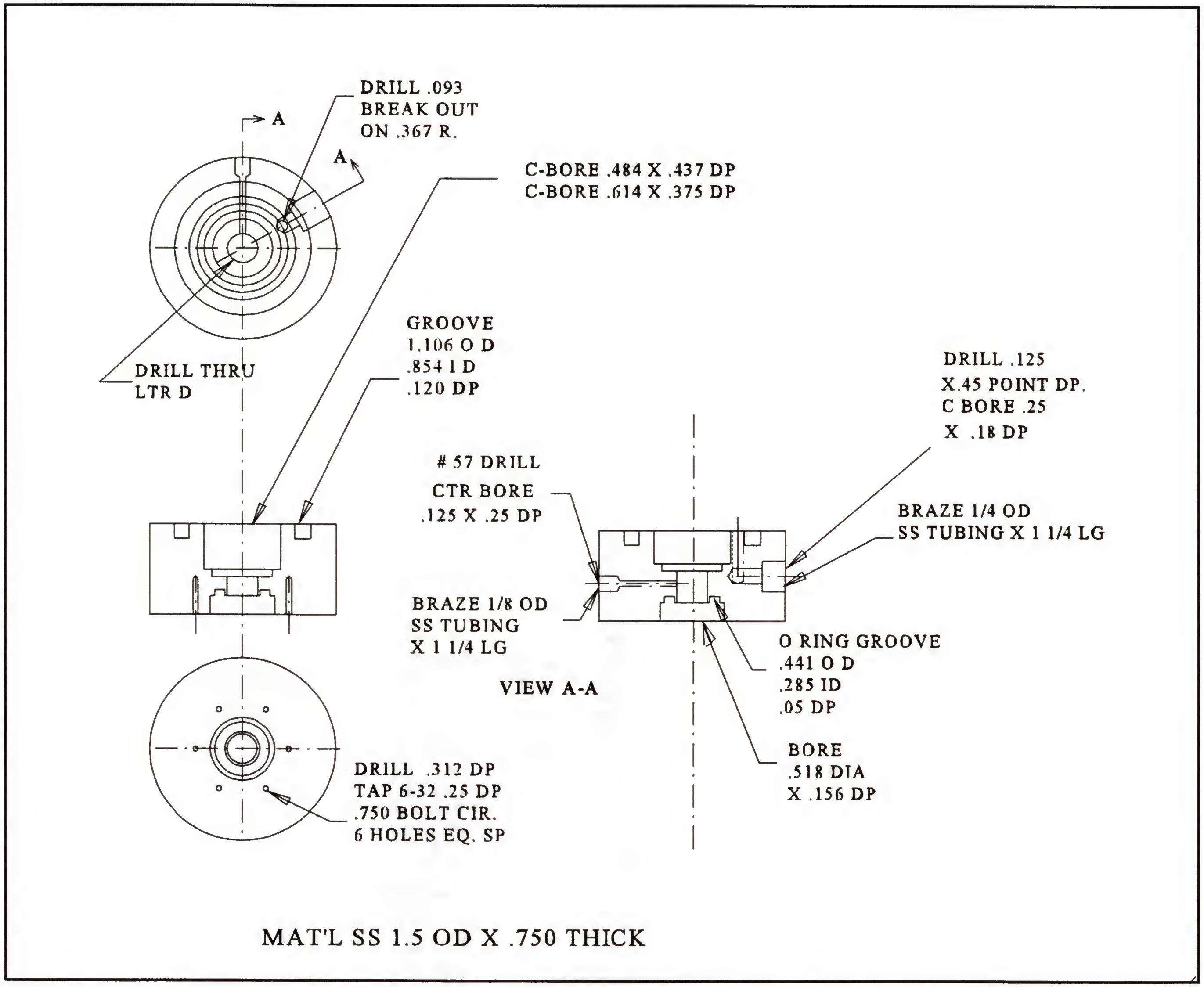

Figure 3-1. Chamber head component of Raman Cell.

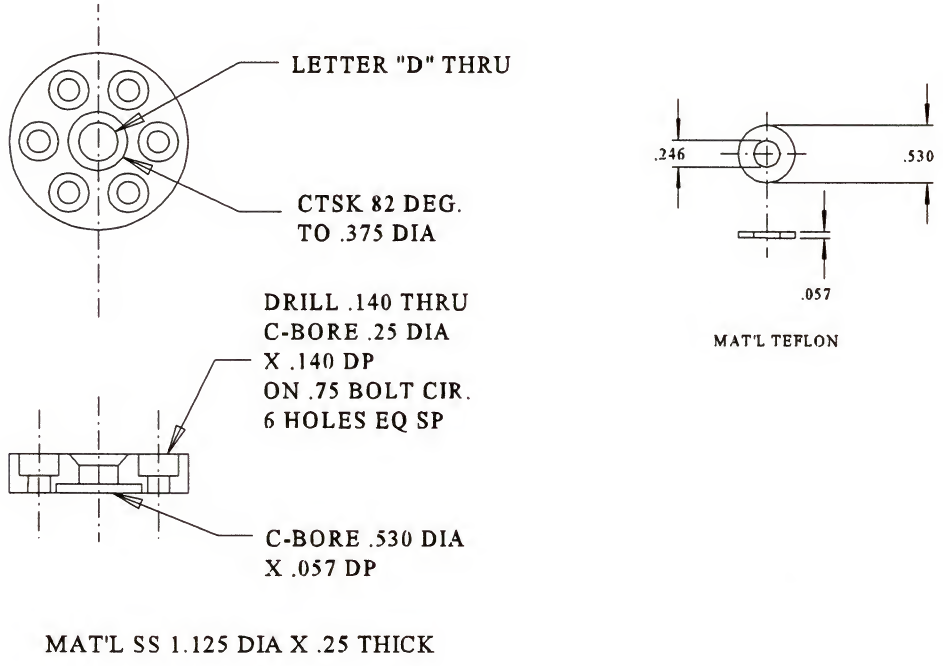

Figure 3-2. Window flange component of Raman scattering cell.

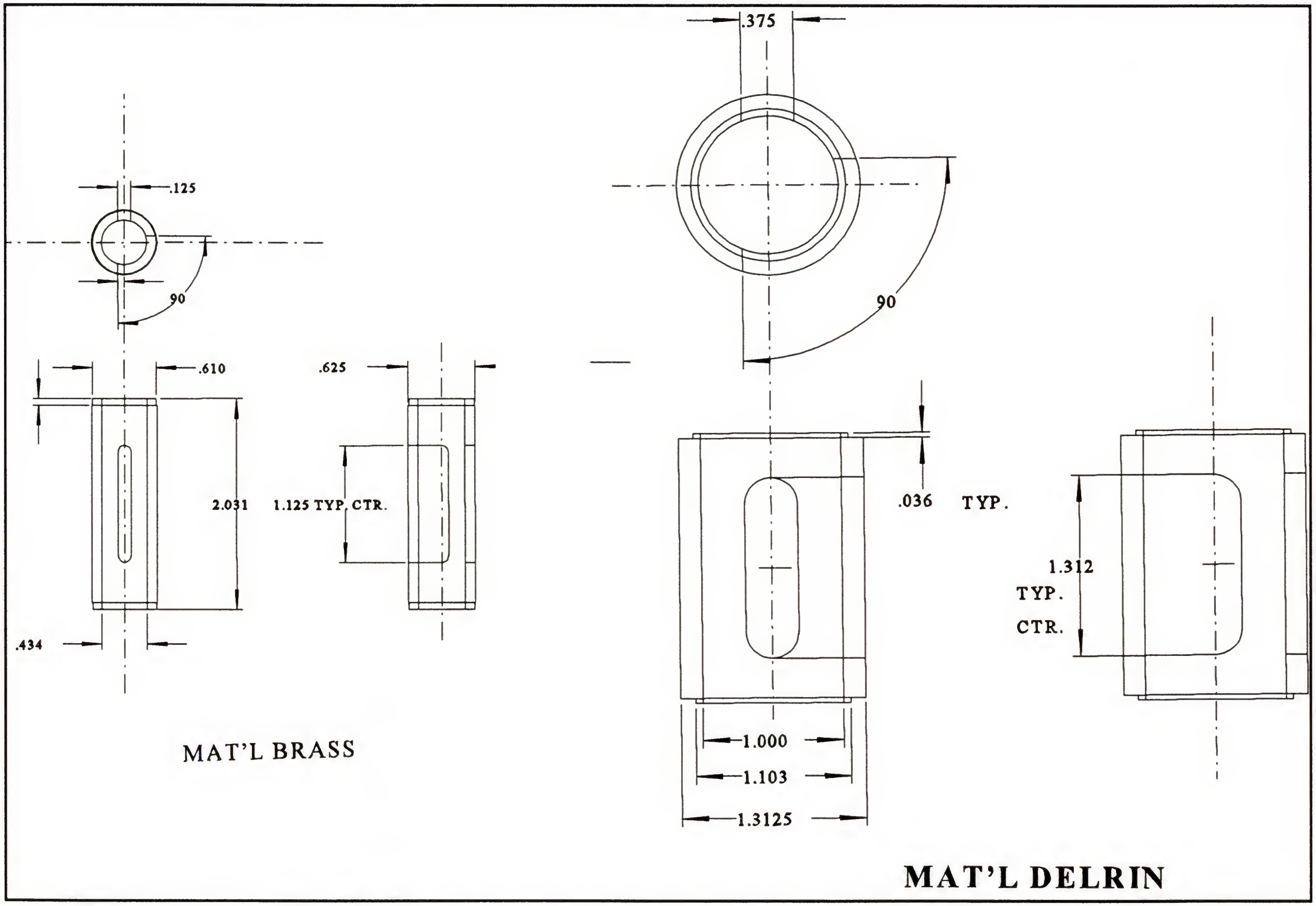

Figure 3-3. Brass and delrin sleeves.

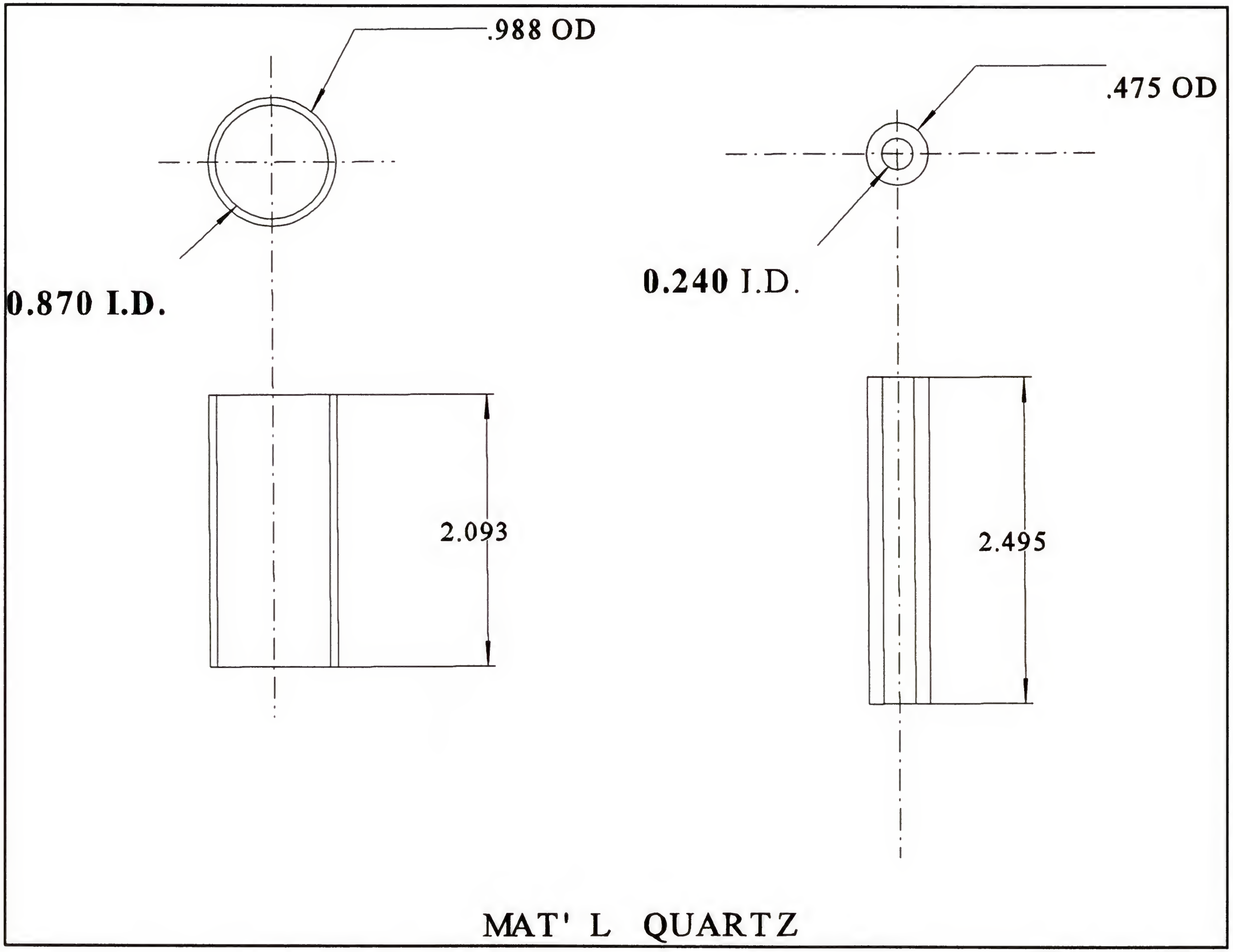

Figure 3-4. Quartz sleeves.

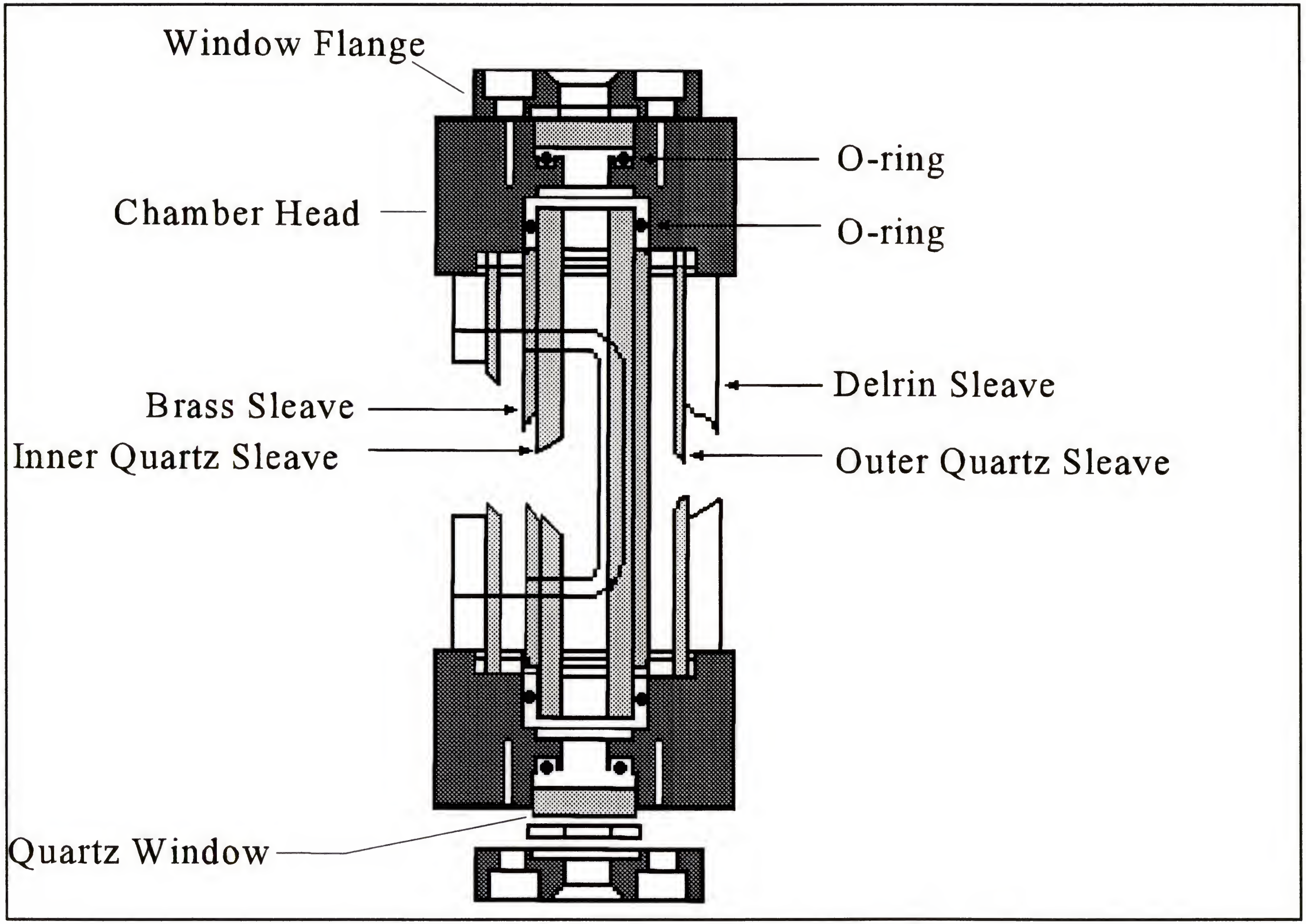

Figure 3-5. Cut-away view of assembly.

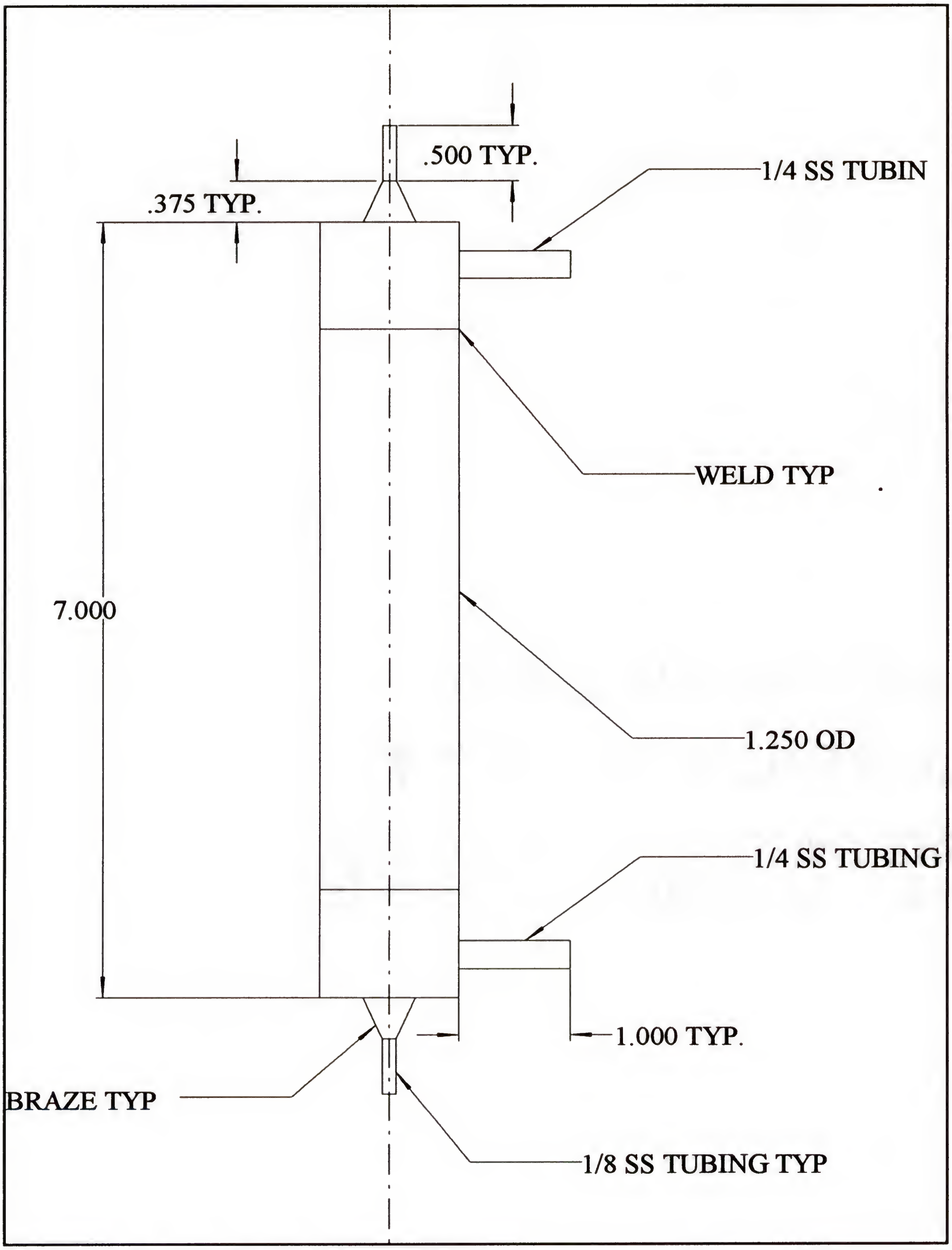

Figure 3-6. Heat exchanger.

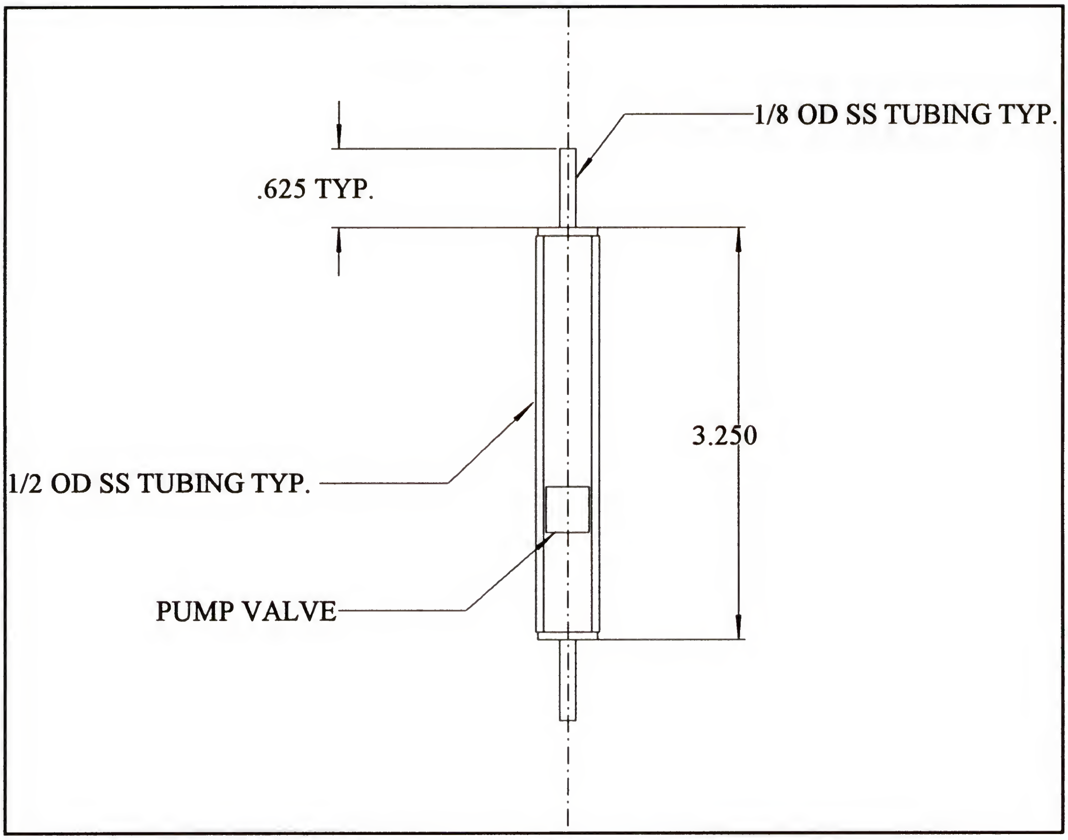

Figure 3-7. Magnetically driven pump.

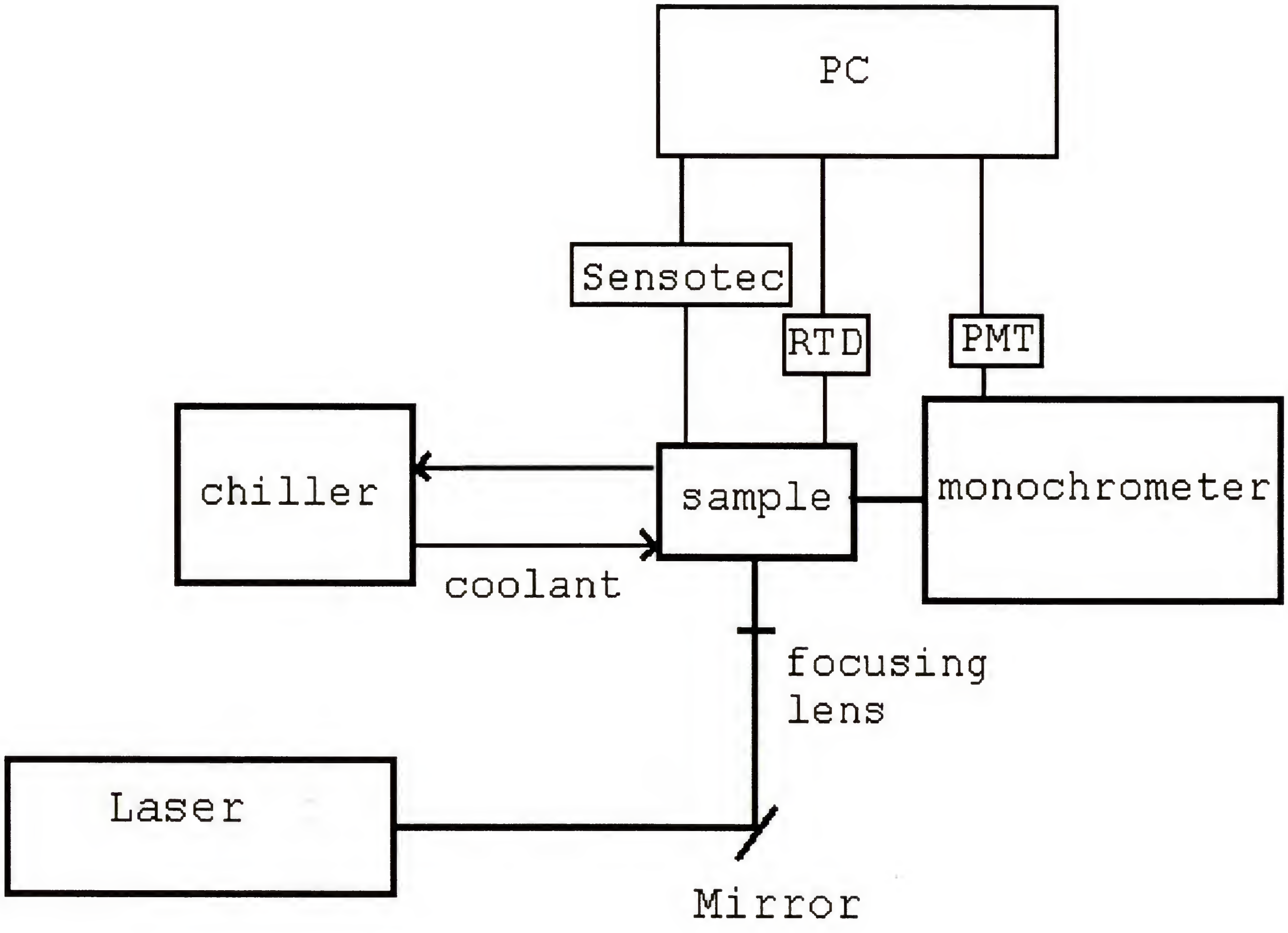

Figure 3-8. Block diagram of experimental setup.

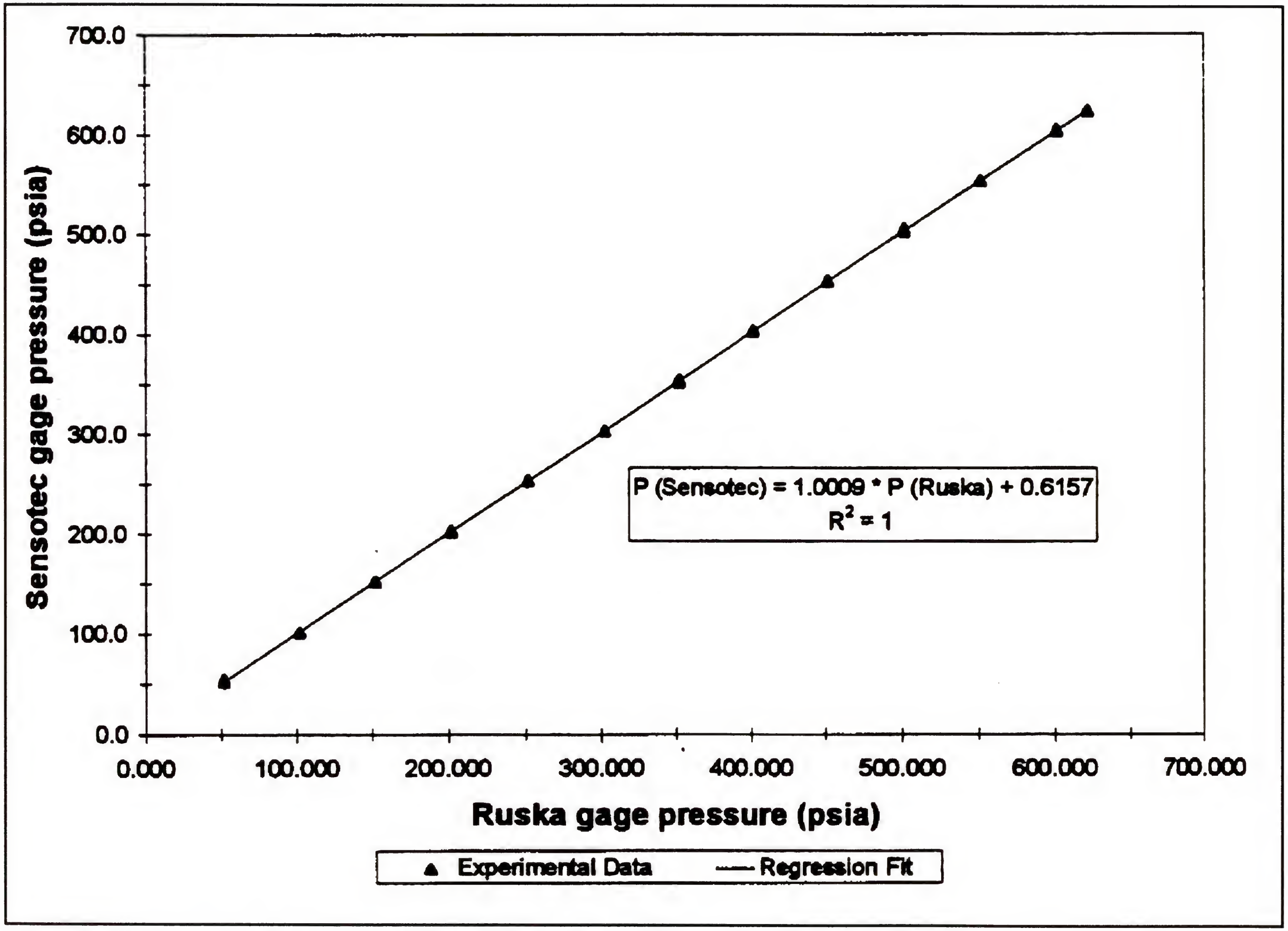

Figure 3-9. Calibration of pressure gage using methane gas.

The opposite (outside) face of the chamber head had a 5/8 inch central hole to house the quartz window. O-rings placed in grooves at the base of the window housing sealed the window against the chamber head.

Each chamber head contains two inlets, one for introduction of the sample and the other for circulation of coolant. The stainless steel tubes (1/8 inch o.d. for the sample inlet and 1/4 inch o.d. for coolant) were brazed into the chamber head. The window flange was held to the chamber head by six 6-32 bolts through holes drilled on a 0.750 inch diameter bolt circle.

The components of the Raman cell are illustrated in Figures 3-1 through 3-4 while their assembly is illustrated in Figure 3-5. In Figure 3-6 the heat exchanger is illustrated which cooled gaseous samples before their introduction into the Raman cell and Figure 3-7 illustrates the one-way pump used to stir the sample.

Instrumentation and Computer Interface

A block diagram of the assembled components is given in Figure 3-8. Source radiation was provided by an Argon ion laser (Spectra Physics Model 2020) tuned to the 514.5 nm line. The power of the incident laser beam was measured using a Scientech, Inc., Model 361 powermeter at 200-400 mW. The excitation power employed was 300 mW and varied by no more than 5%. After the initial polarization was confirmed, only one polarizer was used and it was placed between the sample and the entrance to the monochrometer.

The monochrometer employed was a Spex model 1870 driven by a Spex model 1673c minidrive at the rate of 0.05 nm/sec which permitted acquisition of the 4000 wavenumber spectra in approximately 8 hours. A slit width of 150 μm was used providing a spectral resolution of approximately 4 cm^{-1}. Two standards were used to calibrate the monochrometer: the mercury line from fluorescent room lights (1123.4 cm^{-1}) and the sulfate peak at 980 cm^{-1} of a 0.50 M SO_4^{2-} solution prepared from K_2SO_4.

The signal was detected with a single-channel photon-counting system (RCA 31034A PMT) connected to a Keithley 195A digital voltmeter. The output was then passed to a Gateway 2000 microcomputer containing a 486 CPU operating at 66 megahertz with 32 megabytes of RAM. The interfacing protocol used for the connection of the electronic hardware to the micro-computer was the standardized IEEE general purpose bus interface (GPIB), including the 8-bit i/o card and its accompanying software.

Pressure data were acquired with a Sensotec model TJE/7313-22 strain gage pressure transducer which has an effective pressure range of 0-1,000 psi. This pressure transducer was used together with a Beckman Industrial 600 Series electronic readout device. The Sensotec transducer was calibrated against a Ruska Model 2465 standardized Dead Weight Pressure Gage. The Ruska gage had a pressure range of 0.000 psia to 650.000 psia with an accuracy of ±0.001 psia. The pressure calibration results are shown in Figure 3-9.

A two-wire platinum resistance temperature device (RTD) was used in the experiments. The ceramic, cylindrically-shaped RTD was used in conjunction with a Keithley 195A digital multimeter to read resistance data. The resistance values were converted to their corresponding temperatures, in Celsius, using the following equations and parameters in which $\alpha = 0.00385$, $\delta = 1.502$, $R_0 = 100.00\ \Omega$, and R_t is the resistance of interest,

$$T = \frac{-A + \sqrt{A^2 - 4B\left(1 - \frac{R_t}{R_0}\right)}}{2B}$$

$$A = \alpha\left(1 + \frac{\delta}{100}\right)$$

$$B = -\alpha\delta(0.0001)$$

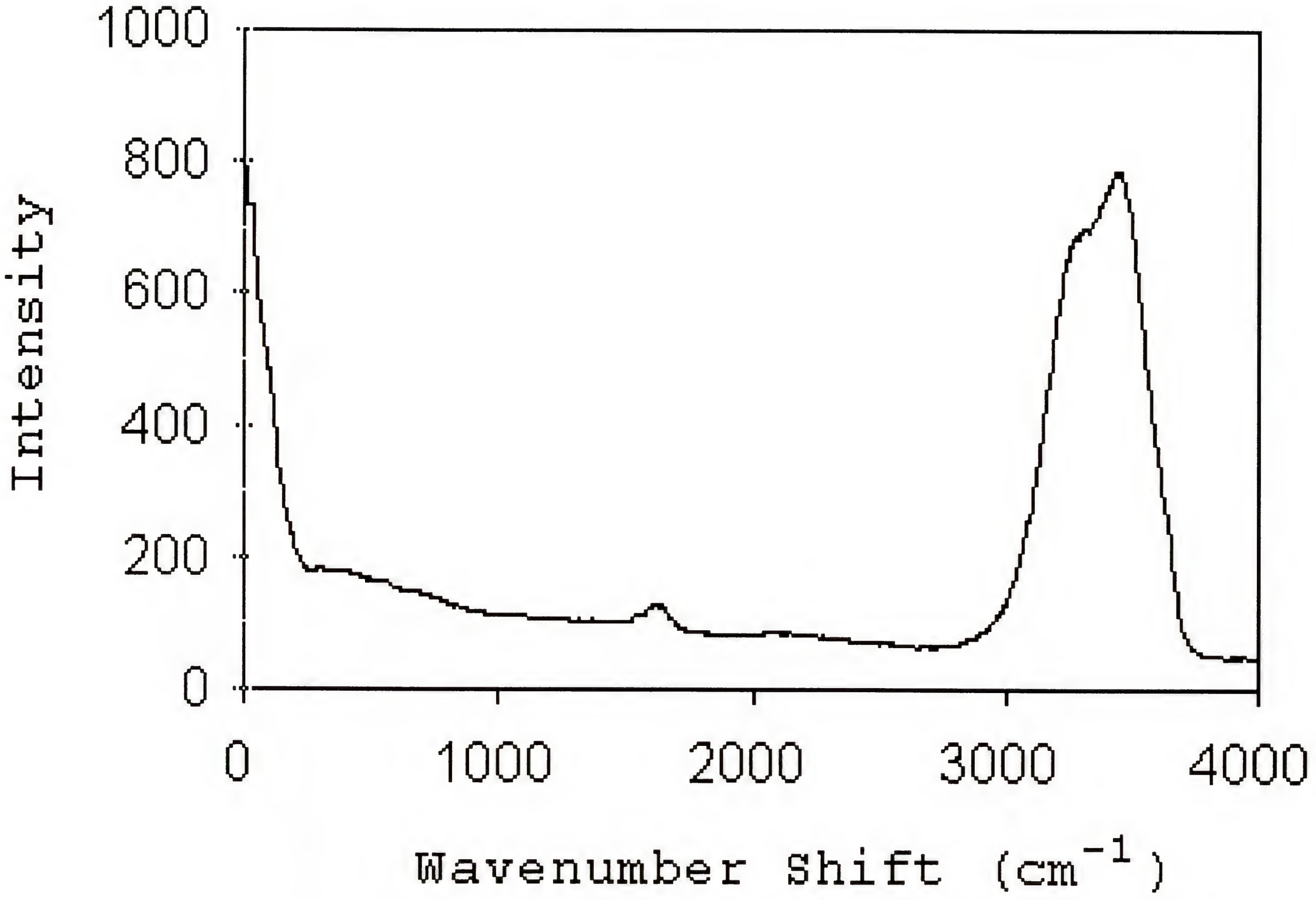

Figure 3-10. Spectrum of scattered light from $H_2O(l)$ at 25 °C.

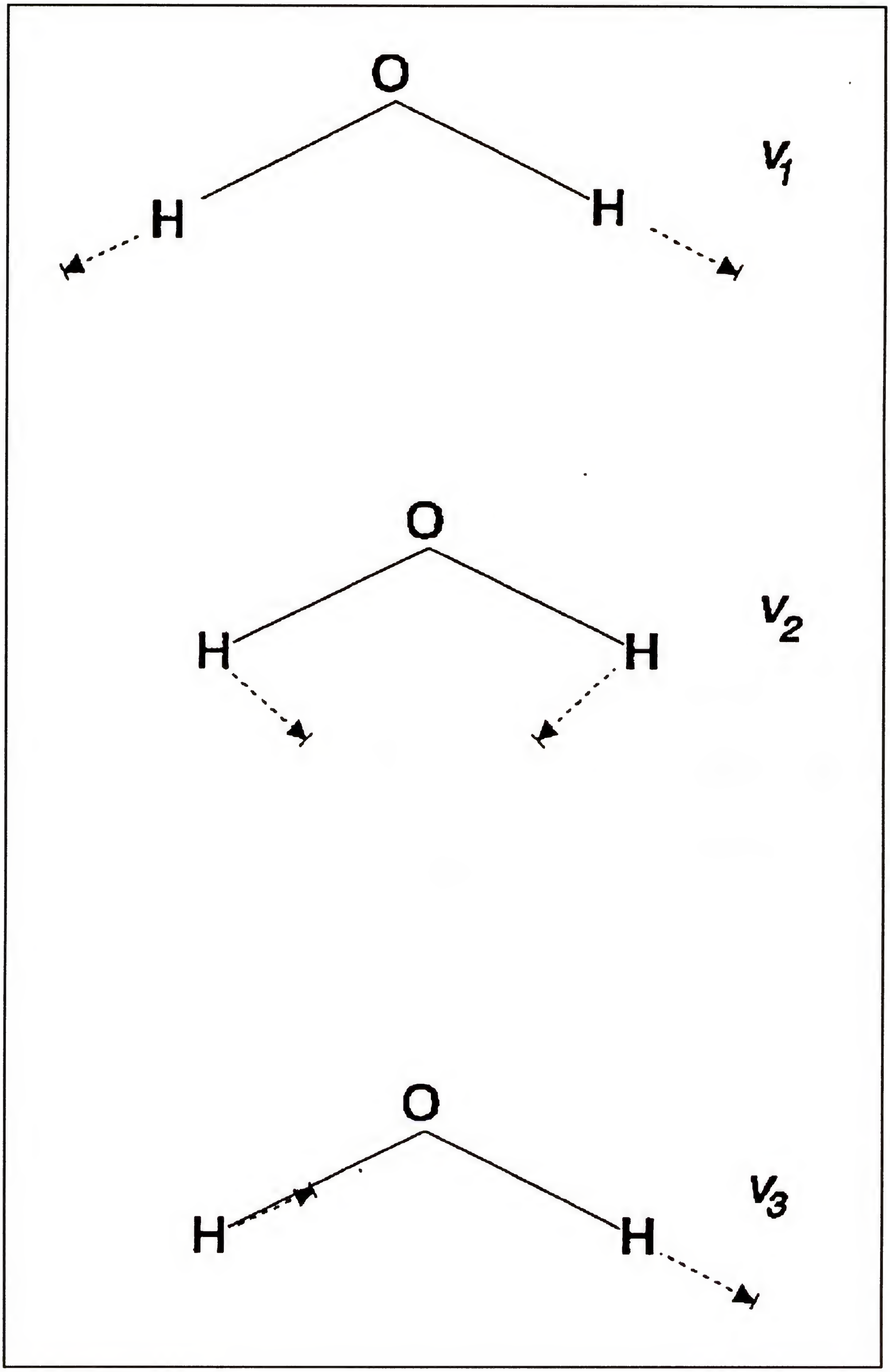

Figure 3-11. The three normal vibrational modes of water.

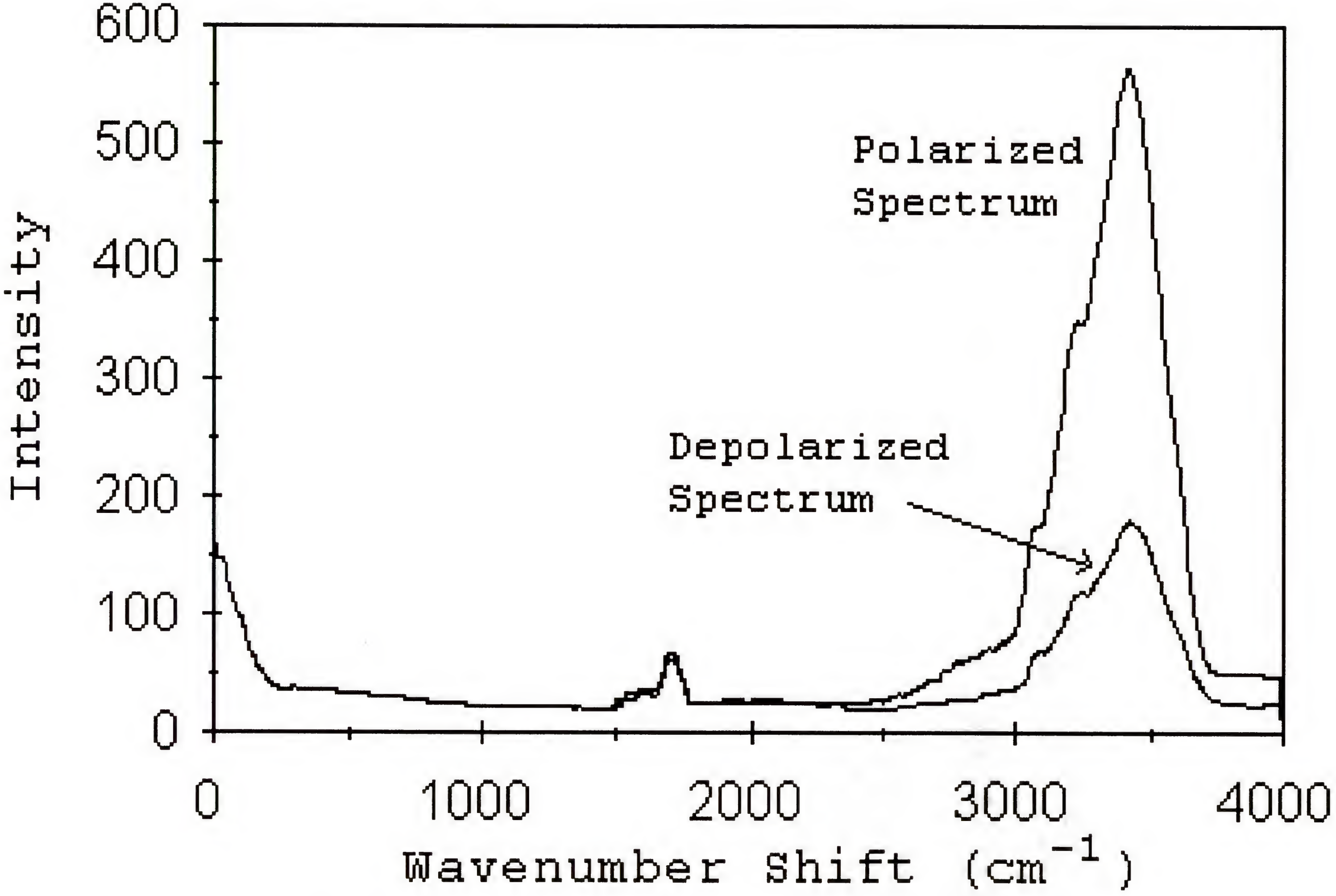

Figure 3-12. Comparison of polarized and depolarized spectra for $H_2O(l)$ at 25 °C.

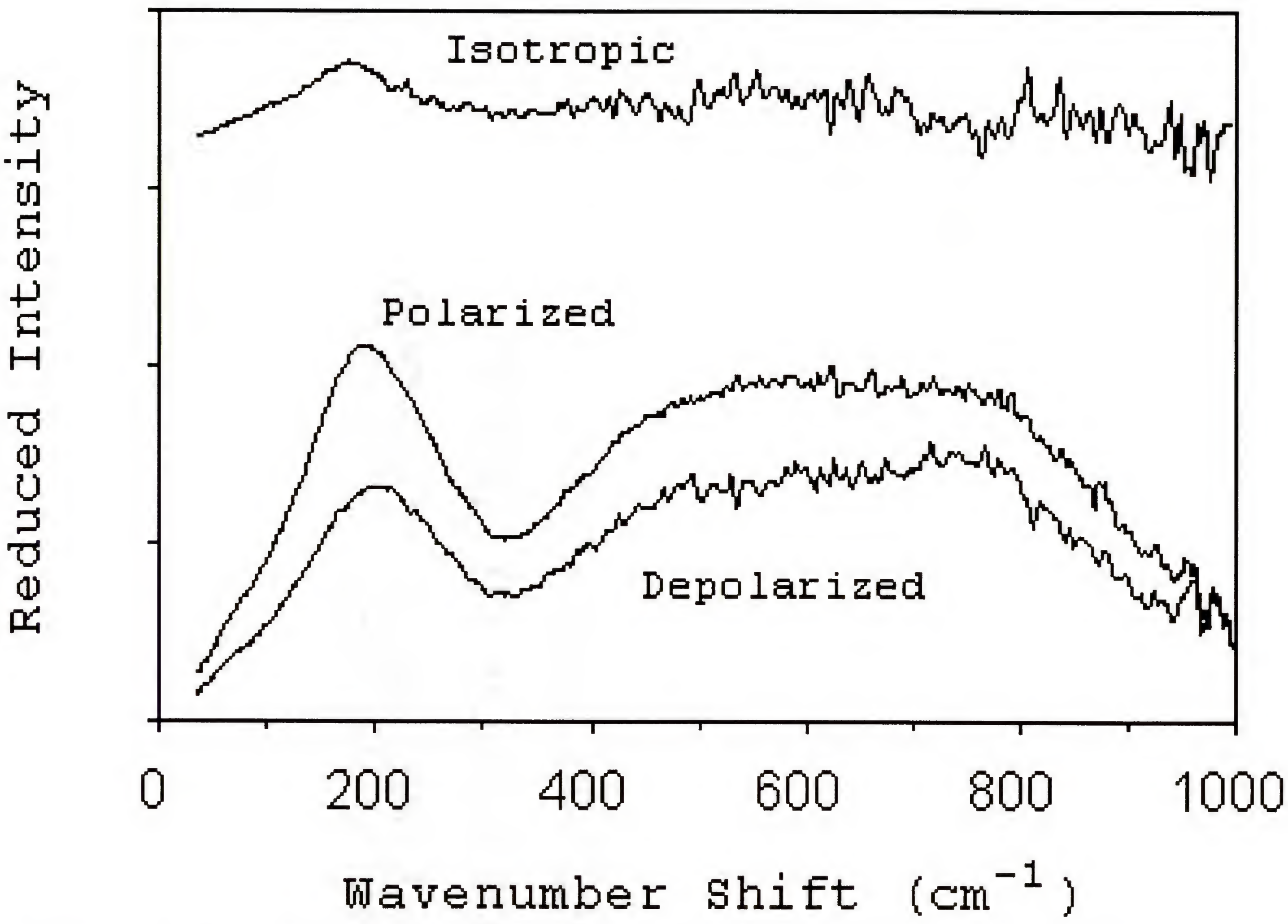

Figure 3-13. Reduced Spectrum of $H_2O(l)$ resolved into its components.

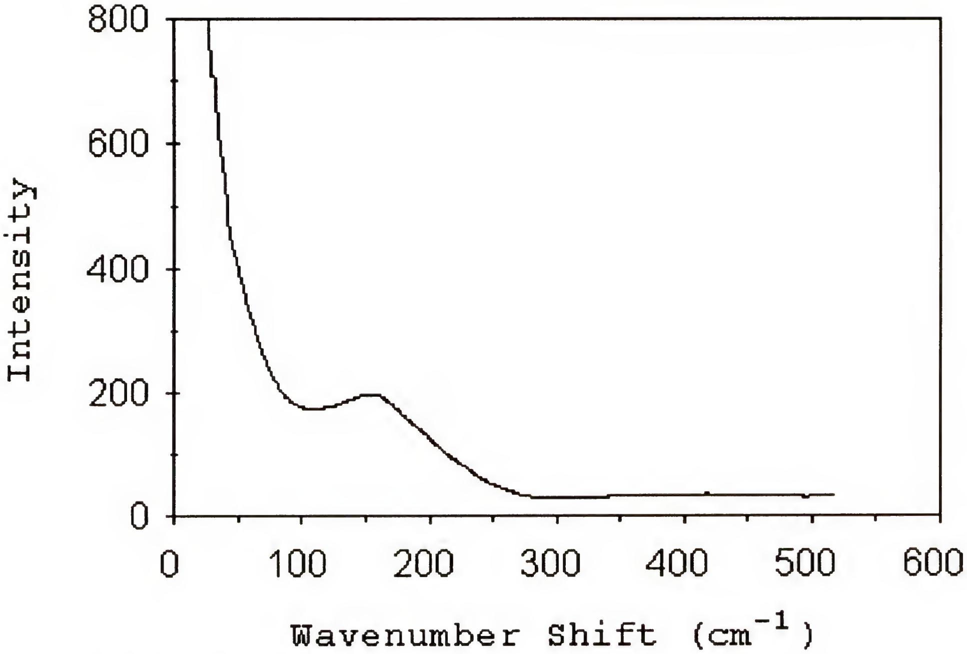

Figure 3-14. Low wavenumber depolarized Raman scattering spectrum of H_2O(l) at 2 °C.

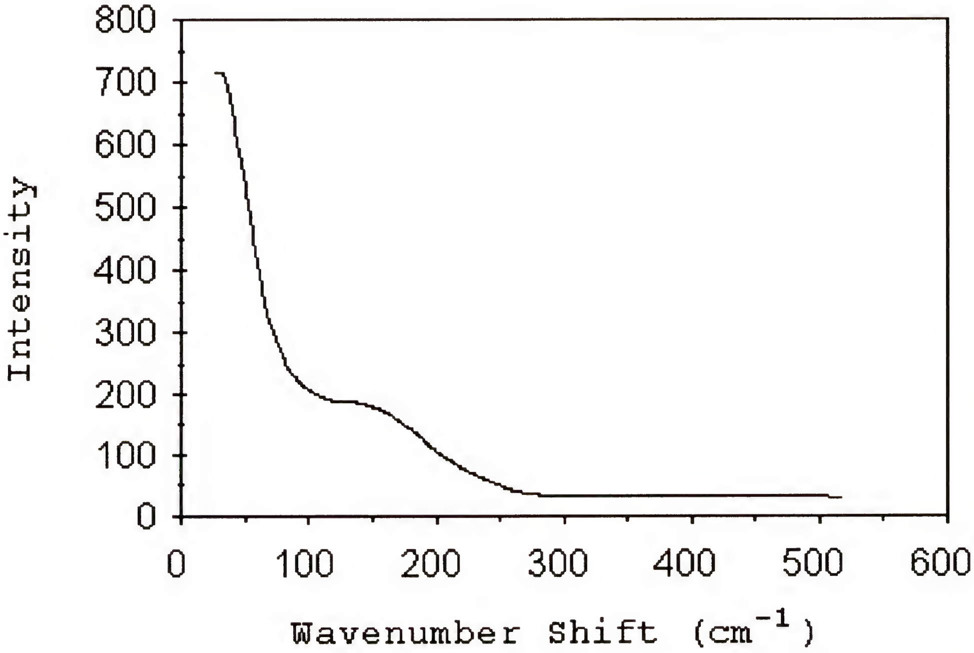

Figure 3-15. Low wavenumber depolarized Raman spectrum of H_2O(l) at 8 °C.

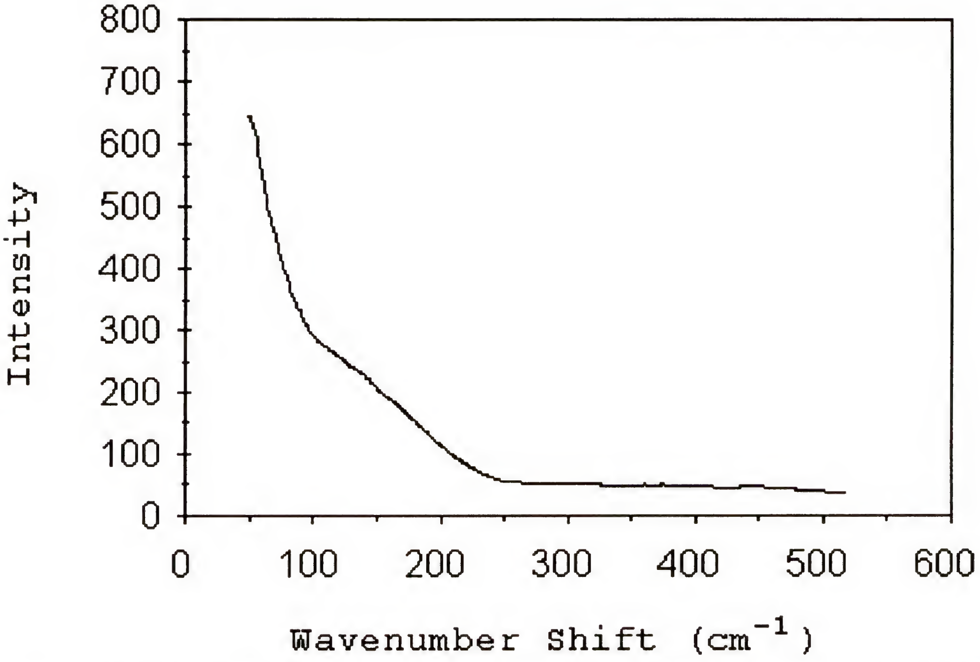

Figure 3-16. Low wavenumber depolarized Raman spectrum of $H_2O(l)$ at 15 °C.

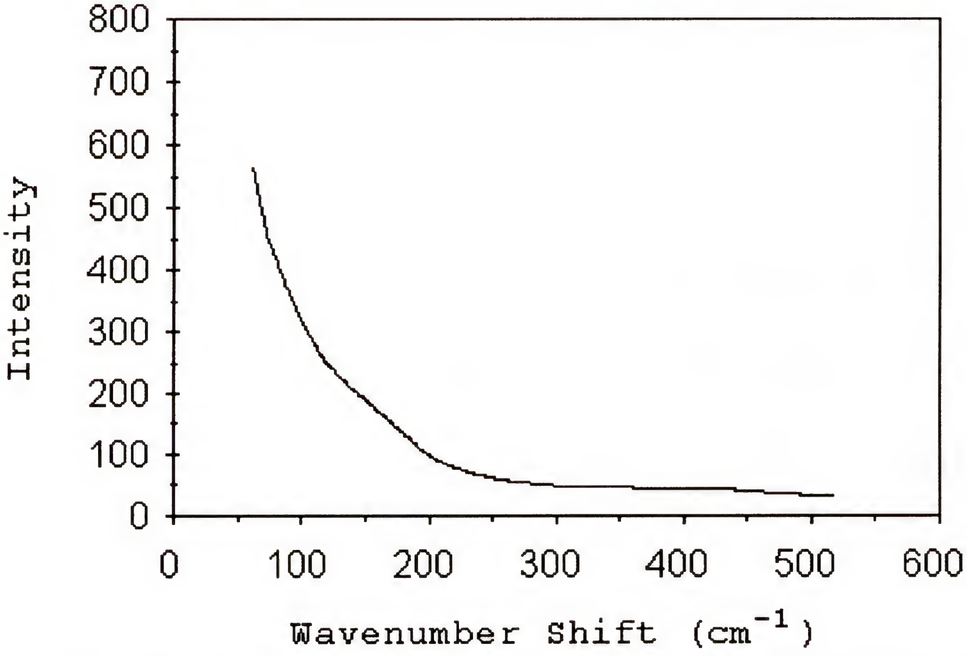

Figure 3-17. Low wavenumber depolarized Raman spectrum of $H_2O(l)$ at 25 °C.

The pressure and temperature measuring devices were interfaced to the micro-computer via the IEEE general purpose interface bus. All data were acquired with computer programs written specifically for these experiments in ANSI C standard code.

Temperature control was performed by a Fisher Scientific Chiller capable of controlling the coolants temperature to ±0.1 K. All actual temperature measurements were performed using the RTD immersed in the sample.

Gases and Chemicals

Doubly-distilled water from a MilliPore Milli-Q UV Plus UltraPure Water System was used after degassing. Methane and gas was obtained from Scott Specialty Gases and had a purity greater than 99.99 mole percent. The carbon dioxide gas was also obtained from Scott Specialty Gases and also had a purity greater than 99.9 mole percent. Both were used without further treatment. Tetrahydrofuran (spectroscopic grade) was obtained from Aldrich Chemical Company and used after degassing.

Representative Spectra

Light Scattering from Water

Because clathrate hydrates can be regarded as a distorted form of ice, liquid water and ice serve as particularly important benchmark systems. Furthermore, several spectroscopic studies of these systems are present in the literature which enabled confirmation that the Raman apparatus was performing adequately.

Figure 3-10 contains the light scattering spectrum of liquid water at 25 °C and it is decomposed into its polarized and depolarized components in Figure 3-12. Some general observations may be made though a more detailed discussion will be reserved for Chapter 5.

The large wavenumber region of the spectrum may be attributed primarily to intramolecular vibrations perturbed by intermolecular coupling. The water monomer has three normal modes of vibration, which are illustrated in Figure 3-12. These are: the H-O-H bending (occuring at approximately 1595 cm^{-1} in the gas phase), the assymetric stretch in which proton motions are out of phase (3756 cm^{-1} in the gas phase), and symmetric stretching motion in which the protons move in phase (3562 cm^{-1} in the gas phase). All three modes are broadened considerably and shifted by intermolecular interactions in the liquid phase: The region from 1625 - 1644 cm^{-1} corresponds to the H-O-H bending motion while the large, broad peak in the 3000-3800 cm^{-1} region corresponds to the two types of OH stretching motion. When the data for this peak are plotted over a smaller wavenumber range, this peak can be seen to contain structure indicating the strength and type of intermolecular interactions present in the liquid and the analysis of this spectral region along these lines is an important part of Chapter 5.

The wide wavenumber range in these figures, together with the intense and broad Rayleigh scattering, tends to obscure the features in the low wavenumber region. Consequently, this section, decomposed into its components, is plotted as the reduced intensity in Figure 3-13. The broad, nearly featureless, increase in intensity extending from around 400 cm^{-1} to 1000 cm^{-1} can be attributed to the librational or restricted rotational motions of the H_2O molecules.

Walrafen's classic review of Raman scattering in water demonstrated that this region can be decomposed into three broad Gaussian components centered near 425, 550, and 740 cm^{-1}. The three components loosely correspond to the rotational modes of the monomer though they are strongly perturbed by the restraints imposed by hydrogen bonds present in the liquid phase.

Hydrogen bond stretching and bending motions give rise to additional weak bands below 300 cm^{-1}. These may be regarded as restricted translational modes of motion since they primarily involve movement of the much heavier oxygen atoms. There is a distinct peak centered near 200 cm^{-1}, corresponding to the stretching motions of O-H units, and one that is much less obvious near 90 cm^{-1} produced by the bending of such units.

Considerable controversy still exists over the interpretation of features closer to the Rayleigh line. However, we may safely avoid this region by noting that the experimental results reported here do not permit the extremely high resolution distinctions that will be required to resolve the debate.

The importance of the low wavenumber region lies primarily in the information it contains concerning the restrictions placed by intermolecular forces on rotational and translational motion. Representative spectra showing the temperature dependence of the low wavenumber depolarized light scattering are presented in Figures 3-14 through 3-17. The decrease in intensity with temperature has been interpreted in terms of a breakdown of hydrogen bonding.

The Water/ Tetrahydrofuran System

The other important benchmark, for a particular hydrate forming system, is the light scattering spectra of the pure former. Figure 3-18 displays the spectrum for pure tetrahydrofuran (THF) liquid. The high wavenumber region again contains features attributable to intramolecular vibrations. C-O-C ring stretch is responsible for the spectral features occuring between 850 and 920 cm^{-1}. Specifically, the sharp peak at 913 cm^{-1} is due to the C-O-C symmetric stretch.

Various CH_2 bend motions are responsible for the complex of peaks that appear between 940 and 1600 cm^{-1}. The intense peak at 2800 cm^{-1} is the result of CH stretching motions.

A representative spectrum of an aqueous solution of THF is given in Figure 3-19. At first glance it appears very much like simply the superposition of the pure water and pure THF spectra, which is not suprising since THF is completely miscible in water. However, there are subtle changes changes in the CH_2 bending and CH stretch regions which become more apparent when they are plotted over a narrower wavenumber range and analyzed quantitatively. The changes in the water OH stretching regions are rather obvious, indicating changes in intermolecular interaction.

Figures 3-19 through 3-21 are included to show the dependence of the spectra on solution composition and the temperature dependence of these spectra are indicated by Figures 3-21 through 3-23. These may be compared to the spectra of the solid clathrate presented in Figures 3-24 and 3-25. Figures 3-26 and 3-27 shows the decomposition of a pure THF spectrum according to polarization. The analogous spectra for the THF/water system is given in Figures 3-28 and 3-29. It will be argued in Chapter 5 that a quantitative analysis of these spectra reveal a great deal of information concerning the changes in intermolecular interactions that are the result of changes in the composition and temperature of the system.

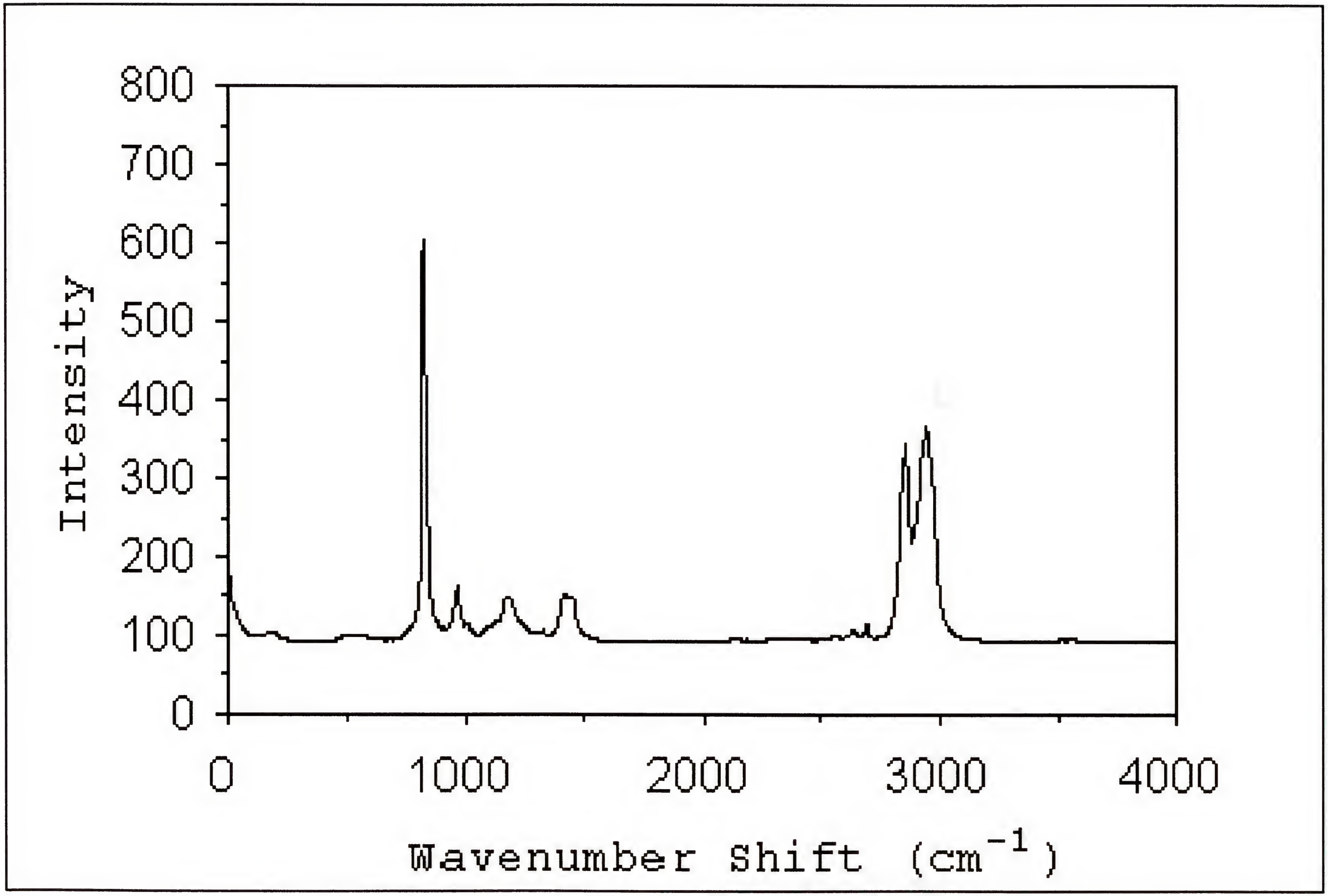

Figure 3-18. Scattering from pure THF(l) at 25 °C.

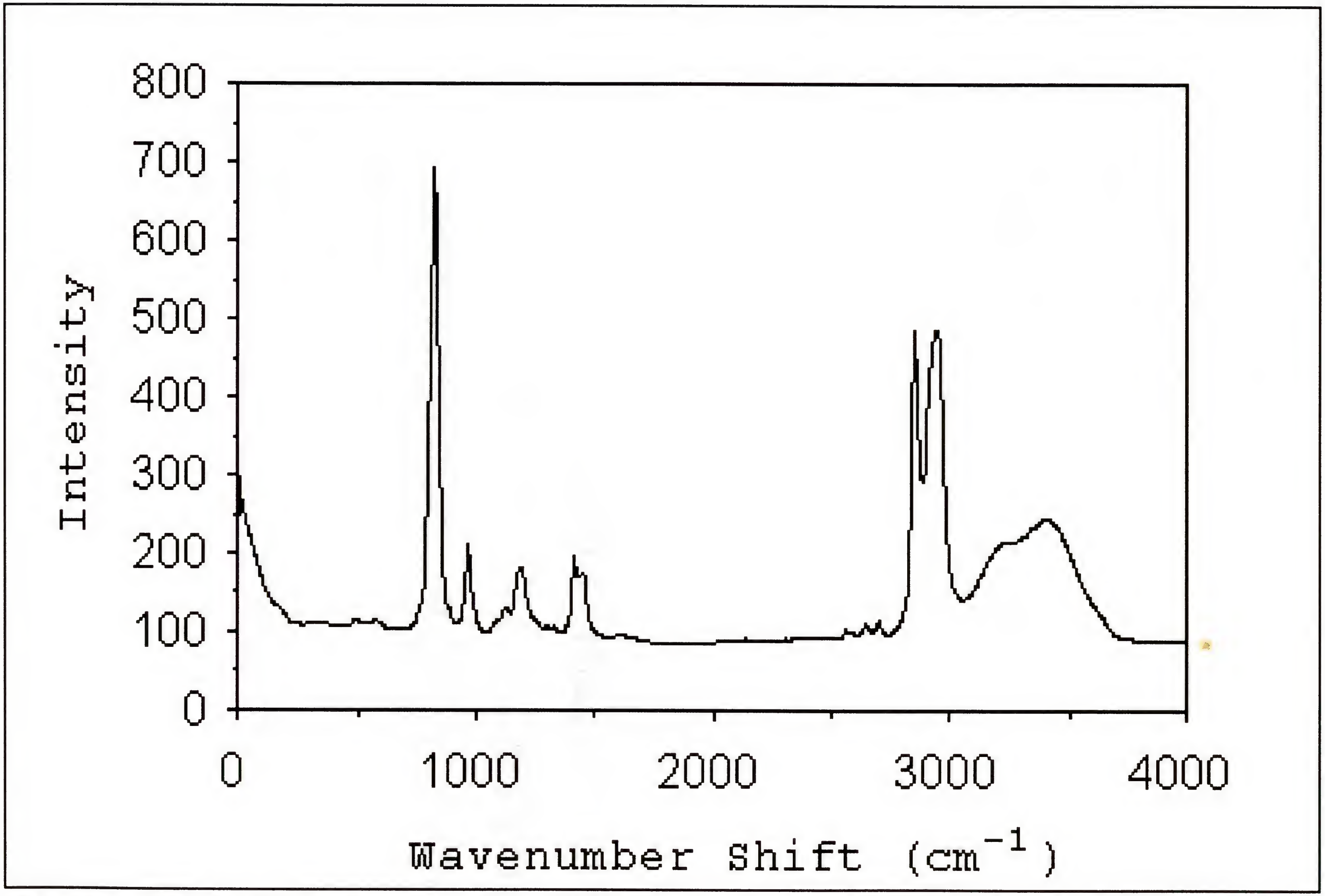

Figure 3-19. Light scattering from THF/H_2O solution at 25 °C (0.11 mole fraction THF).

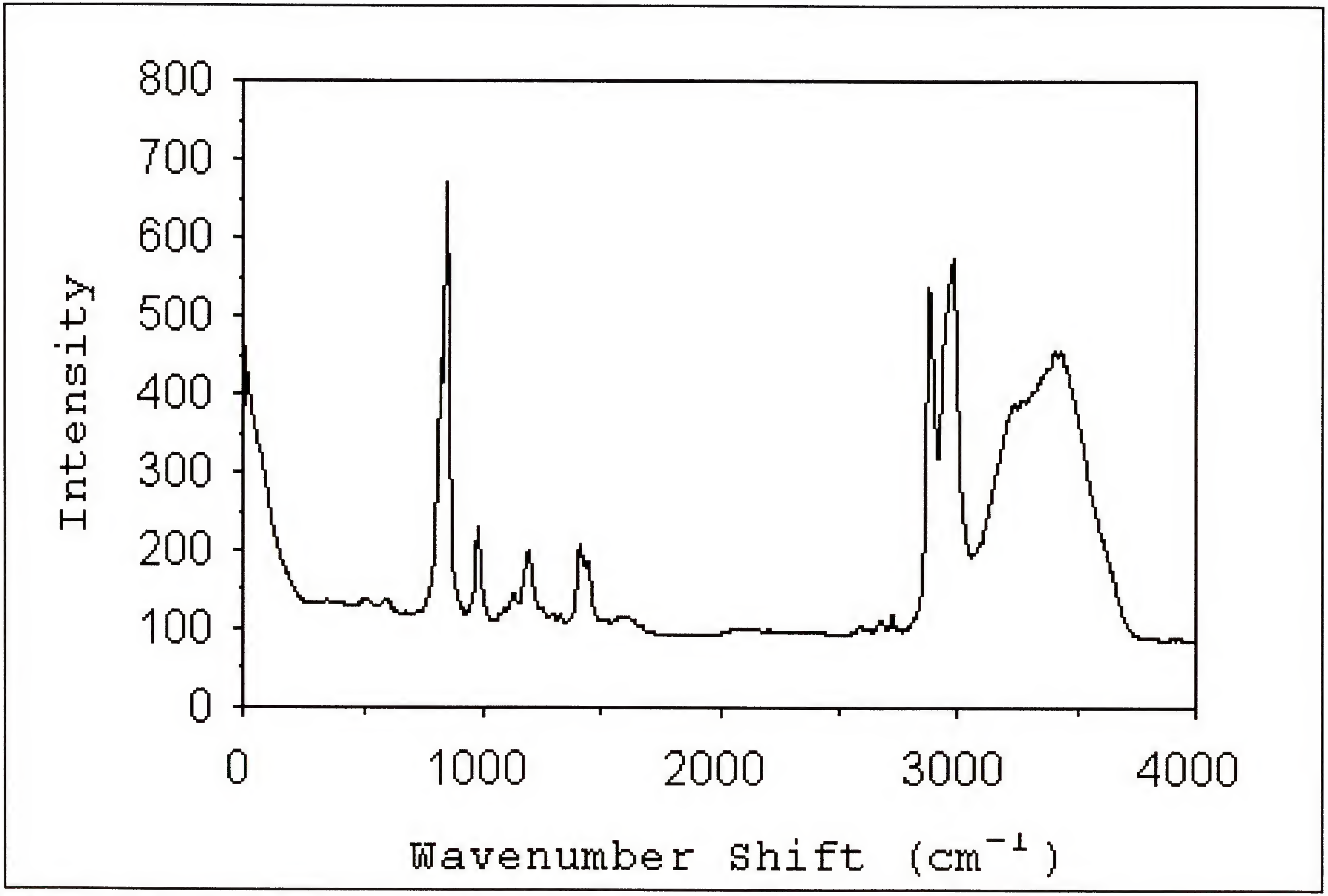

Figure 3-20. Light scattering from THF/H_2O solution at 25 °C (0.056 mole fraction THF).

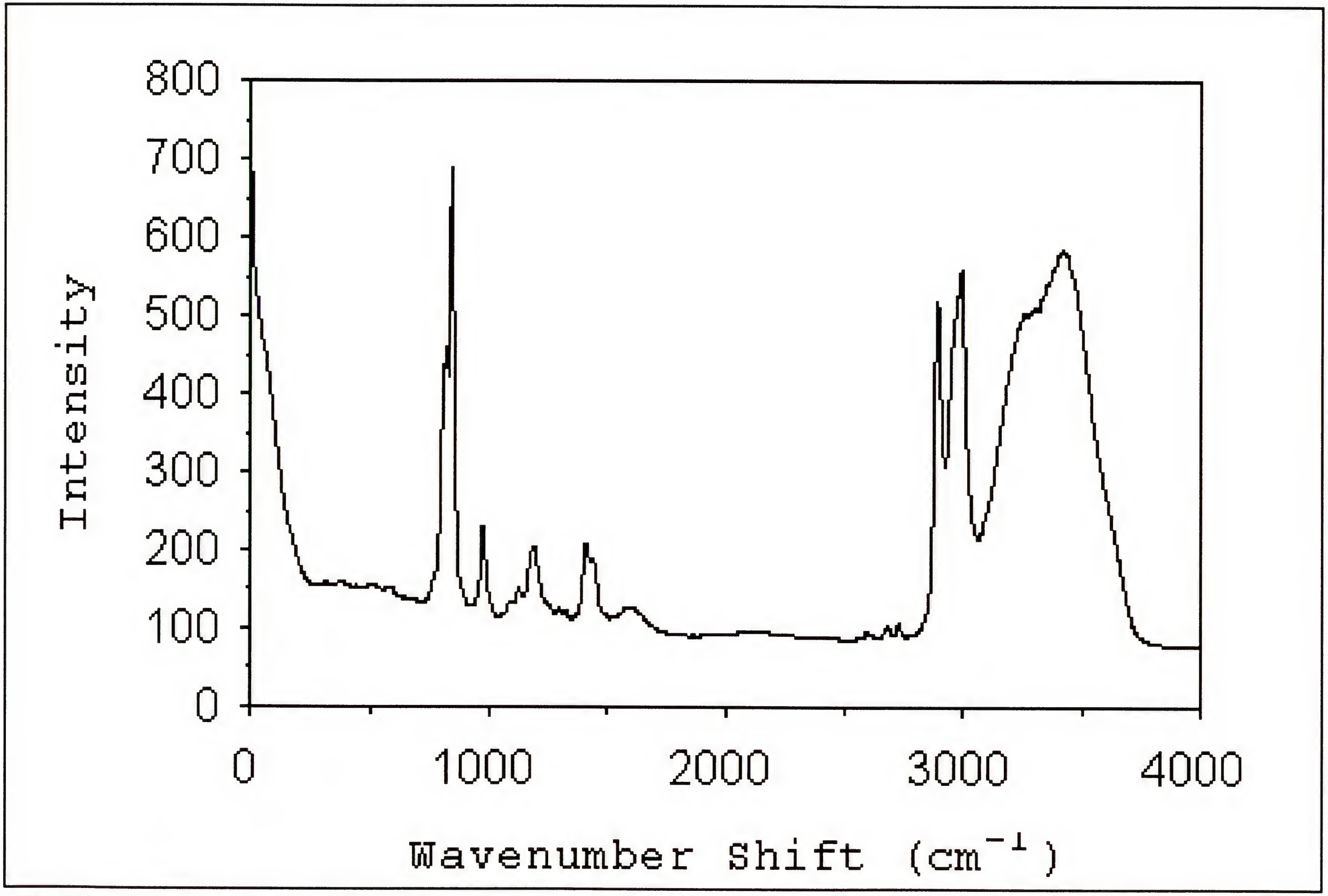

Figure 3-21. Light scattering from THF/H_2O solution at 25 °C (0.04 mole fraction THF).

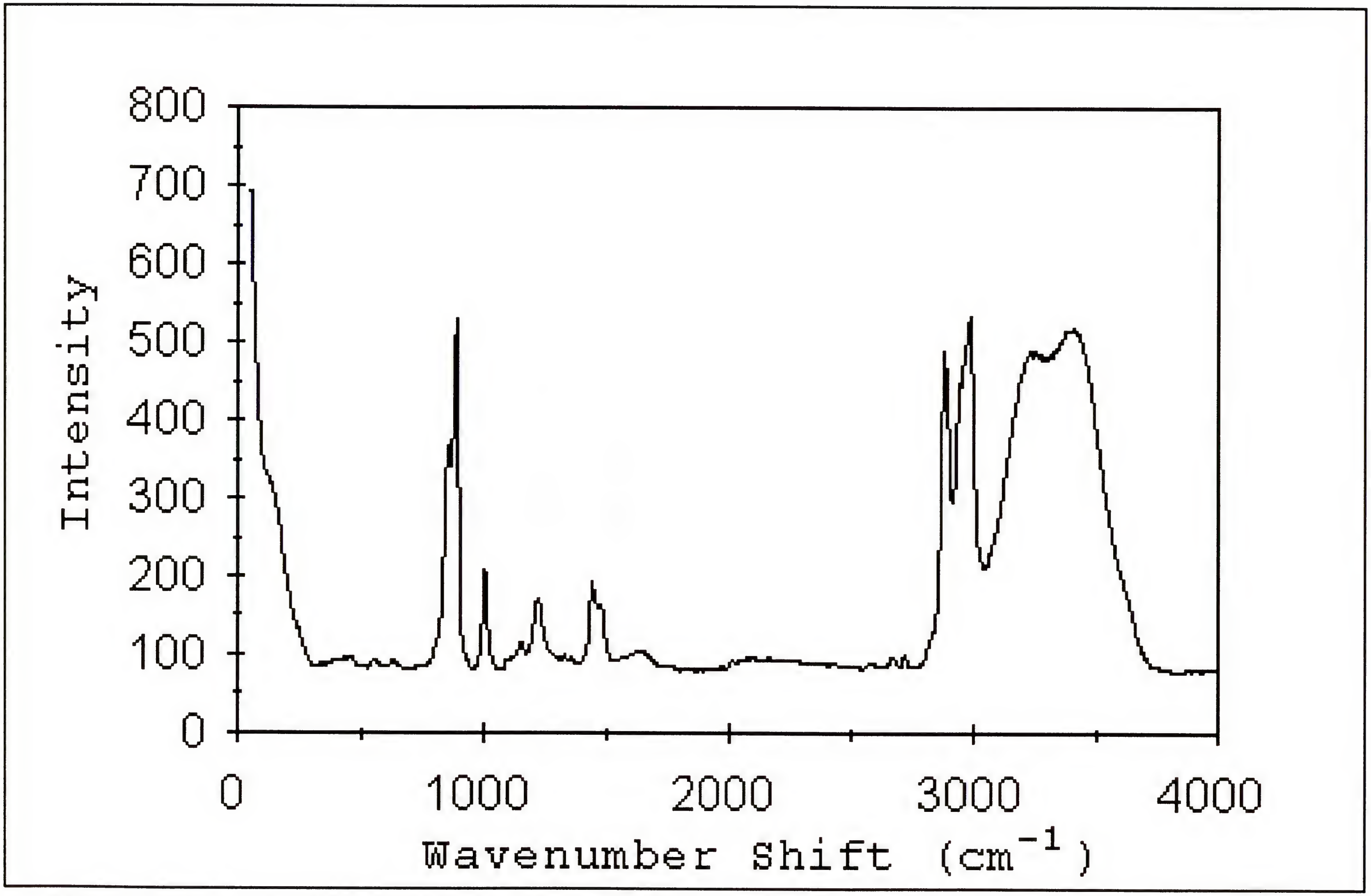

Figure 3-22. Light scattering from THF/H_2O solution at 10 °C (0.056 mole fraction THF).

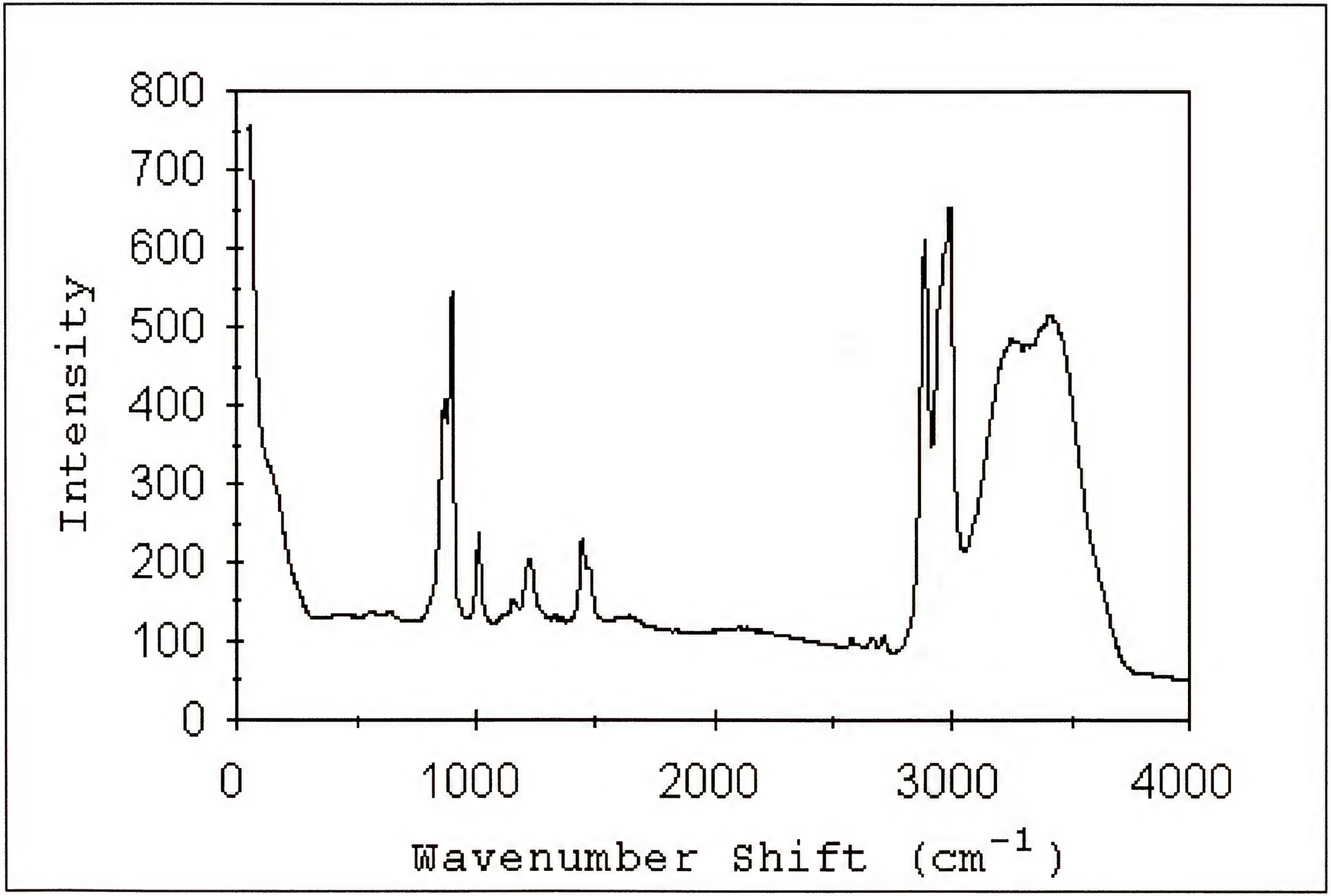

Figure 3-23. Light scattering from THF/H_2O solution at 6 °C (0.056 mole fraction THF).

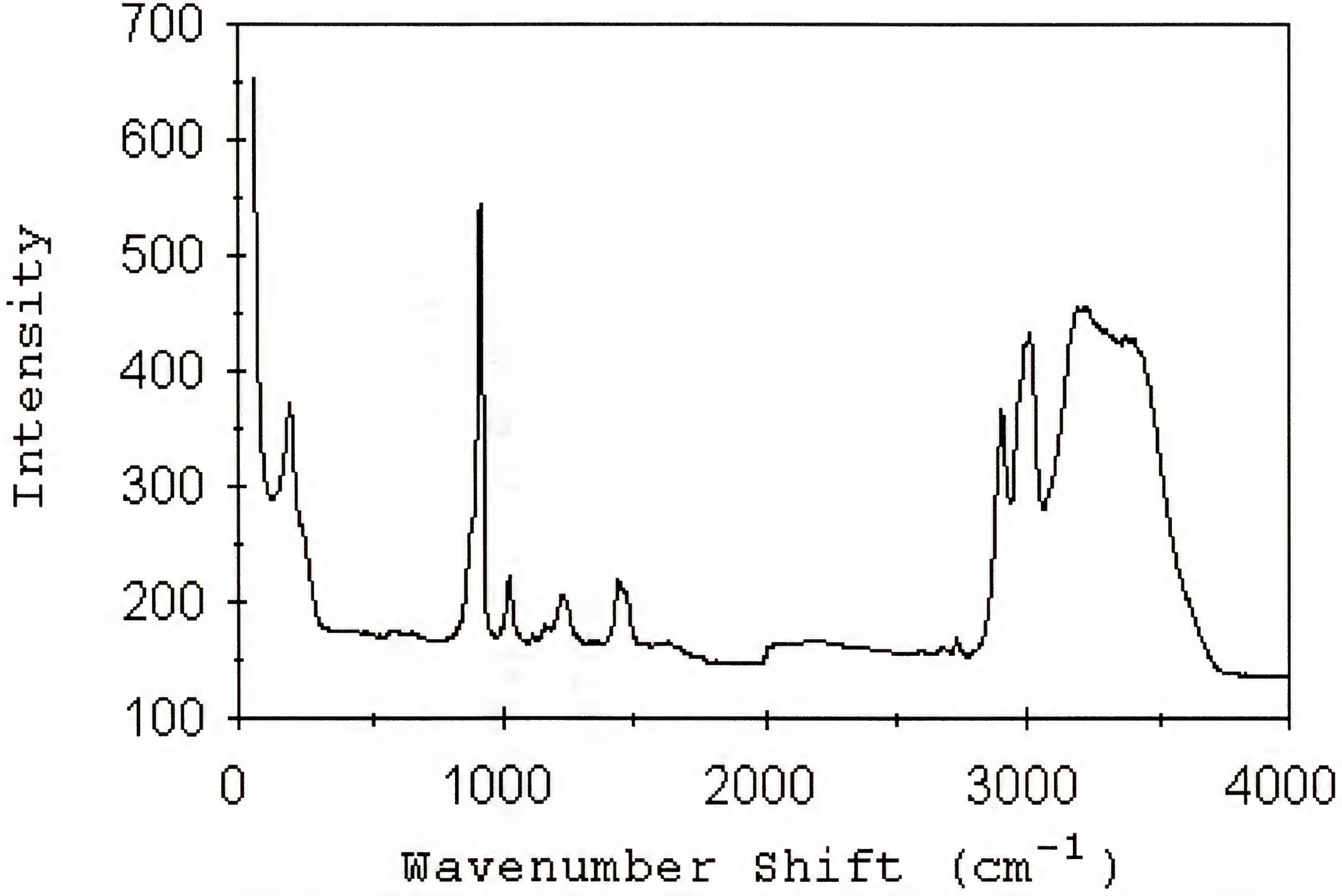

Figure 3-24. Light scattering from THF clathrate hydrate at 3 °C.

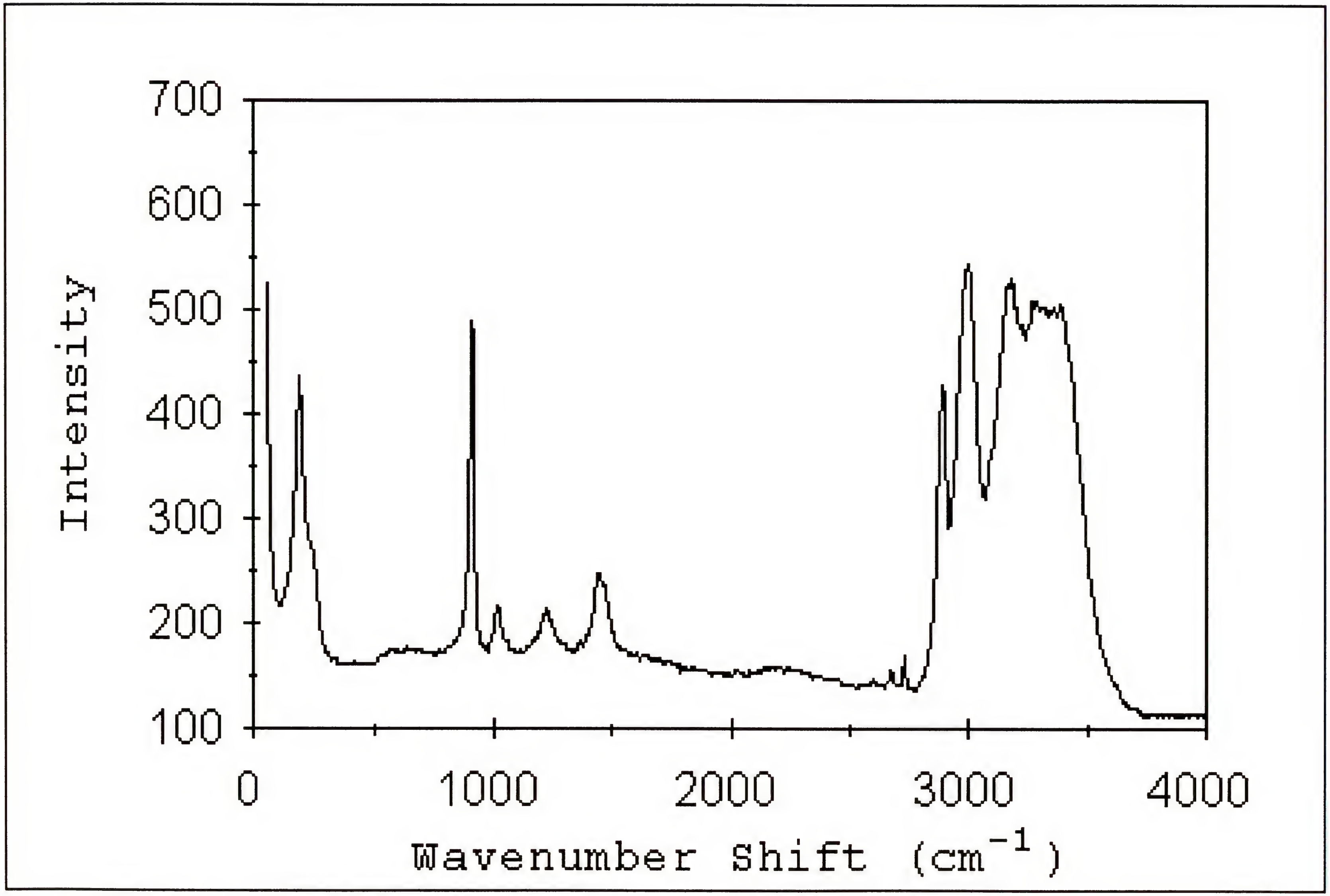

Figure 3-25. Light scattering from THF clathrate hydrate at -2 °C.

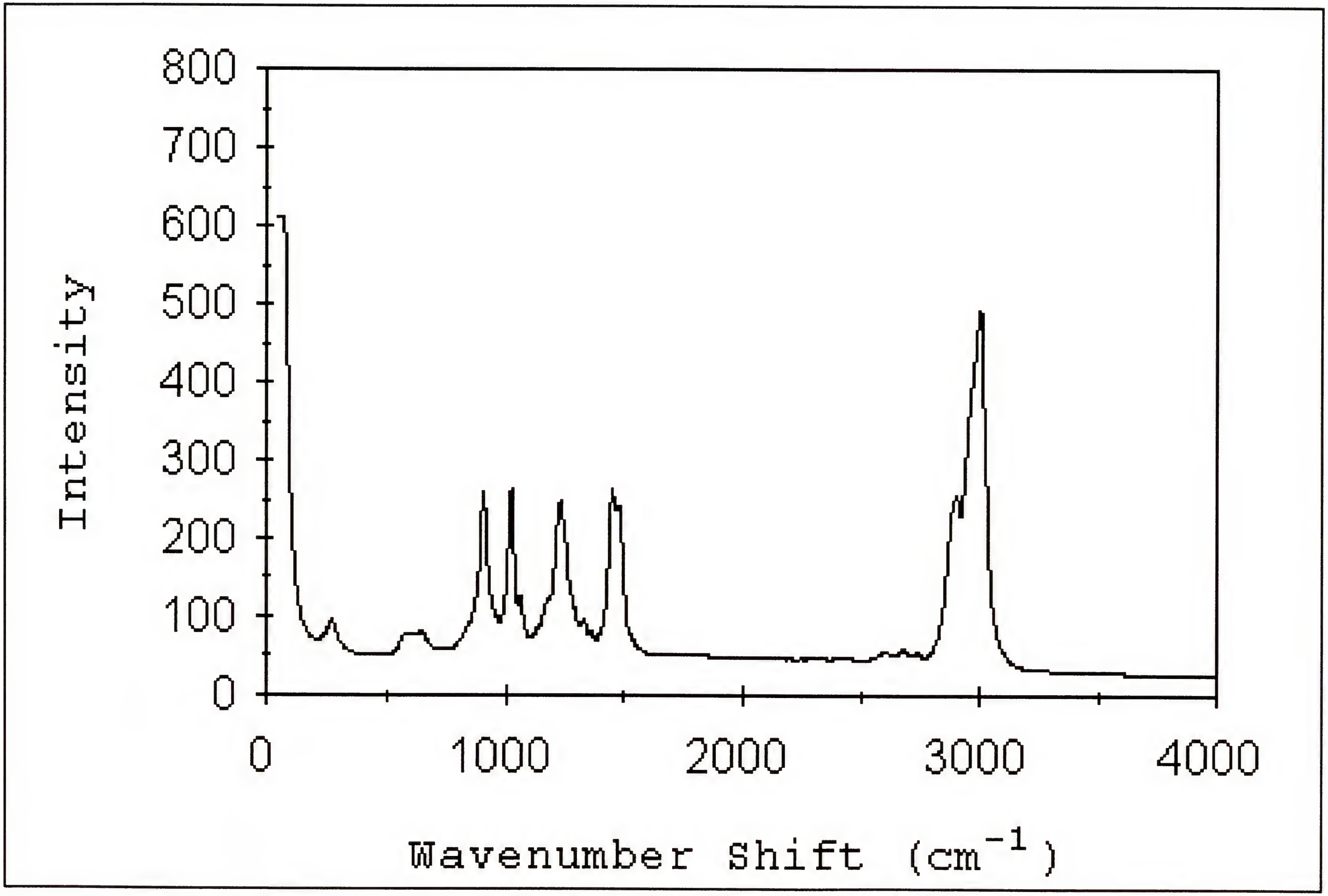

Figure 3-26. Depolarized spectrum of THF at 25 °C.

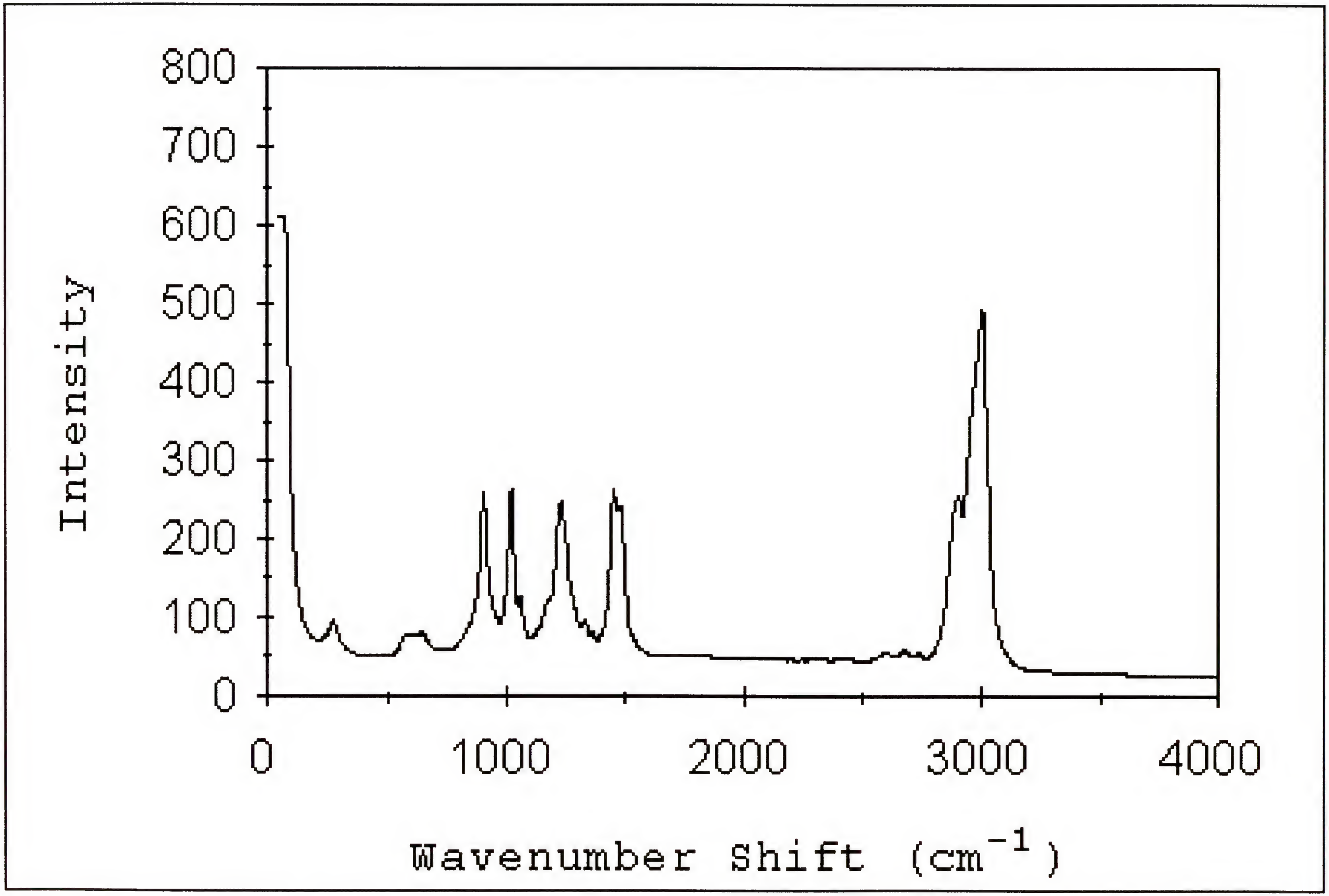

Figure 3-27. Polarized spectrum of THF at 25 °C.

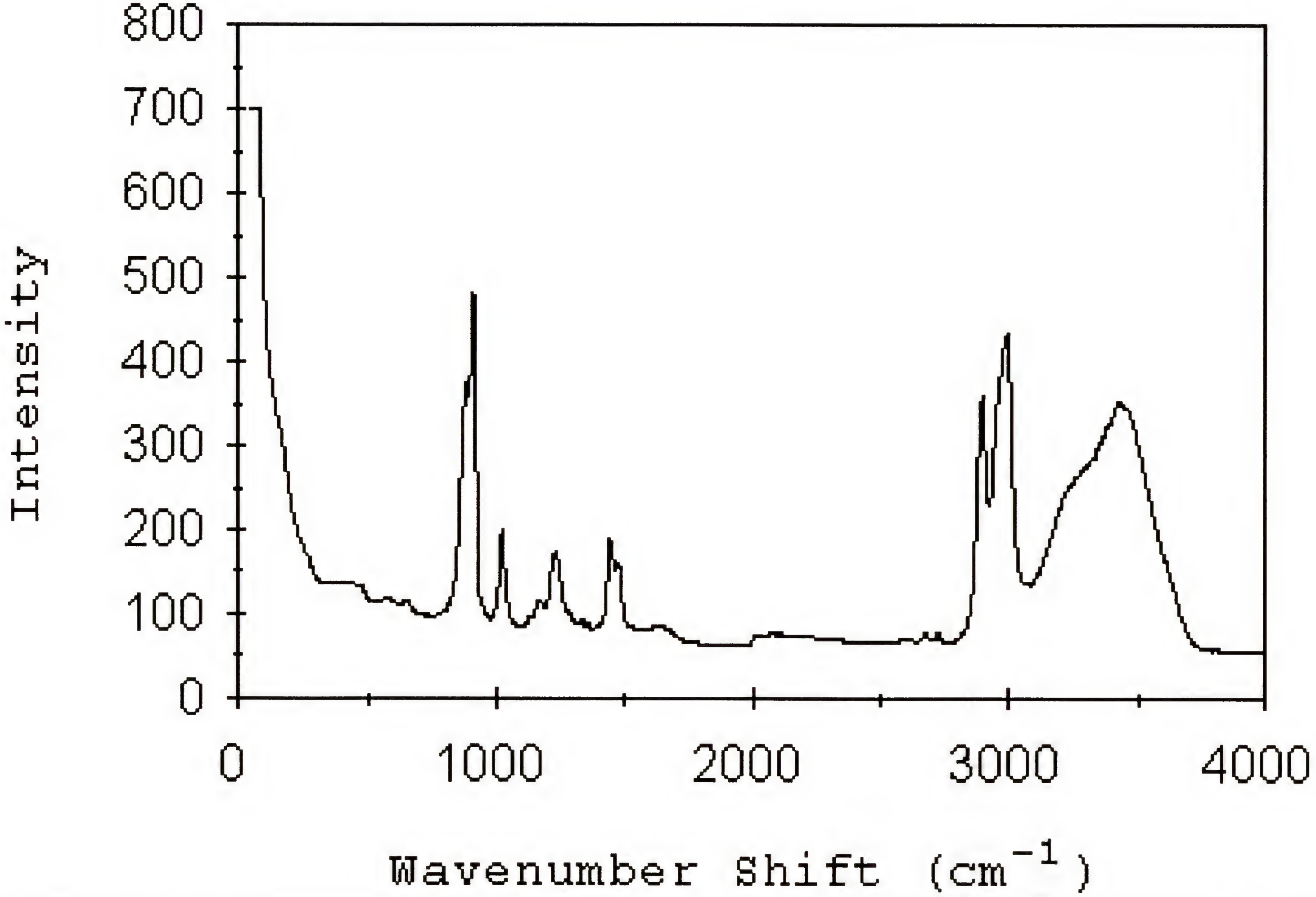

Figure 3-28. Depolarized spectrum of THF/H_2O solution at 25 °C (0.056 mole fraction THF).

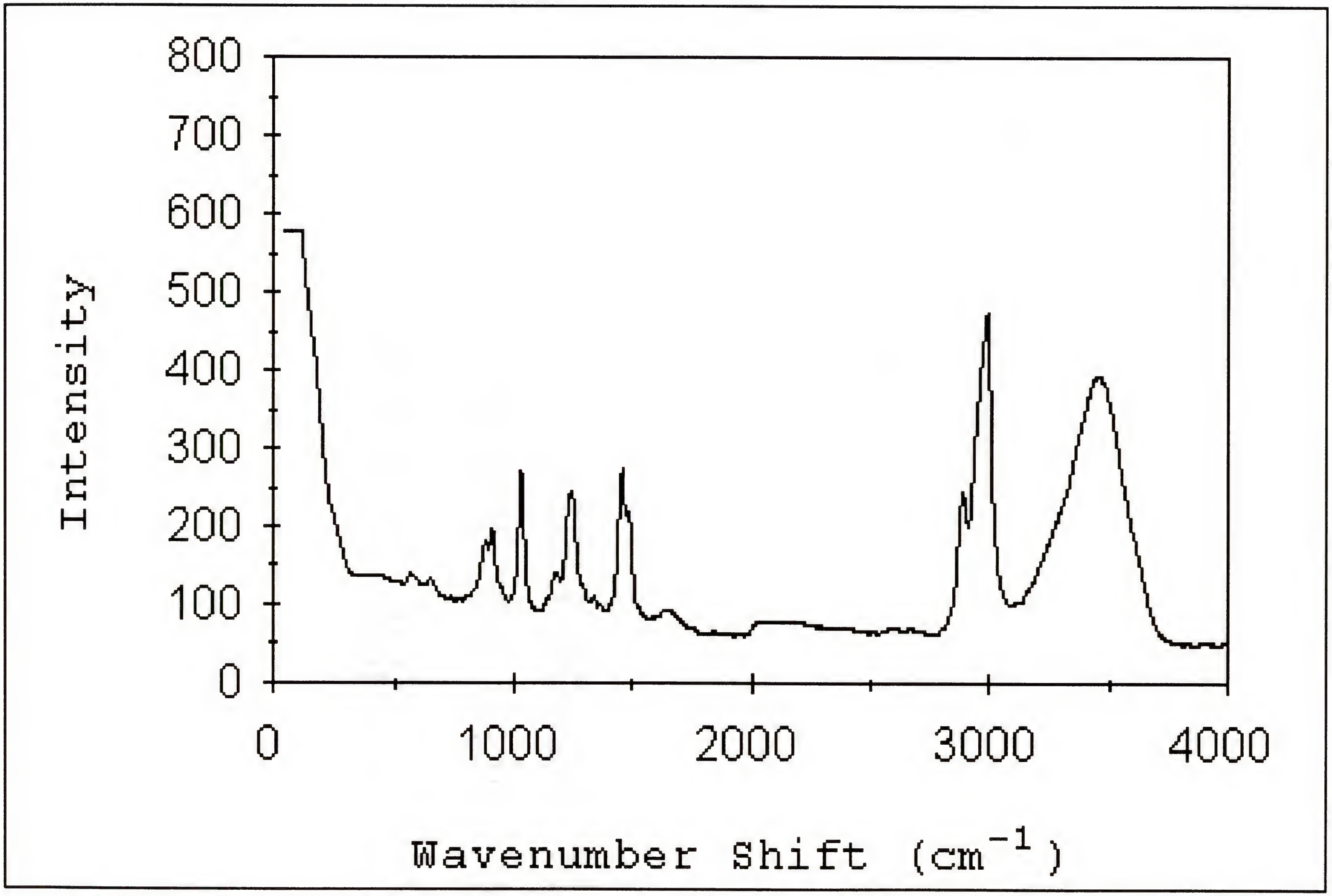

Figure 3-29. Depolarized spectrum of THF/H_2O solution at 25 °C (0.056 mole fraction THF).

CHAPTER 4
MOLECULAR DYNAMICS SIMULATIONS

Software and Algorithms

All molecular dynamics (MD) simulations were performed using modules from the TINKER[49] package of source code. After some modifications, the code was compiled and run under the Linux operating system on a pentium PC. Although some features of the software package are incomplete, those features primarily pertain to the simulation of large molecules of biological significance and were not required for the studies reported here; the modularity of the code permits one to avoid those features entirely. A user interface was written using C and the Tk/Tcl toolkit and all analysis programs were written by this author in C.

The equations of motion for the molecular centers of mass and their orientations (quaternions) were integrated using the velocity Verlet algorithm[50] The electrostatic forces and energies were evaluated by the Ewald method[50] while Lennard-Jones interactions were set equal to zero for intermolecular separations greater than half the length of the simulation cell.

Intermolecular Potentials

A wide variety of intermolecular potentials have been proposed to model water, and the choice of one requires some defense. The simulations reported here used the simple point charge (SPC) model introduced by Berendsen[51]. This is a semi-empirical model with parameters determined by fitting the internal energy and pressure of liquid water to the experimental values at 300 K, and with the further restriction that the model adequately approximate the measured oxygen-oxygen distribution.

The simplicity of the model makes it attractive from a computational standpoint and the SPC model is one of only a handful that have been found to adequately describe the static properties of different polymorphic forms of ice.[52] Furthermore, the model has been successfully used by others to simulate solid clathrate hydrates[53].

The SPC model consists of three point charges placed on the atomic centers with the oxygen centers interacting through a Lennard-Jones potential; the water molecule is rigid and no account is taken of any short-range H-H or O-H forces.

Water-guest and guest-guest interactions are treated in a similar manner with each guest treated as a rigid molecule possessing a number of Lennard-Jones and electrostatic interaction sites. Ethylene oxide was represented by three interaction sites; two methylene groups centered on the carbon atoms and the etheric oxygen atom. Electrostatic parameters are those reported by Tse et al[54] and were evaluated from the known dipole moment and structure of the molecule. The Lennard-Jones interaction parameters were obtained from the same source and were those used in the TIPS2 model of Jorgensen.

Methane was represented by five coulombic interaction sites and a single Lennard-Jones site; the relevant parameters are also from Tse et al and were estimated from data on krypton which has a solid state lattice spacing and binding energy similar to methane. Guest-water interaction parameters were obtained using the Lorenz-Berthelot mixing rules

$$E_{ij} = [E_{ii} \cdot E_{jj}]^{1/2} \qquad [4\text{-}1]$$

$$\sigma_{ij} = \frac{1}{2}[\sigma_{ii} + \sigma_{jj}] \qquad [4\text{-}2]$$

The intermolecular potential between two molecules m and n, U_{mn}, is given by

$$U_{mn} = 4\epsilon[(\frac{\sigma_{mn}}{r_{mn}})^{12} - (\frac{\sigma_{mn}}{r_{mn}})^{6}] + \sum_{i}^{on\ m} \sum_{j}^{on\ n} \frac{q_i q_j e^2}{r_{ij}} \qquad [4\text{-}3]$$

and all parameters are reported together in Table 4-1.

Table 4-1. Intermolecular Potential Parameters

Lennard-Jones Parameters

Interaction	**σ/ Å**	**4ε /kJ mol^{-1}**
Water O-O	3.16	2.60
Ethylene Oxide O-O	3.05	3.27
Ethylene Oxide CH_2-CH_2	3.98	1.91
Methane C-C	3.64	5.46
Methane-Water CH_4-O	3.33	3.05

Electrostatic Parameters

Site	**Charge / e**
Water O	-0.82
Water H	0.41
Ethylene Oxide O	-0.32
Ethylene Oxide CH_2	0.16
Methane C	-0.56
Methane H	0.14

Table 4-2. Asymmetric Residue Unit for Host Lattice of SI Clathrate Hydrates[55].

Lattice Parameter: 12.0 Å (cubic)
Space Group: Pm3n

Atom	**x**	**y**	**z**	**Population**
O_i	0.18375	0.18375	0.18375	1
O_k	0.0	0.30822	0.1173	1
O_c	0.0	0.5000	0.2500	1
H_{ii}	0.2323	0.2323	0.2323	0.5
H_{ck}	0.0	0.43404	0.2015	0.5
H_{kc}	0.0	0.37874	0.1588	0.5
H_{kk}	0.0	0.31614	0.0357	0.5
H_{ki}	0.0676	0.26483	0.1397	0.5
H_{ih}	0.1170	0.22763	0.1588	0.5

Oxygen atom indices *c, i, k* refer to the symmetry sites. H_{ck} is the site of a proton which is covalently bonded to O_c and hydrogen-bonded to O_k.

Notation from: International Tables for X-ray Crystallography (Kynoch Press, Birmingham England, 1965), Vol. I.

Cluster Simulation Details

Simulations were performed for water clusters of various sizes near room temperature. The clusters were not confined and periodic boundary conditions were not imposed. Thus, they were free to dissociate though this did not occur in any of the simulations reported here.

Initial configurations for the smaller clusters (N=2, 5, 8) were chosen from published reports of local minima configurations. The larger clusters (N=20, 50) were arranged as fragments of hexagonal ice. It should be noted that the spectra calculated here have been generated using a single, though long, MD run; thus it is possible that the lower-temperature clusters may not have had enough energy to isomerize and may not represent the complete distribution of cluster geometries.

The atomic configurations so obtained were then adjusted to the HOH bond angle and OH bond length required by the SPC model. The simulated sample was then heated by uniformly increasing the velocities of each molecule to produce a temperature increase of 0.02 K fs^{-1} followed by a 10,000 MD step equilibration period (10 ps) every 20 K. This sequence was repeated until the desired temperature was obtained whereupon the system was again allowed to equilibrate for 10,000 steps. The dynamics were then followed for 32768 steps

(~30 ps) by saving configurations every eight steps. Cluster temperatures were calculated according to,

$$T = \left(\frac{3N}{3N - 6}\right)\left(\frac{2}{3k}\right)\left\langle\frac{1}{N}\sum_i \frac{1}{2}m_i v_i^2\right\rangle \qquad [4\text{-}4]$$

Unlike the bulk simulations, the clusters were permitted to evolve without thermal interference and may be considered constant energy systems, i.e., while the initial temperature was deliberately chosen, it was not maintained during the simulation.

Bulk Simulation Details

MD simulations were performed for Canonical ensembles (constant NVT) of water, ethylene oxide/water, and methane/water. Random initial configurations were used for the water simulations, while the SI x-ray results of Jeffrey et al[55] were used to obtain initial configurations for the ethyelene oxide and methane simulations. Asymmetric residue units are reported in Table 4-2 and the *discus*[56] software package was used to generate the full unit cell. The excess protons were then removed until the resulting configuration satisfied the correct valence of oxygen atoms and the correct proton placement according to the Bernal-Fowler ice rules[57].

Each sample for the bulk water simulations consisted of 256 molecules in a cubic simulation cell, 19.46 Å on edge. The methane/ water systems were simulated by cubic cells 24.6 Å on edge corresponding to eight SI unit cells; they contained 368 water molecules and 64 guest molecules which corresponds to the ideal clathrate stoichiometry. The initial configurations for the ethylene oxide/ water simulations are identical to those used for methane with the important exception that the guests are permitted to occupy only the larger cages as experimental studies have indicated.

Bulk simulations of the solid hydrates followed the same procedure, but with constant temperature conditions imposed during the data collection steps using the Gronigen method. These simulations were performed primarily for comparison with simulations performed by others.

Bulk simulations of the liquids began with a somewhat different heating procedure. The initial configurations were first heated by the same method used for the clusters to 400 K and equilibrated there for 10,000 steps to ensure melting. They were then cooled to the desired temperature and equilibrated further for 10,000 steps before the 32768 data collecting steps were performed during which the samples evolved subject to constant temperature conditions imposed using the Groningen method.

Spectral Calculations

From the discussion in Chapter 2, the expressions for the isotropic and anisotropic (depolarized) intensities are:

$$I_{iso}(\tilde{\nu}) = < |FT\ (\ \textstyle\sum_i \frac{1}{3}\sum_\alpha P^i_{\alpha\alpha}(t)\ )|^2 > \qquad [2\text{-}53]$$

$$I_{aniso}(\tilde{\nu}) = <|FT[\textstyle\sum_i \frac{1}{10}\sum_{\alpha\beta}\ [P^i_{\alpha\beta}(t) - \delta_{\alpha\beta}(\frac{1}{3}\sum_\gamma P^i_{\gamma\gamma}(t)\ )]]\ |^2 > \qquad [2\text{-}54]$$

These quantities were calculated from the configurations generated by the molecular dynamics simulations described in the preceding section. This requires the transformation of the body-fixed frame components of the susceptibility tensors into their laboratory-frame components which was performed using the body-fixed frame for water in which the principal moments of inertia are ordered $I_{11} < I_{22} < I_{33}$.

Three scalar quantities may be constructed from the components of $\boldsymbol{\alpha}$, specifically[58]:

$$\alpha_0 = \frac{1}{3}\ Tr[\alpha] \qquad [4\text{-}5]$$

i.e., the molecular isotropic point polarizability, and

$$\alpha_1 = \alpha_{33} - \frac{1}{2}[\alpha_{11} + \alpha_{22}] \qquad [4\text{-}6]$$

$$\alpha_2 = \frac{1}{2}[\alpha_{11} - \alpha_{22}] \qquad [4\text{-}7]$$

which are related to the optical anisotropy δ by

$$\delta^2 = \alpha_1^2 + 3\alpha_2^2 \qquad [4\text{-}8]$$

The molecular polarizability of the ith molecule in the laboratory frame may then be expressed as the sum of its trace and two traceless tensors, $\mathbf{Q}_i$ and $\mathbf{R}_i$ according to:

$$\alpha^{i} = \alpha_0 \boldsymbol{I} + \alpha_1 \boldsymbol{Q}^{i} + \alpha_2 \boldsymbol{R}^{i} \qquad [4\text{-}9]$$

where

$$Q^{i}_{\alpha\beta} = e^{i}_{3\alpha} e^{i}_{3\beta} - \frac{1}{3}\delta_{\alpha\beta} \qquad [4\text{-}10]$$

$$R^{i}_{\alpha\beta} = e^{i}_{1\alpha} e^{i}_{1\beta} - e^{i}_{2\alpha} e^{i}_{2\beta} \qquad [4\text{-}11]$$

in which $e^{i}_{n\alpha}$ (n = 1,2,3) is the direction cosine of the n^{th} body-fixed axis of the i^{th} molecule with respect to the α-axis of the laboratory frame.

Observe that this permits all tensors in the '$\beta T\mu$' spectrum (see equation 2-52) to be represented as vectors directed as axis 2 in the body-fixed frame, that is,

$$ {}^{0}\mu^{i}_{\alpha} = {}^{0}\mu e^{i}_{2\alpha} \qquad [4\text{-}12] $$

$$ \sum_{\gamma} \beta^{i}_{\alpha\gamma\gamma} = \overline{\beta} e^{i}_{2\alpha} \qquad [4\text{-}13] $$

The contribution of the dipole-quadrupole polarizability were calculated from the components of **A** in the laboratory frame constructed from

$$ A_{\alpha\beta\gamma} = \sum_{n_1 n_2 n_3} e_{n_1\alpha} e_{n_2\beta} e_{n_3\gamma} A_{n_1 n_2 n_3} \qquad [4\text{-}14] $$

The values of ${}^{0}\mu$, β, and A are collected in Table 4-3. It should be noted that these simulations used the water polarizability components calculated by Huiszoon using *ab initio* methods[59]. The resulting polarizability tensor is significantly more anisotropic than the experimental values obtained by Murphy[60] and used by de Santis et al in their calculations of Raman scattering from simulated water. The more anisotropic tensor was found by Bosma et al[61] to give a much more realistic description of the scattering from librational modes.

The time evolution of the different polarizability terms may be followed along the molecular dynamics trajectory by constructing the signals[58]

$$ {}^{\alpha T\delta}S_{iso}(t) = \frac{1}{3}\alpha_0 \sum_i \sum_{j\neq i} \sum_{\alpha\beta} T^{(2)}_{\alpha\beta}(ij)\ [\alpha_1 Q^{i}_{\beta\alpha}(t) + \alpha_2 R^{j}_{\beta\alpha}(t) \qquad [4\text{-}17] $$

$$^{AL}S_{dep}(t) = \frac{1}{10}\sum_{\alpha\beta}\sum_{i}\,[\alpha_1 Q^{i}_{\alpha\beta}(t) + \alpha_2 R^{i}_{\alpha\beta}(t)] \qquad [4\text{-}15]$$

$$^{IDID}S_{dep}(t) = \frac{1}{10}\sum_{\alpha\beta}\sum_{i}\sum_{j\neq i} T^{(2)}_{\alpha\beta}(ij) \qquad [4\text{-}16]$$

for the allowed rotational and IDID contributions and

$$^{\alpha TA}S_{iso}(t) = \frac{1}{3}\alpha_0\sum_{i}\sum_{j\neq i}\sum_{\alpha\beta\gamma} T^{(3)}_{\alpha\beta\gamma}(ij)\;[A^{j}_{\alpha\beta\gamma}(t) + A^{j}_{\alpha\beta\gamma}(t)] \qquad [4\text{-}19]$$

$$^{\beta T\mu}S_{iso}(t) = \frac{1}{3}\sum_{i}\sum_{j\neq i}\sum_{\alpha\beta\gamma} \beta^{i}_{\alpha\alpha\beta}T^{(2)}_{\alpha\beta}(ij)\;\mu^{j}_{\gamma}(t) \qquad [4\text{-}18]$$

for the first isotropic contributions. It should be noted that the second order propagator, $\mathbf{T}^{(2)}$, is commonly referred to as the dipole propagator and may be written in the more familiar form[47]:

$$T^{(2)}(ij) = \frac{1}{|r^{3}_{ij}|}(3\hat{r}_{ij}\hat{r}_{ij} - \mathbf{I}) \qquad [4\text{-}20]$$

The individual spectra and their cross terms are calculated according to,

$$^{ab}I(\nu) = FT[\,^{a}S(t)]\cdot FT[\,^{b}S(t)]^{*} + c.c \qquad [4\text{-}21]$$

where a and b represent any of the spectral labels previously defined.

Results

Several atomic pair distribution functions were calculated in order to characterize structural features of the simulated systems. Though no simulations of liquid phase hydrate-forming systems have been found in the literature, published reports of solid hydrate simulations are available for comparison. Figure 4-1 reports the oxygen-oxygen host lattice pair distribution function, $g_{OO}(R)$, for the methane hydrate. It may be compared to Figure 4-2, from the simulation by Tse et al[49] who obtained comparable results. There follows Figure 4-3, and 4-4 which report the host lattice pair distribution functions $g_{OH}(R)$ and $g_{HH}(R)$ respectively.

Guest-host pair distribution functions were also calculated and Figure 4-5 and 4-6 report representative results obtained from the solid methane hydrate simulation and the liquid phase methane/ water simulation respectively. Specifically, these figures characterize the structural relationship between the methane guest's center and the water oxygen atom. Analagous quantities for the ethylene oxide hydrate and ethylene oxide/ water system are reported in Figures 4-7 and 4-8.

Calculated spectra are presented and discussed in Chapter 5.

Table 4-3. Molecular polarizabilities in e.s.u.

Water	**Value**	**Reference**
α_{xx}	1.468×10^{-24}	59
α_{yy}	1.528×10^{-24}	
α_{zz}	1.415×10^{-24}	
$^0\mu$	1.855×10^{-18}	62
$\bar{\beta}$	3.130×10^{-31}	63
$A_{123,1}$	1.164×10^{-36}	64
$A_{123,3}$	-0.36×10^{-32}	
Methane		
α_0	2.593×10^{-24}	65
$^0\mu$	0	
Ethylene Oxide		
α_{xx}		66
α_{yy}		
α_{zz}		
$^0\mu$	1.88×10^{-18}	67

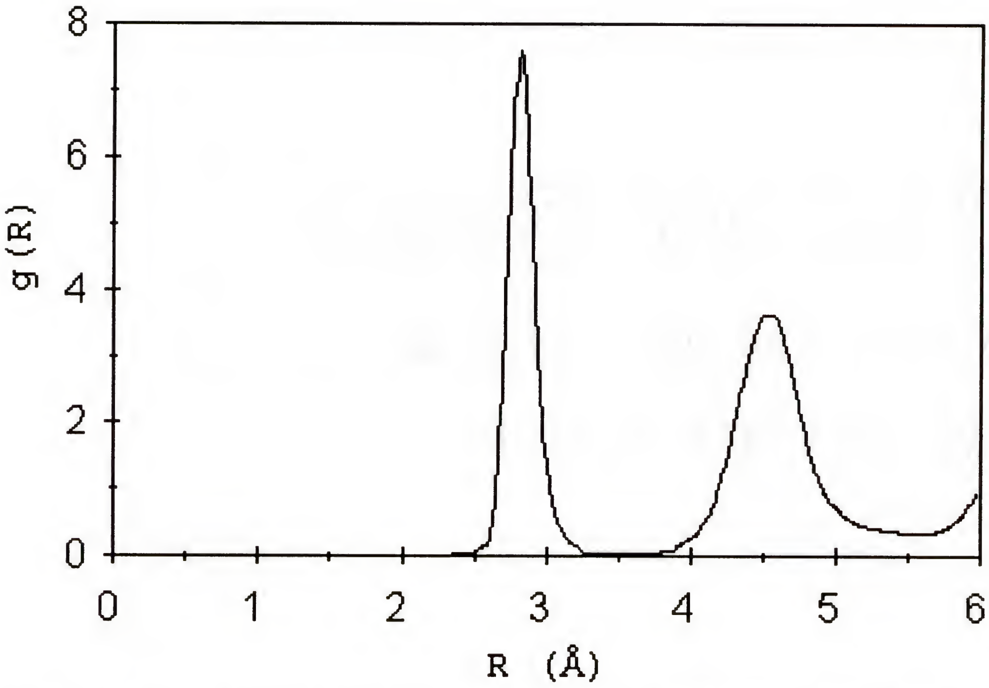

Figure 4-1. $g_{OO}(R)$ calculated from methane hydrate simulation, T = 145 K.

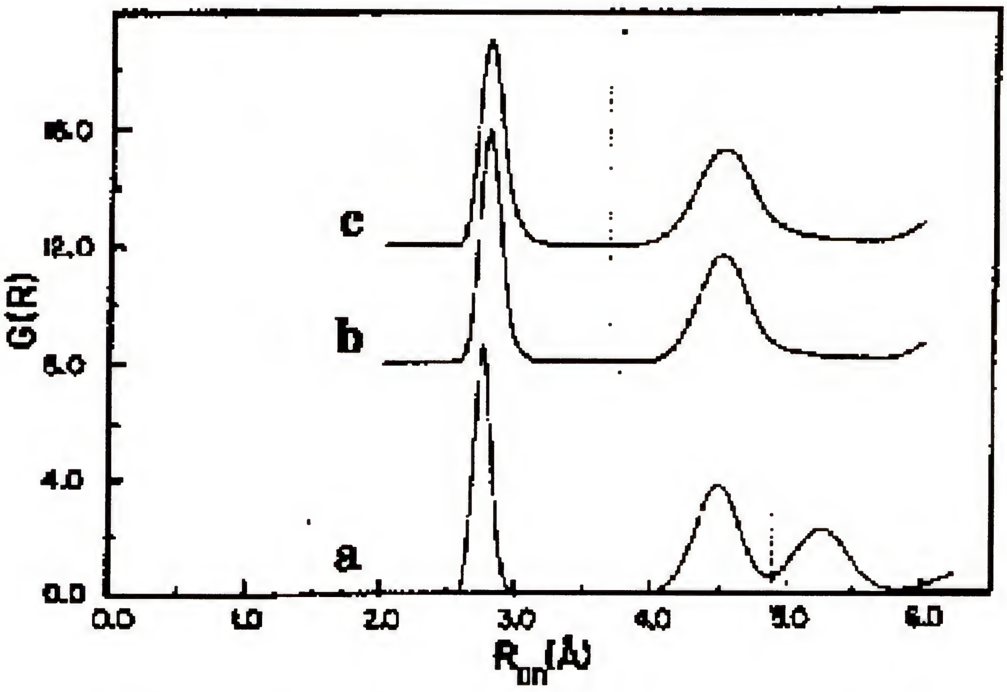

Figure 4-2. $g_{OO}(R)$ calculated from simulations by Tse et al. (a) ice Ic at 69 K, (b) empty hydrate at 110 K, and (c) methane hydrate at 145 K.

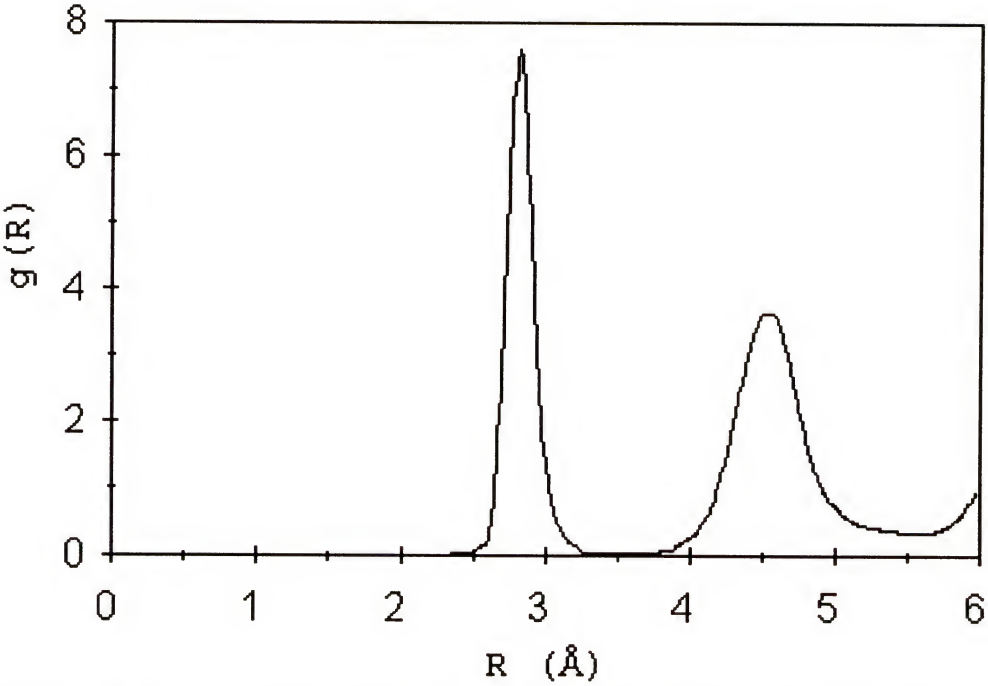

Figure 4-3. $g_{OH}(R)$ calculated from methane hydrate simulation.

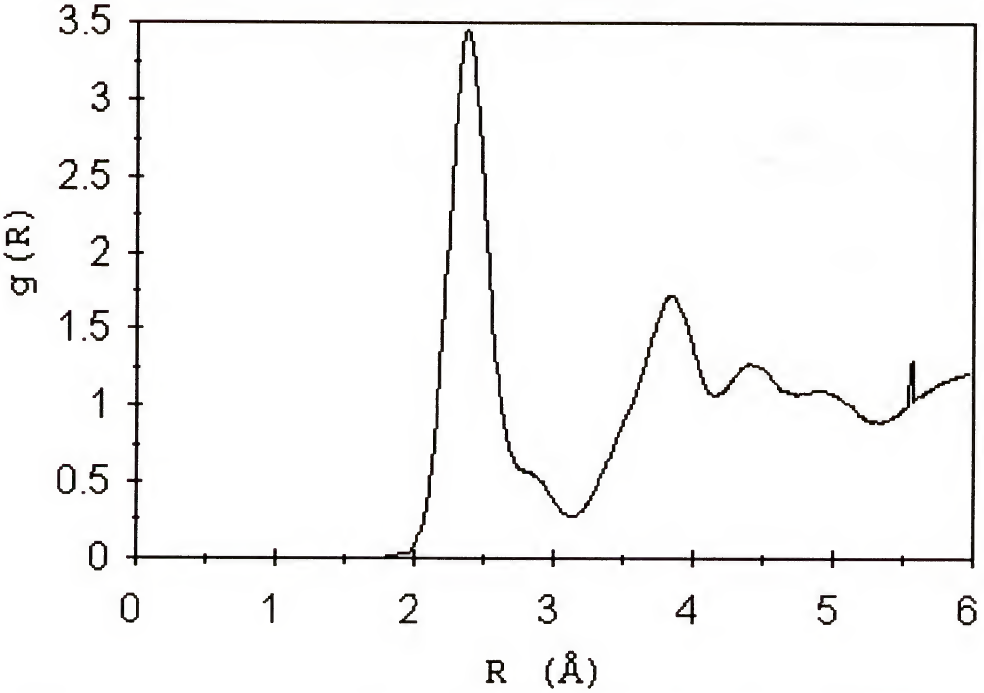

Figure 4-4. $g_{HH}(R)$ calculated from methane hydrate simulation.

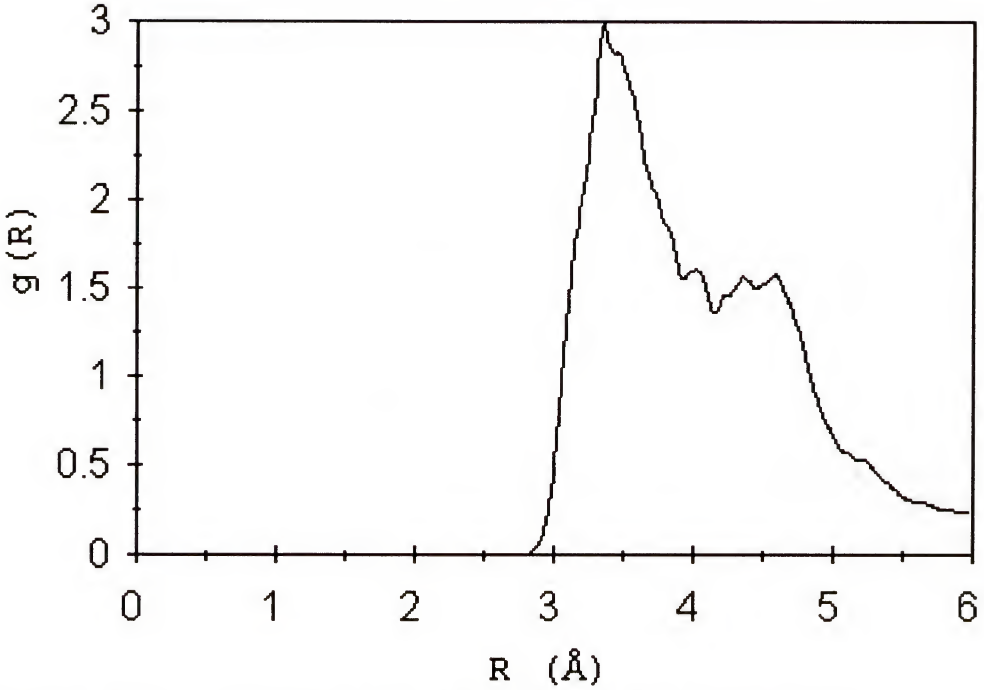

Figure 4-5. Guest-host atom-atom distribution function, $O[(CH_2)_2O]$ -- $O(H_2O)$, calculated from the ethylene oxide hydrate simulation

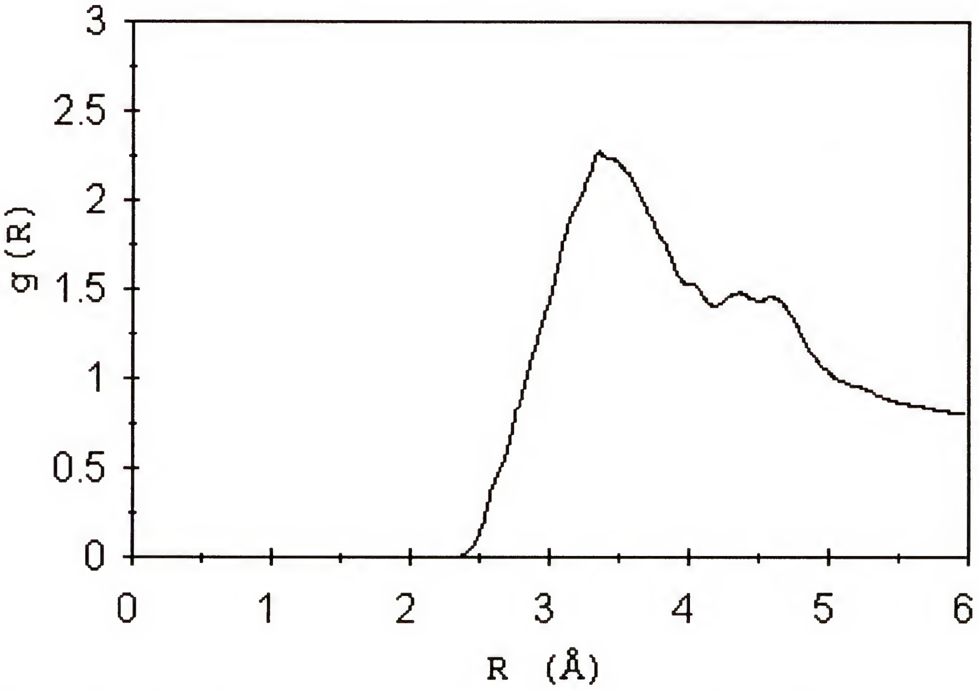

Figure 4-6. Guest-host atom-atom distribution function, $O[(CH_2)_2O]$ -- $O(H_2O)$, calculated from the ethylene oxide/ water simulation

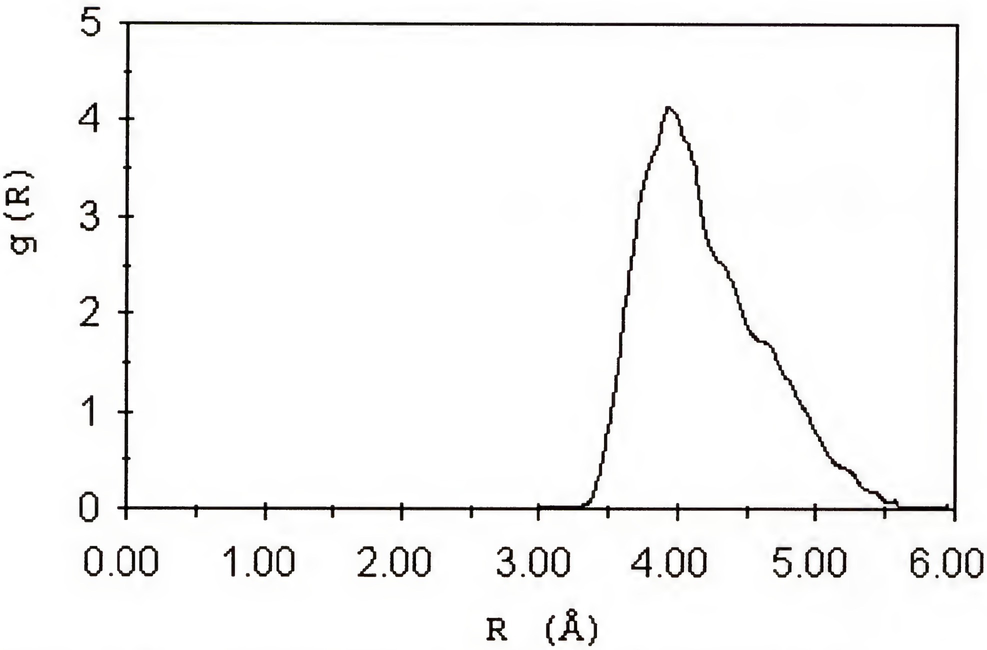

Figure 4-7. Guest-host atom-atom distribution function, C(CH_4) -- O(H_2O), calculated from the methane hydrate simulation

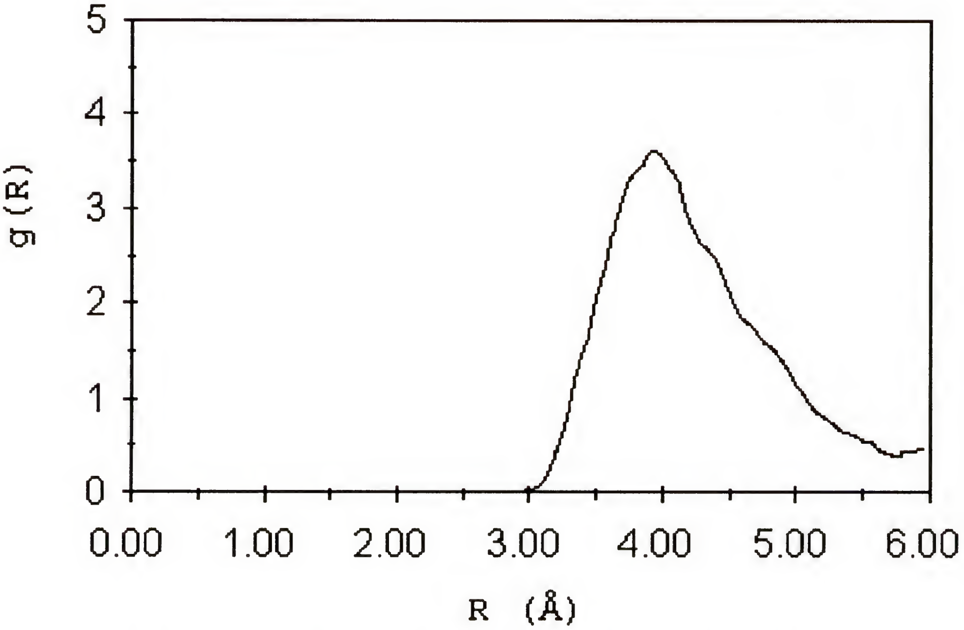

Figure 4-8. Guest-host atom-atom distribution function, C(CH_4) -- O(H_2O), calculated from the ethylene oxide/ water simulation

CHAPTER 5
ANALYSIS AND DISCUSSION

The High Wavenumber Shift Region

Fitting Procedures

All spectra were smoothed once with a Savitsky-Golay three-point smoothing function before analysis. Fitting of spectra was performed using software entitled "RAMAN."[68] The The code fits combinations of Lorentzian and Gaussian peaks to Raman spectra with a polynomial background using the Levenberg-Marquardt method. Figure 5-1 indicates the results of using this procedure on a representative spectral region.

Spectral Features due to THF

Tetrahydrofuran contains several vibrational modes which contribute to infrared or Raman spectra, or to both, and the assignments made by Palm, et al[69], are collected in Table 5-1. One would expect attractive intermolecular interactions between THF and water to occur primarily between either of the hydrogen atoms on water and the oxygen atom on THF. Indeed, those spectral features which derive from THF vibrational

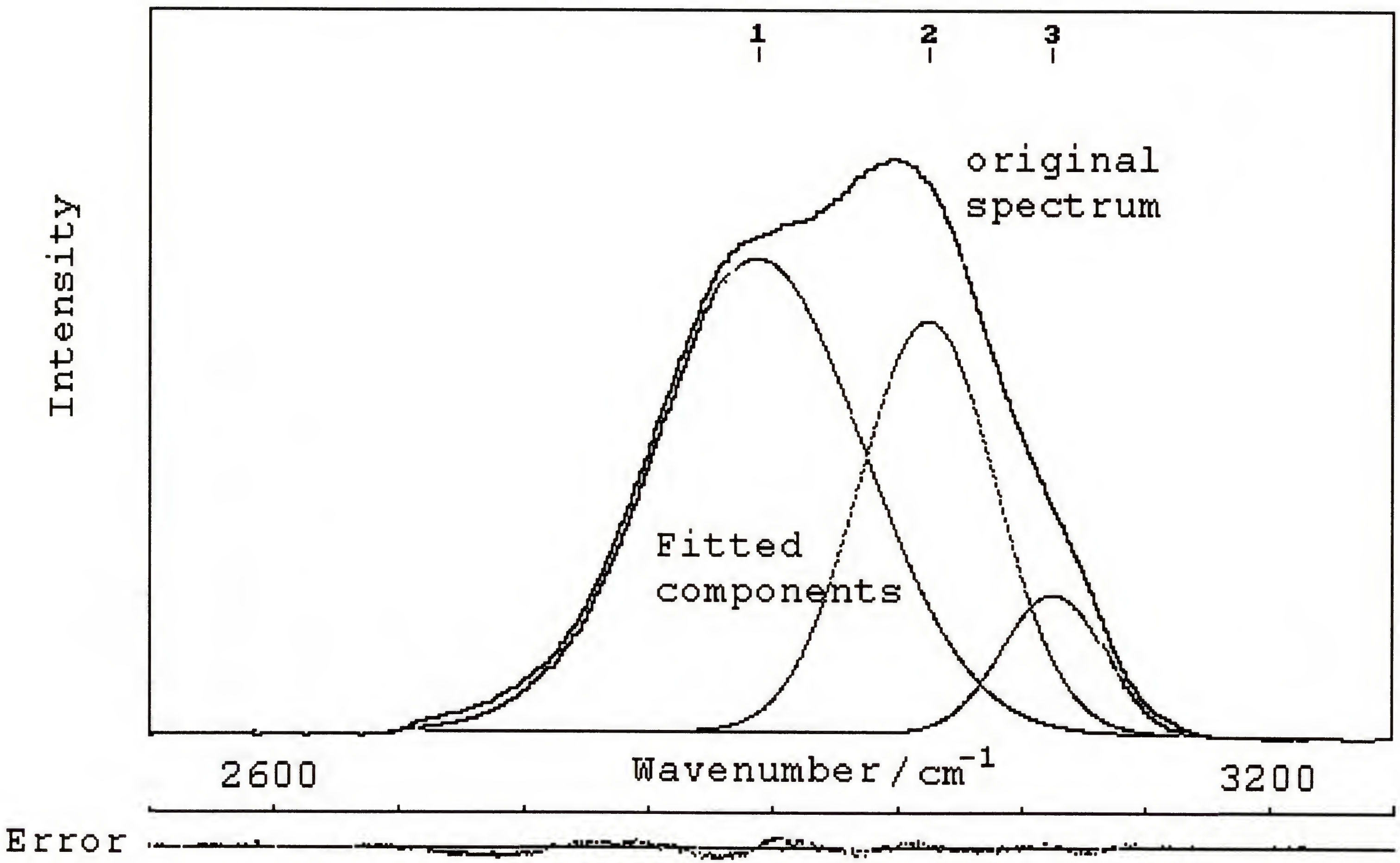

Figure 5-1. Typical results fitting an experimental spectrum (total Raman scattering from $H_2O(l)$ at 25 °C).

Table 5-1. Raman and Infrared Spectral Data and Assignments[69].

Raman cm^{-1}	**Infrared cm^{-1}**	**Assignments**
2975	2977 vs	CH stretch
2938		CH stretch
2865	2861 vs	CH stretch
2717	2860 m	CH stretch
	1972 m	CH stretch
1486		CH_2 bend
1452	1461 s	CH_2 bend
	1364 m	CH_2 wag
	1333 m	CH_2 wag
	1289 m	CH_2 wag
1234	1234 m	CH_2 wag
1174	1177 s	ring stretch
1104		CH_2 twist
1071	1067 vs	ring stretch
964		CH_2 rock
913	908 vs	ring stretch
651	654 s	CH_2 rock
596		ring i-p bend
276		ring o-p bend
215		ring o-p bend

modes primarily involving its aliphatic portions are essentially insensitive to the variations in temperature and composition that are reported here. In contrast, vibrational motions of the THF molecule which involve the stretching of C-O-C bonds give rise to spectral features that are quite sensitive to changes in the system.

Specifically, the peak which occurs at 913 cm^{-1} in the pure liquid THF spectrum at 25 °C can be attributed to ring stretching modes, denoted COC stretch in this discussion. With the addition of water a shoulder appears on the low wavenumber side of the COC stretch peak. These two features are particularly important.

Figure 5-2 illustrates the effect of system composition on the position of these peaks: the dilution of THF with water shifts the shoulder to significantly lower wavenumbers. A similar trend, but with smaller magnitudes, is found when the weaker hydrogen bonding solvents methanol and chloroform are used.

Changes in system composition also alter the ratio of integrated intensities for these two THF peaks as is illustrated in Figure 5-3. The effect of temperature on peak position is much weaker as can be seen in Figure 5-4. Similarly, the effect of temperature on the ratio of integrated intensities is given in Figure 5-5.

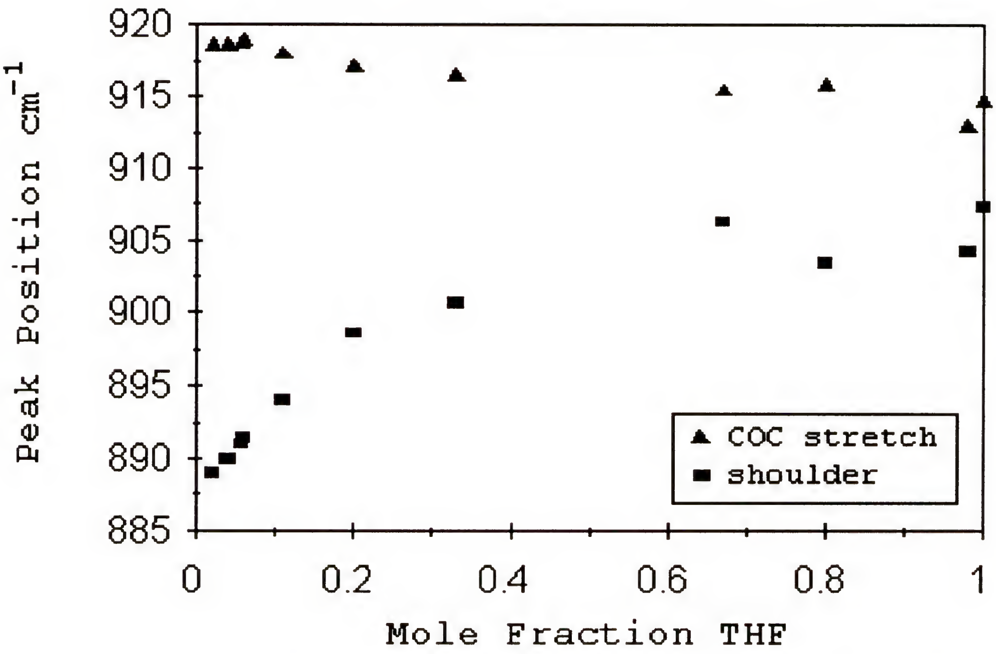

Figure 5-2. Composition dependence of COC/Shoulder peak positions

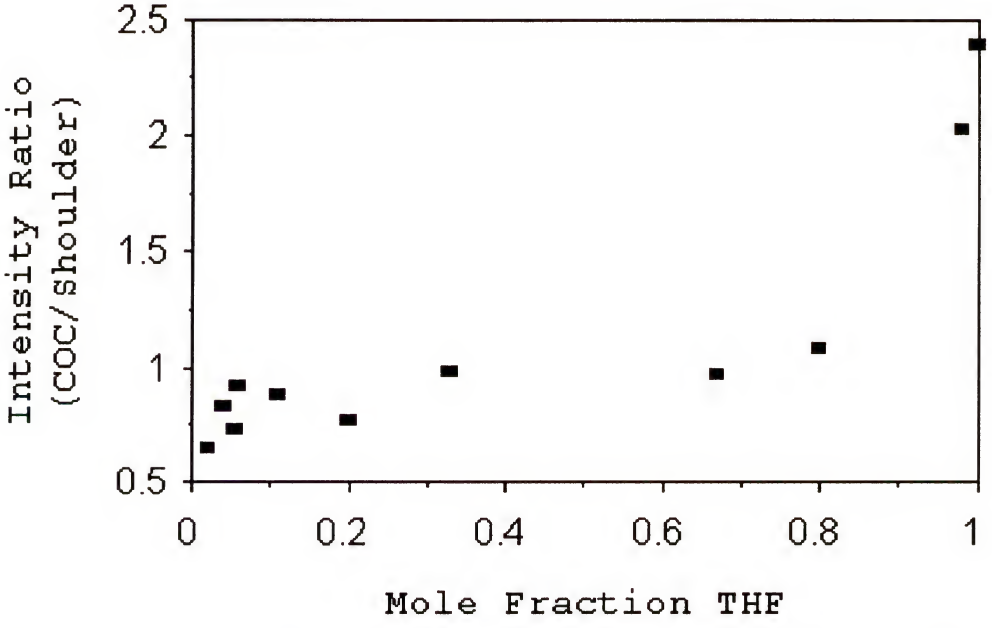

Figure 5-3. Composition dependence of COC/Shoulder Intensity ratio.

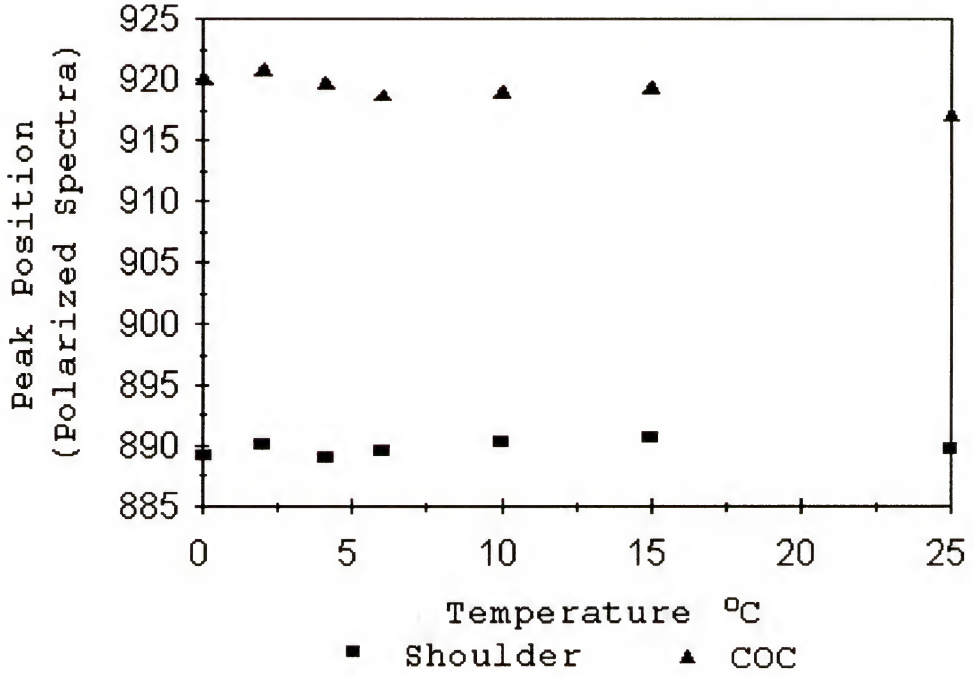

Figure 5-4. Temperature dependence of COC and Shoulder peak positions (0.056 mole fraction THF).

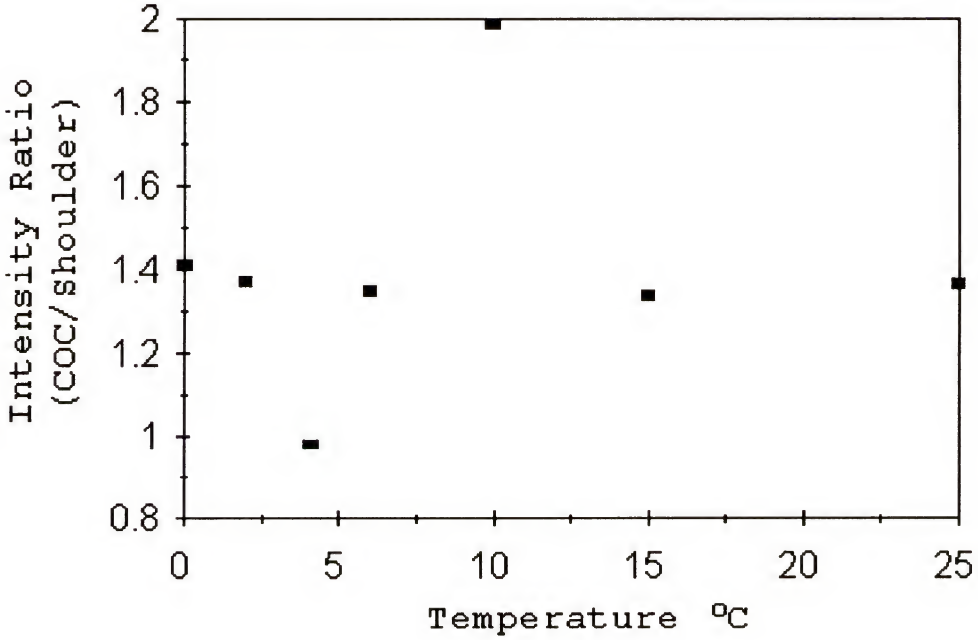

Figure 5-5. Temperature dependence of integrated intensity ratio (0.056 mole fraction THF).

If vibrational and rotational motion are uncorrelated, one can determine the rotational correlation time by comparing the widths of a particular peak in the isotropic and depolarized spectrum. That is, one can calculate,

$$\tau_{rot}^{-1} = 2\pi c(W_{depol} - W_{iso}) \qquad [5\text{-}1]$$

where W refers to the full-width at half-maximum (FWHM) for the specified spectrum[70]. Calculations of this type were performed for the THF COC stretch peak and the results are presented in Table 5-2 from which it is readily apparent that the assumption of vibrational-rotational statistical independence is not justified.

Table 5-2. THF rotational relaxation times calculated from depolarization ratio of COC peak.

T /K	**τ_{THF} /ps**
298	3.27
293	2.86
291	2.44
288	3.02
283	4.21
281	4.80
279	5.08
278	4.77
277	5.68

Spectral Features due to Water

The high wavenumber spectrum of liquid water contains features due to the three normal vibrational modes of the monomer, all of which are strongly modified by the influence of intermolecular interactions.

The intense and broad band from 2800 cm^{-1} to 3800 cm^{-1} is due to intramolecular OH vibrations. These vibrations are extremely sensitive to the presence and nature of local hydrogen bonding and thus contain information concerning the intermolecular structure of the liquid phase.

The complexity of liquid water has given rise to two distinct classes of models. Continuum models assume that all water molecules are four-coordinated as in ice, but with a continuous distribution of hydrogen bond strengths and configurations[71].

Mixture models postulate the existence of a small number (nine or fewer) of species (e.g., dimers, trimers, pentamers) that differ in the number and configuration of hydrogen bonds. The spectra of the liquid are usually separated into components which are then attributed to different species. However, the number of species involved is an unknown parameter which leads to controversial multi-peak band fitting. Nevertheless, this is the approach that has consistently garnered experimental support.

The analysis of the OH stretching region that is offered here closely follows that described by Walrafen[72] and belongs in the class of mixture models.

In the analysis offered by Walrafen, the OH stretching region is decomposed into components classified according to whether they lie above or below an isobestic point at 3425 cm^{-1}. Those lying above this point are attributed to hydrogen bonded molecules while those below are assigned to molecules not hydrogen bonded. The integrated intensities may then be used to infer the relative number of molecules which are hydrogen bonded to other water molecules compared to those that are not.

Following Walrafen, the OH stretch region of the spectra was first corrected using the Bose-Einstein thermal population factor; it was then decomposed into three Gaussian components. Figure 5-1 indicates the results of such a decomposition. Components centered at positions higher than 3425 cm^{-1} were assigned to hydrogen bonded monomers and their integrated intensities combined to form the numerator of a ratio denoted f. The combined integrated intensities of components centered below 3245 cm^{-1} form the denominator of f. This ratio is interpreted as the mole fraction of partially covalent hydrogen bonded monomers. In Figure 5-7 these results are plotted as a function of temperature where they are compared to those obtained by Walrafen.

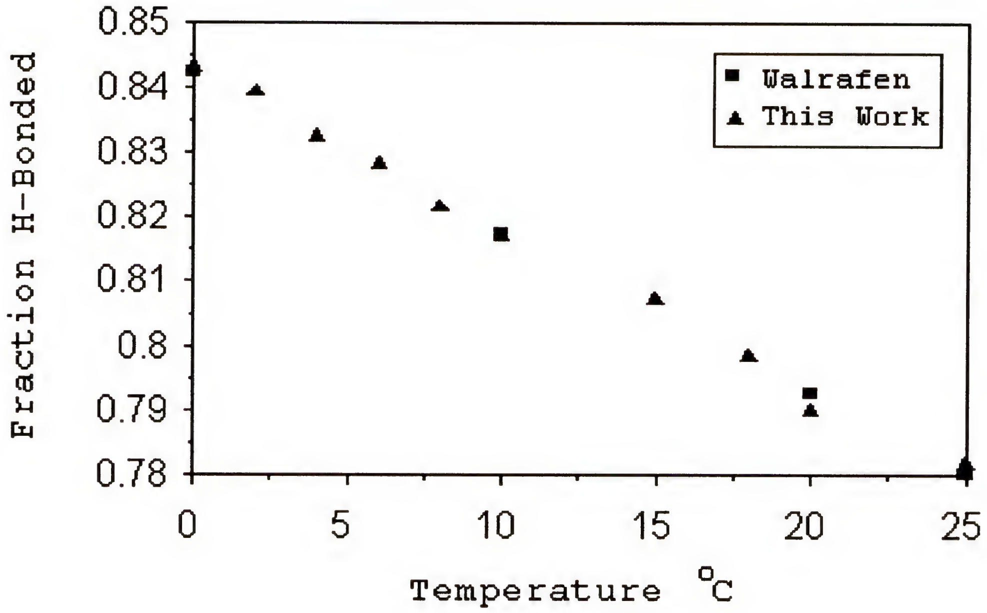

Figure 5-6. Temperature dependence of hydrogen bonding in liquid water compared to the results obtained by Walrafen

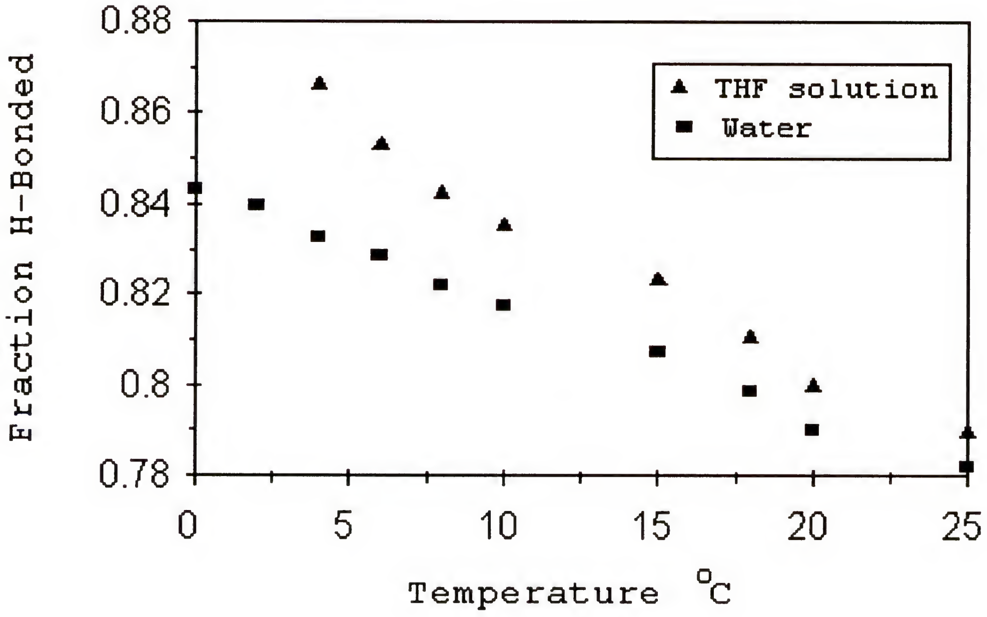

Figure 5-7. Temperature dependence of hydrogen bonding in water compared to THF solution

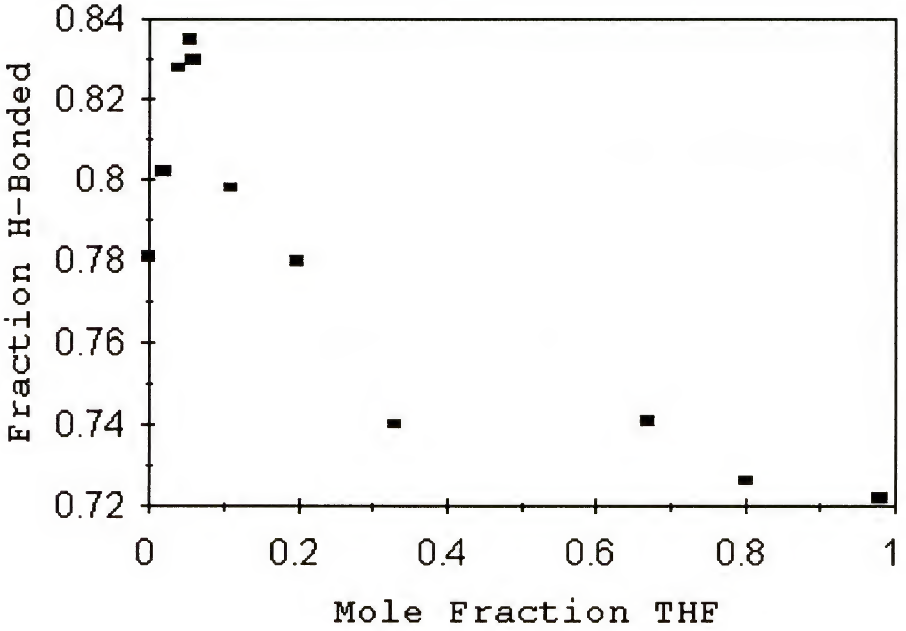

Figure 5-8. Composition dependence of hydrogen bonding at 25 °C.

Aqueous solutions of THF contain additional spectral features that arise from CH stretching modes and which appear in this same waveumber region; thus, two additional Gaussian peaks must be included in the fitting procedure.

The Low Wavenumber Shift Region

The Raman spectra results begin with those for the simulations of clusters. Figure 5-10 reports the total Raman spectra as a function of cluster size, where they are plotted in the reduced form,

$$R(\omega) = (\omega_0 - \omega)^{-4}\, \omega\{1 - \exp[-h\omega/2\pi kT]\}\, I^{st}(\omega) \qquad [2\text{-}60]$$

Figure 5-11 reports the variation of Raman spectra for the pentamer as a function of temperature.

The spectra of the clusters demonstrate how these Raman signals converge, as a function of size, to that of the bulk. As one might expect, the dimer is the main exception in the series, where the lowest- and highest-frequency peaks are redshifted relative to the pentamer spectrum. This is in contrast to the overall trend for redshifting of these peaks with increasing size. This behavior may be the result of the two molecules in the dimer having a larger range of rotational mobility.

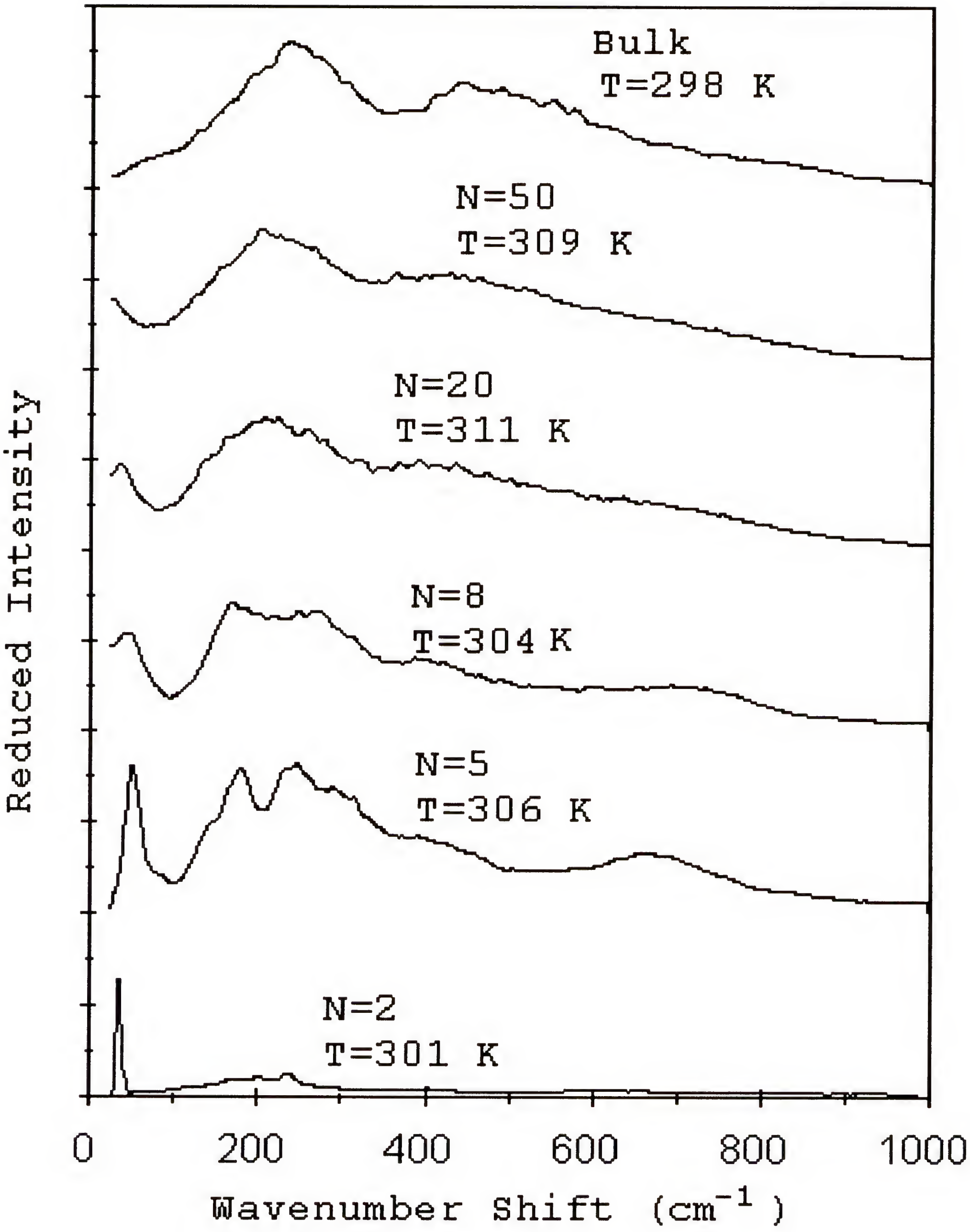

Figure 5-9. Reduced Raman spectra calculated for clusters of various sizes.

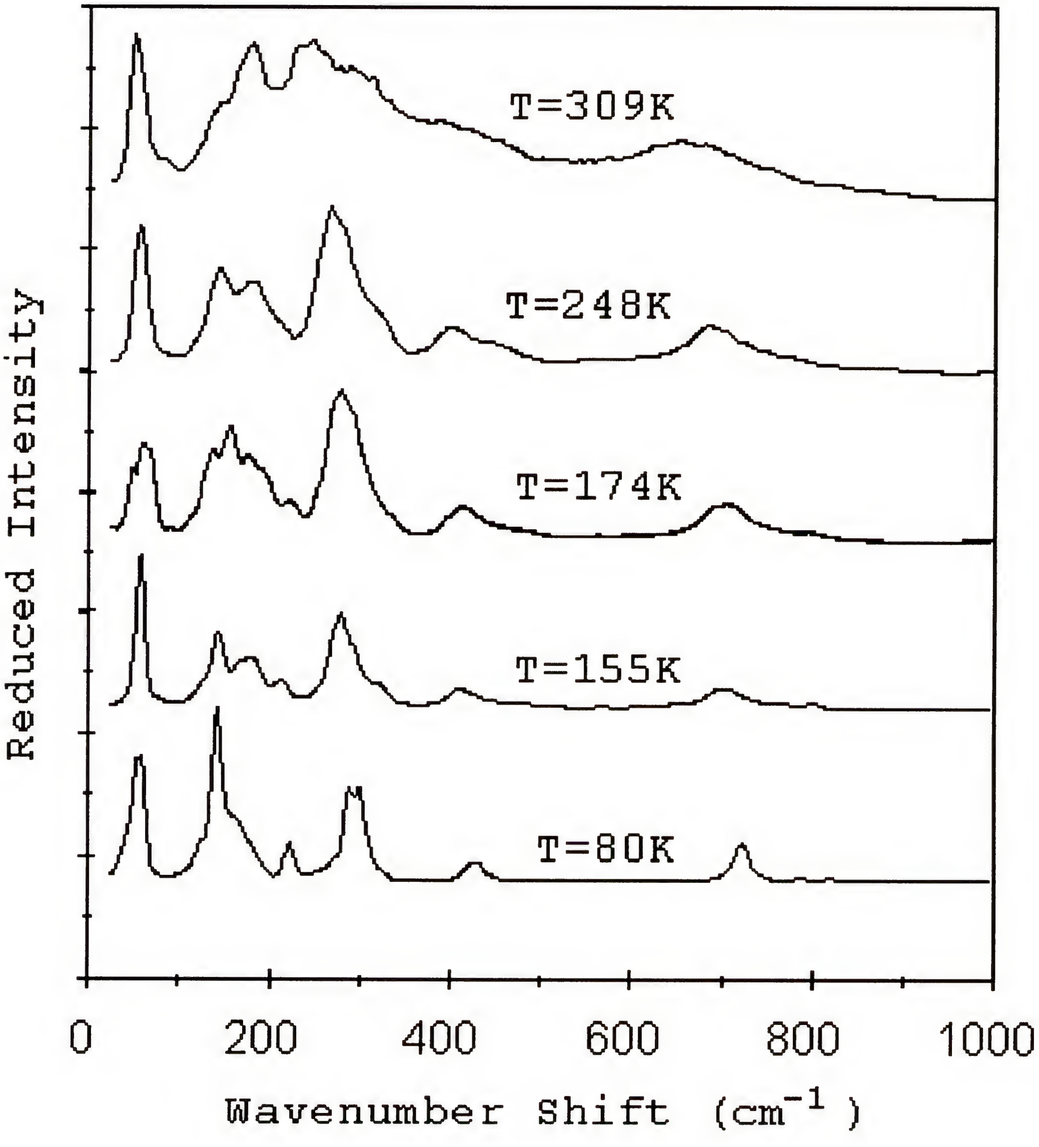

Figure 5-10. Reduced Raman spectra calculated fron water pentamer simulations at various temperatures.

It is doubtful that the peak which appears at 45 cm^{-1} in the pentamer has the same origin as the 60 cm^{-1} peak in the bulk since the former redshifts, as a function of size from 45 cm^{-1} in the pentamer spectrum to 25 cm^{-1} in the simulation of 50 molecules. As size is increased, the peaks which are near 45 cm^{-1} and 700 cm^{-1} in the pentamer either diminish or broaden, and shift to the red. The 700 cm^{-1} peak is not clearly resolved in the larger clusters. The 200 cm^{-1} peak has a distinct bimodal structure in the smaller clusters suggesting that more than one type of motion may be contributing to this feature.

There are several features of note in the spectra of the pentamer simulations, presented as a function of temperature in Figure 5-11. The peak near 45 cm^{-1} has a distinct bimodal character at lower temperatures. The peak broadens only slightly as the temperature increases and it shifts to the red only a few wavenumbers.

The peak near 140 cm^{-1} broadens considerably with temperature increase. A shoulder on its high frequency side (150-170 cm^{-1}) increases in intensity with temperature increase, surpassing the 140 cm^{-1} peak near room temperature.

The librational features can be seen to undergo significant redshifts as the temperature increases. This can be understood in that the molecules have more energy to move at the higher temperatures, and consequently have larger amplitude librational motions with lower characteristic oscillation frequencies.

Raman spectra for the bulk water simulations are decomposed into their components and left in their unreduced form begining with Figure 5-12 which contains the allowed rotational spectra, reported as a function of temperature. These show the characteristic lineshapes of the orientational contributions of asymmetric tops, specifically, an intense Q-branch plus a broad band extending past 700 cm^{-1}. They also show a well-defined band arround 480 cm^{-1} in the supercooled liquid. With an increase in temperature this band is red-shifted until it merges into the Q-branch.

From Figure 5-13 it can be seen that the allowed portion of the depolarized spectrum is dwarfed by the IDID contribution which is at least an order of magnitude larger. Since α_0 is a scalar, the dynamical information appears in the IDID spectrum through the dipole propagator and the spectra reflect only the center of mass translational dynamics. In simple fluids the lineshapes are approximately exponential, while water spectra develop more structured profiles containing features which are probably related to those observed in inelastic neutron experiments and in the power spectrum of the center of mass velocity.

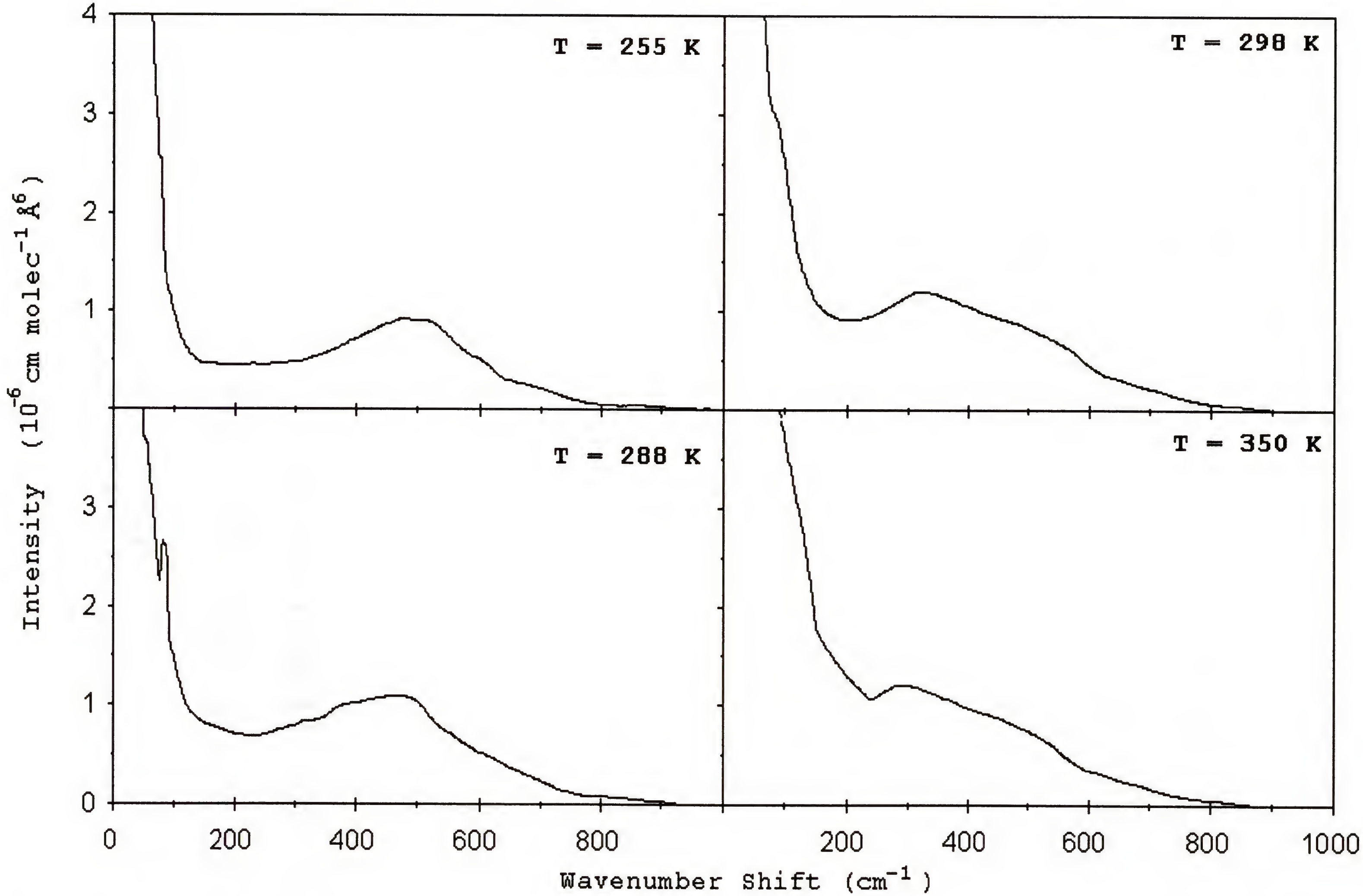

Figure 5-11. The allowed rotational spectrum calculated from bulk water simulations at various temperatures.

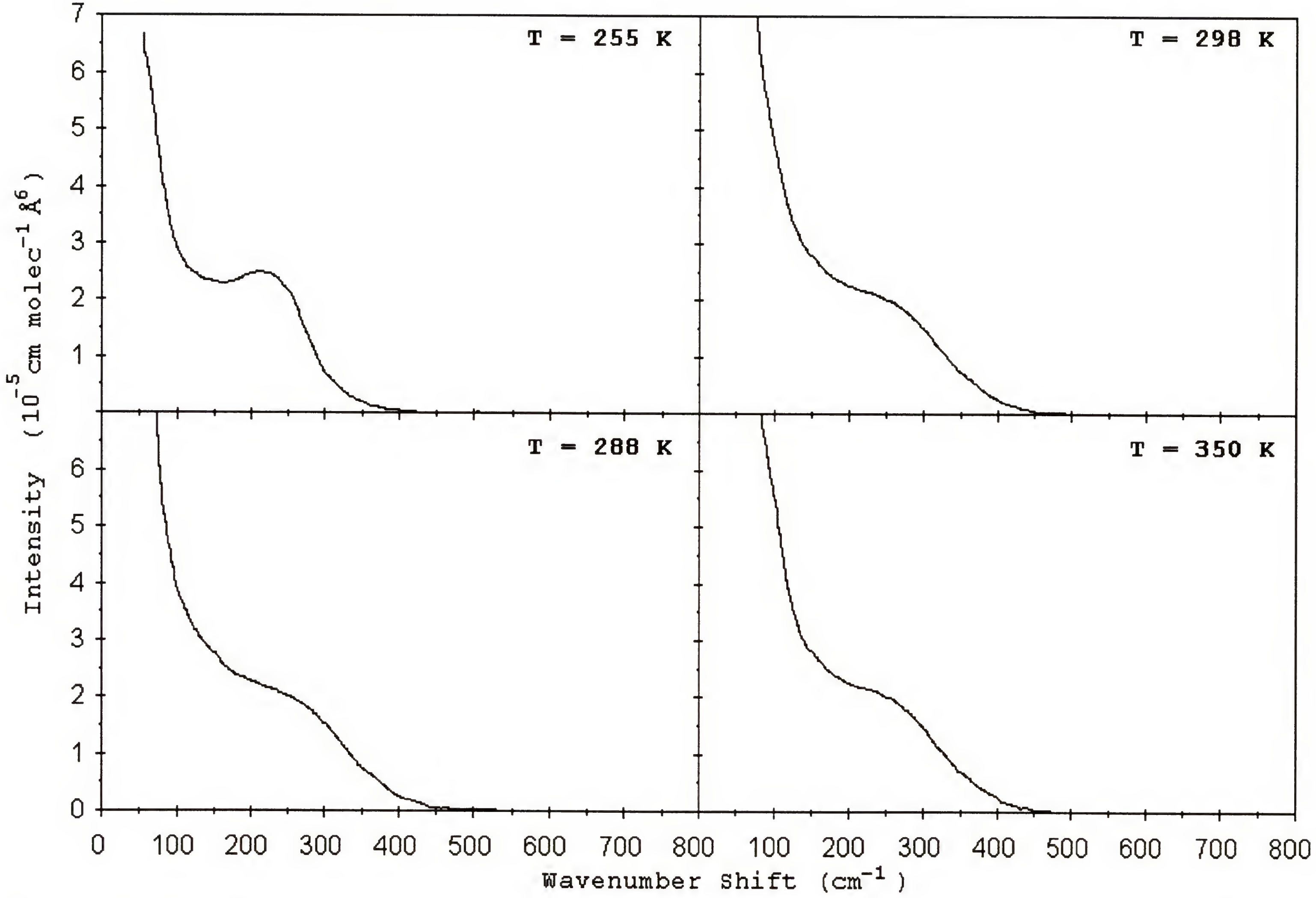

Figure 5-12. The calculated IDID spectrum for bulk water simulations at various temperatures.

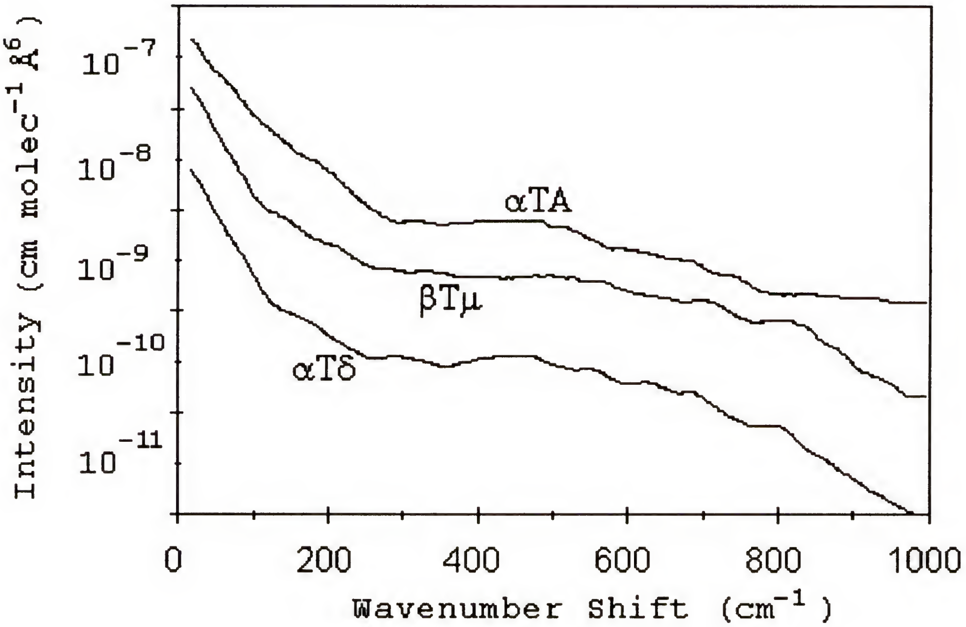

Figure 5-13. Higher order contributions to the isotropic spectrum calculated for the 288 K bulk watersimulation.

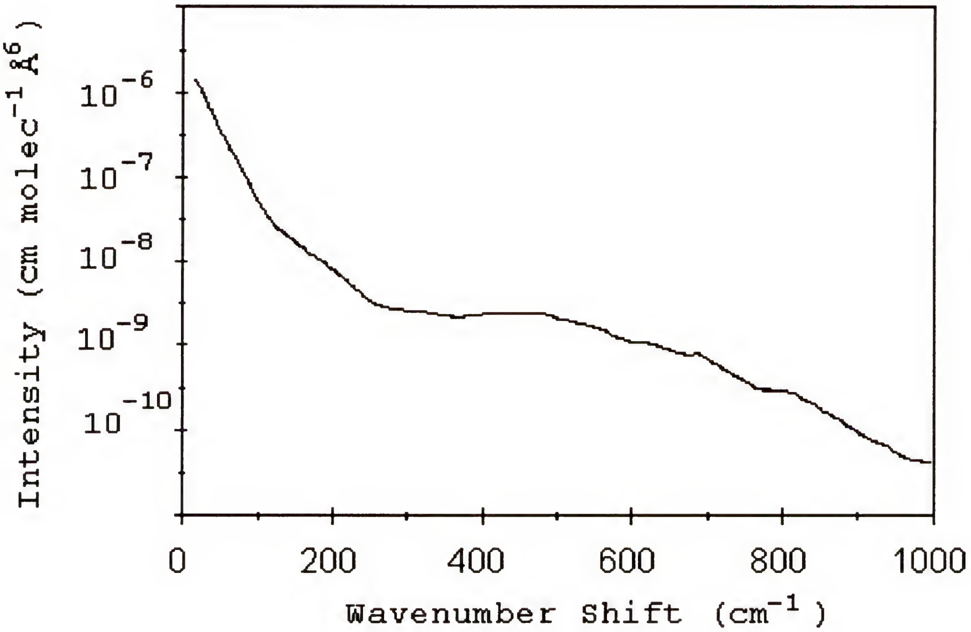

Figure 5-14. The total isotropic spectrum calculated from the 288 K bulk water simulation.

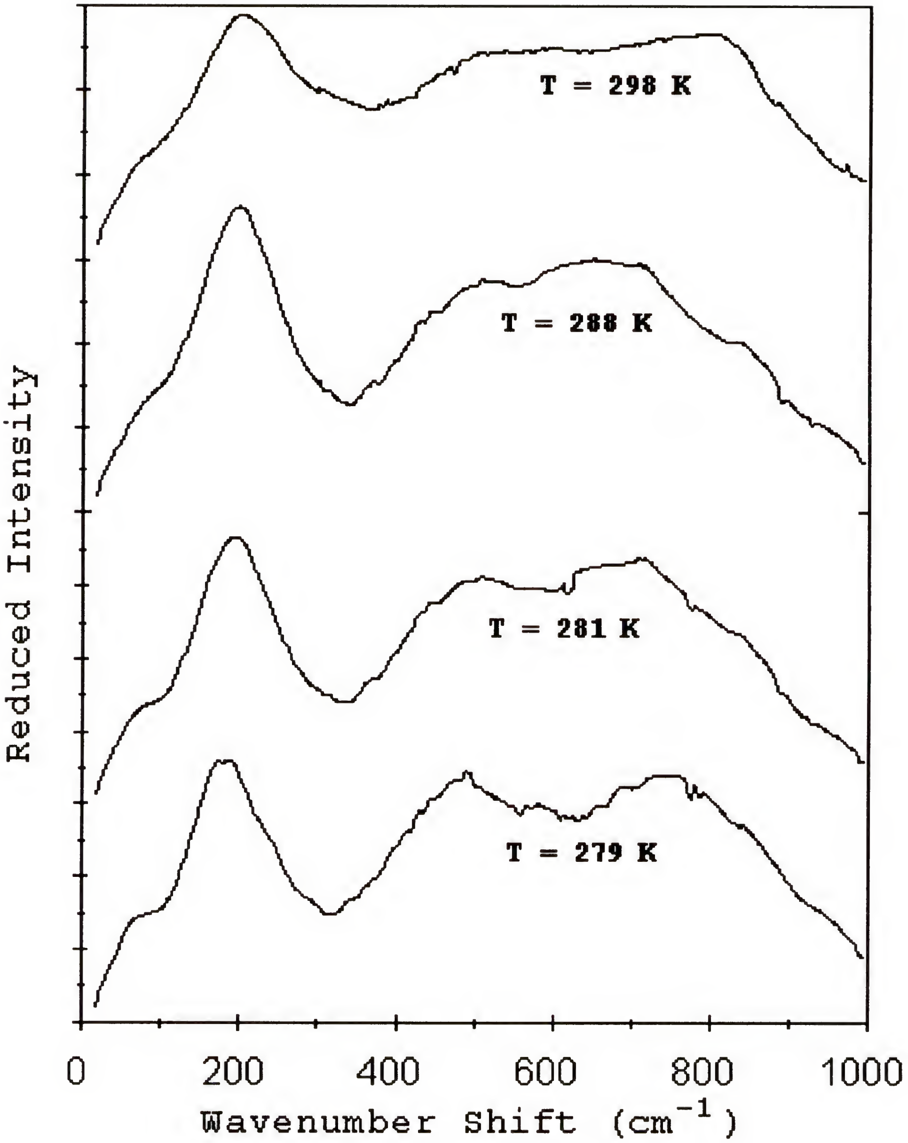

Figure 5-15. Representative depolarized experimental water spectra.

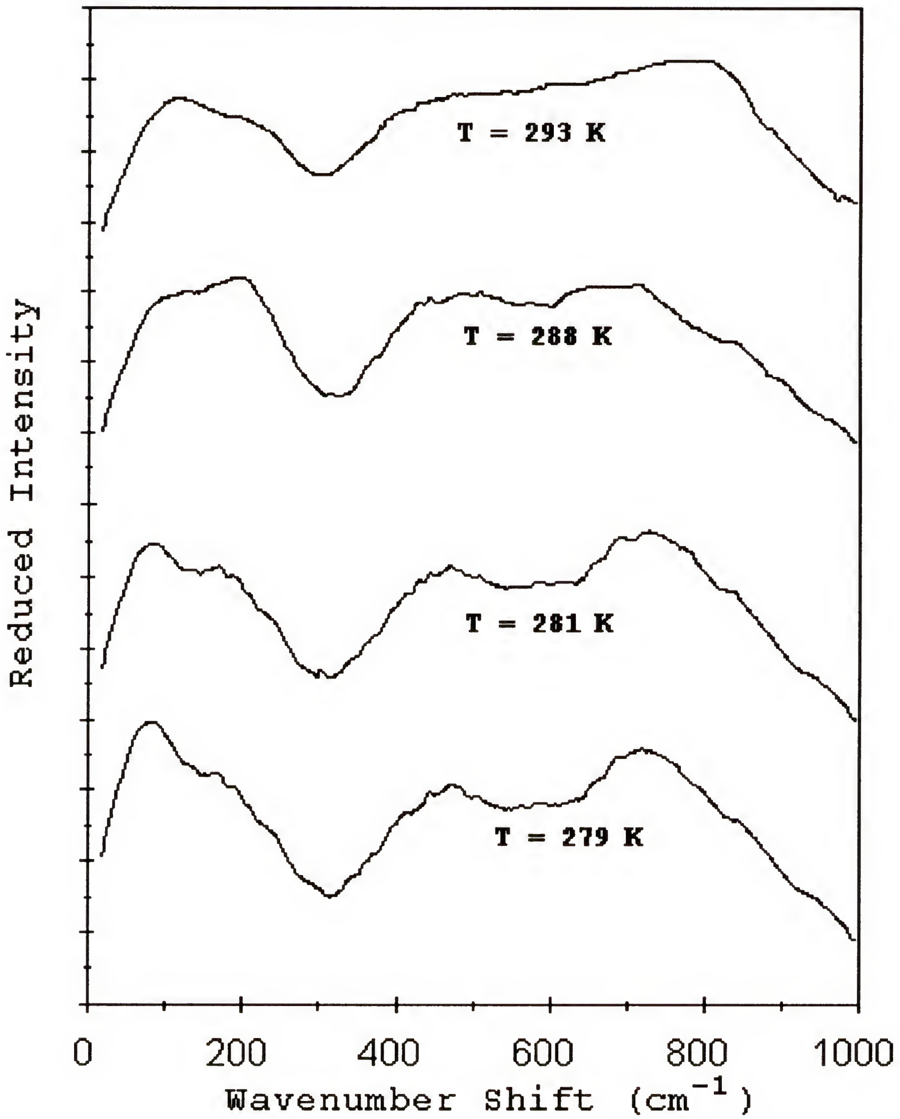

Figure 5-16. Representative depolarized spectra obtained from THF/ water solutions (0.056 mole fraction THF).

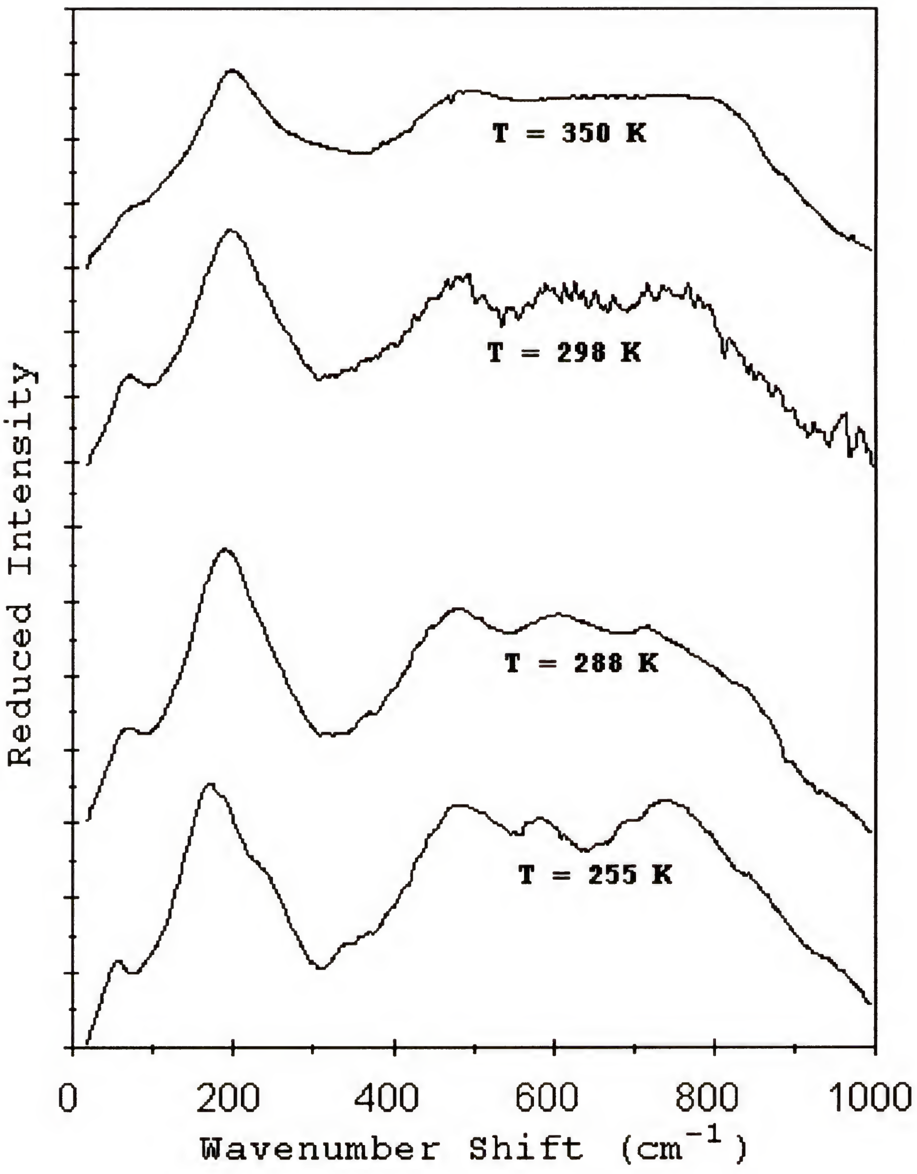

Figure 5-17. Depolarized spectra calculated from bulk water simulations.

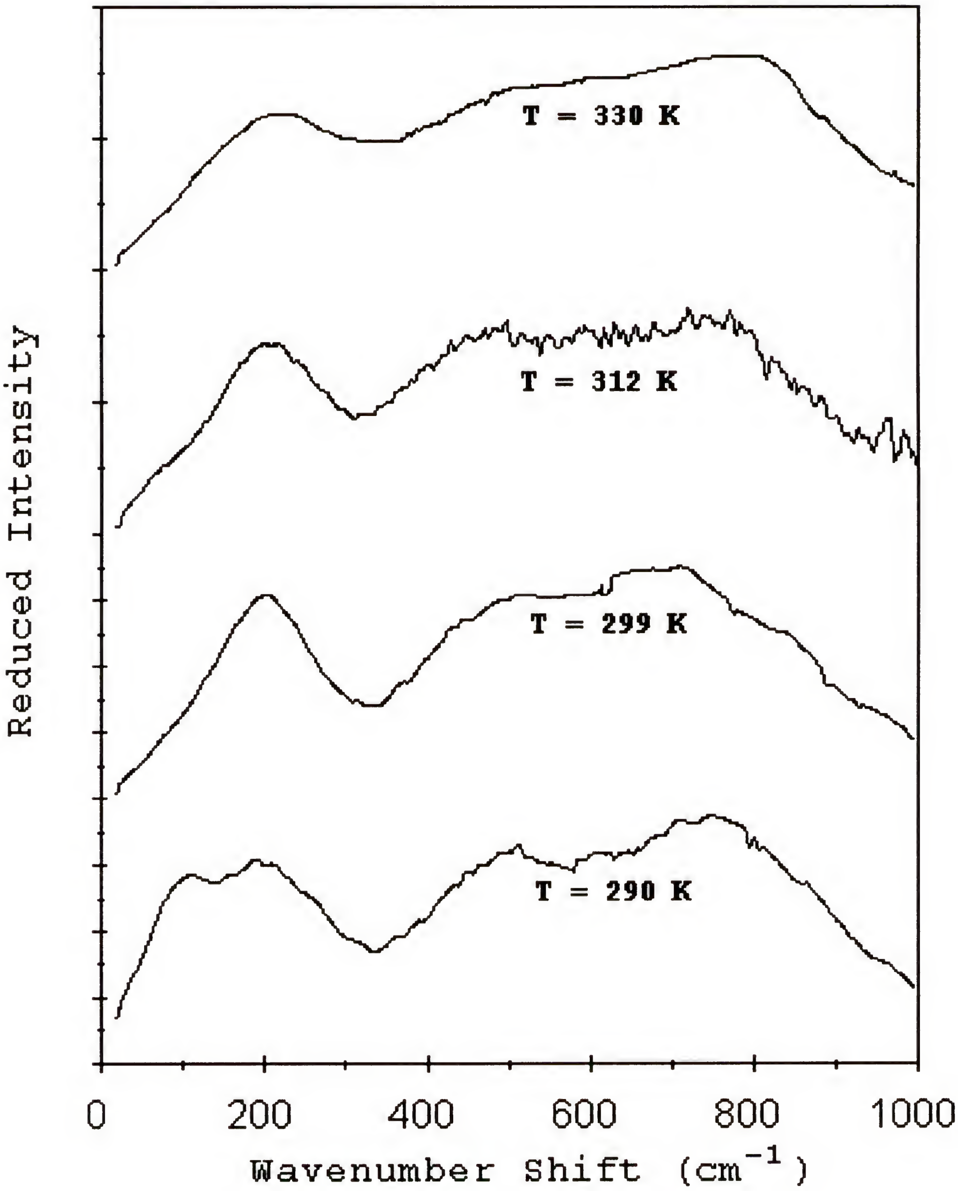

Figure 5-18. Depolarized spectra calculated from ethylene oxide/water simulations.

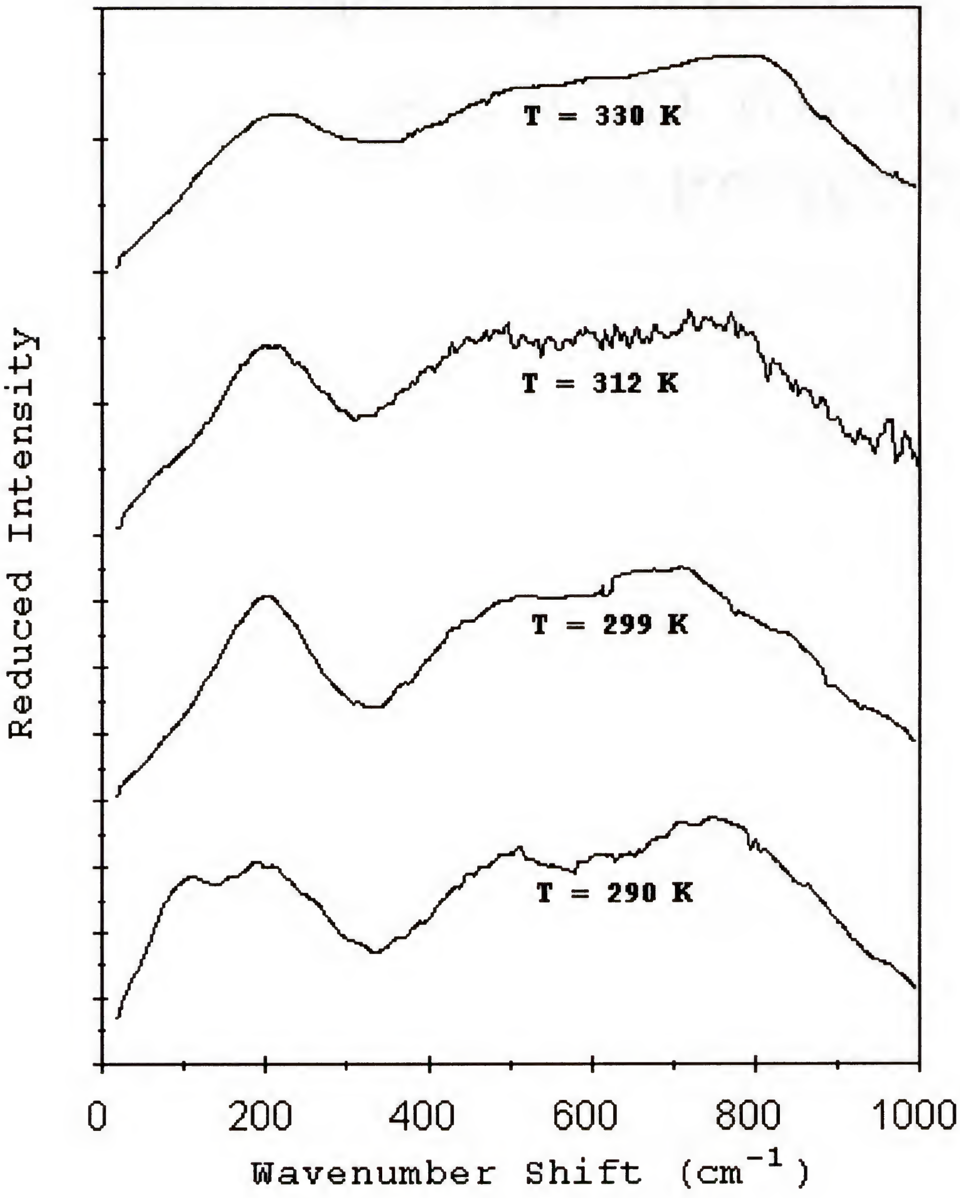

Figure 5-19. Depolarized spectra calculated from ethylene oxide/water simulations.

Higher order contributions to the light scattering spectra are plotted for the 288 K MD simulation in Figure 5-14. Though these are calculated from different tensors, all of them show an approximately exponential decay to 200 cm^{-1} with a characteristic frequency of about 80 cm^{-1}. This is followed by a broad tail which extends to about 900 cm^{-1}.

The sum of these three higher order contributions is plotted in Figure 5-15 as the total isotropic spectrum. Its lineshape appears to be independent of temperature. Like their experimental counterparts, the calculated isotropic spectra are essentially featureless. The calculated spectra suffer an additional handicap: their dependence on the poorly known dipole-quadrupole polarizability, $\mathbf{A}$. This quantity is known for only a handful of molecules, and no experimental values for the dipole-quadrupole polarizability could be found for either methane or ethylene oxide; calculated values range over nearly two orders of magnitude. Since the αTA terms are of the same order as the other higher-order contributions, their neglect would lead to unreliable isotropic spectra; hence the remainder of this discussion will concern only the depolarized spectra.

Both the experimental and simulated low wavenumber depolarized spectra for bulk water are consistent with the results obtained by others. Specifically, they contain maxima located at nearly the same positions, and show the correct temperature dependence.

Decomposition of the room temperature experimental reduced depolarized spectrum into Gaussian components gives components centered at approximately 65 cm^{-1} and 190 cm^{-1}, assigned to restricted translational modes of motion, and very broad components centered near 470, 550, and 770 cm^{-1}, which are assigned to librational motion. The simulated room temperature spectrum yields nearly identical results: 65, 195, 477, 609, and 752 cm^{-1}. These compare favorably to the experimental Raman results reported by Walrafen[73]: 60, 170, 470, 550, 775 cm^{-1}. In the spectrum of water far-infrared absorption coefficients[74], broad bands were found at 60, and 188 cm^{-1} with an unresolved librational maximum at approximately 685 cm^{-1}. Similar results have been obtained in calculations of the vibrational density of states derived from inelastic neutron scattering[75].

As Figure 5-17 makes clear, the addition of THF produces rather large effects, both in the position and intensity of the maxima, particularly in the restricted translation region.

Figure 5-18 contains the reduced depolarized spectra obtained from bulk water simulations. An effect similar to that produced by the addition of THF in the experimental spectra also appears in the spectra calculated from the simulations. the ethylene oxide/ water system, given in Figure

5-19. This is followed by the simulated methane/ water system spectra given in Figure 5-20.

Compared to their high wavenumber counterparts, the low wavenumber spectra are characterized by broader and much less structured features. This makes their interpretation more difficult but some insight can be obtained from power spectra calculated from the simulated solid hydrates.

The velocity time autocorrelation function is given by,

$$C_v(t) = \frac{\langle \mathbf{v}(t) \cdot \mathbf{v}(0) \rangle}{\langle \mathbf{v}(0) \cdot \mathbf{v}(0) \rangle} \qquad [5\text{-}2]$$

and the power spectrum associated with translational motion is obtained as the Fourier transform of the velocity autocorrelation function[76]. For a monatomic harmonic crystal, the power spectrum is just the density of vibrational states. For a molecular system, one may study analogous quantities describing the translational motion of the center of mass and rotational motion of the molecule, i.e., the autocorrelation functions of the molecular velocity and angular velocity, respectively.

A good approximation of the host lattice translational density of states is given by the power spectrum of oxygen atom motions and this is presented in Figure 5-21 for the simulated ethylene oxide hydrate. Similarly, one may obtain insight into the host librational motion from Figure 5-22 which displays the power spectrum obtained from the motion of hydrogen atoms of the host lattice. Analogous spectra corresponding to motion of the guest are presented in Figure 5-17 and 5-18.

These calculations were also performed for the simulated methane hydrate. The motion of host water molecules is similar in nature in the two hydrates though, as Table 5-2 indicates, there are differences in the details. The motion of the guest molecules in the two hydrate types differs more substantially, as Figures 5-23 through 5-26 make clear.

The main features of the translational density of states for the hydrates are similar to those found in experimentally for ice Ic at a comparable temperature[77]. Even for the solid hydrate, variations in temperature lead to a significant redistribution of the density of states. Specifically, an increase in temperature leads to a very large enhancement in the density of states in the 100-300 cm^{-1} region of the spectra. Furthermore, there is a tendency for the vibrations to shift to lower temperatures. This trend has been observed in the infrared spectra of ice Ic and ice Ih[78], in the infrared and Raman spectra of liquid water[79], and in the bulk liquid simulations reported here.

An important feature of the translational spectrum is the well defined gap appearing at approximately 116 cm^{-1} and 140 cm^{-1} for the methane and ethylene oxide hydrates respectively.

This gap, though not as well defined, appears in the vibrational power spectrum, the Raman spectrum of the simulated liquid systems and in the experimental THF/ water Raman spectrum, though at significantly higher wavenumbers. These may be compared to the results of incoherent inelastic neutron scattering for the SI SO_2 hydrate[80], whose low frequency neutron time-of-flight spectrum showed two broad maxima at 69 and 244 cm^{-1}, separated by dip at 110 cm^{-1}. The large scattering cross section of the proton prevented observation of SO_2 motion.

The translational frequency spectrum of the encaged methane molecules contains well defined peaks at 35, 54, and 78 cm^{-1}. By following the motion of specific molecules, these can be partitioned into the contribution from the small cages and large cages, mean radii ~4.0 and ~4.3 Å respectively. Thus the higher energy vibration, 78 cm^{-1}, is assigned to the motion of methane molecules in the smaller, nearly spherical cages. The lower vibrational frequencies and the splitting of the translational energy of guests in the large cages may be understood as a consequence of the greater size and assymmetry of the cavity. The fact that these frequencies fall in the same range as several prominent peaks in the host translational spectra suggests that even in the solid hydrate the potential exists for coupling between the translational motion of the guest molecules and that of the host lattice.

Although there are no experimental infrared data available for methane hydrates, there are results for the xenon hydrate between 50 and 350 cm^{-1} [81]. The main features are similar to those for ice I_c, though there is a slight shift to higher energy in the hydrate, which is in general accord with the results reported here.

With respect to the librational motion of the host lattice, the calculated frequency spectrum spans the range between 450 and 1000 cm^{-1}. Proton motion can be studied experimentally by incoherent neutron scattering, and for ice I_h, the neutron time-of-flight cross section shows a broad asymmetric profile with a maximum located at 570 cm^{-1} and a total width of approximately 600 cm^{-1} [82].

In contrast to the pattern found for the host lattice, the librational modes of the guest occur at lower frequencies than the translations. The methane molecules trapped in the clathrate rotate essentially freely about all inertial axes. The librational density of states for ethylene oxide molecules is more complicated, perhaps due to strong coupling with its translational motion. Two absorption peaks located at 65.0 and 35.6 cm^{-1} have been observed in the infrared spectrum of the ethylene oxide hydrate[83], suggesting that the four peaks appearing in the librational density of states should be interpreted as a single pair which are split into doublets due to long range dipole-dipole interactions. If this is the case, then the infrared features should be compared to the mean values of 61 and 27 cm^{-1} calculated from the simulation.

A neutron inelastic scattering experiment[84] yielded three main peaks at 29, 39, and 57 cm^{-1}. Good agreement with dielectric and NMR results for the activation energy was obtained if the lowest frequency was assigned to libration of the $(CH_2)_2O$ molecule about its polar axis and the higher frequency librations to motions about the inertia axes which are perpendicular and parallel to the dipole axis, respectively.

To discuss the reorientational motion of the molecules one may calculate the time autocorrelation functions $C_l^x(t)$ of the first four Legendre polynomials (l=1, 2, 3, 4) of the angle subtended by the molecular axis corresponding to the dipole axis with respect to its position at t=0.

$$C_l^x(t) = \langle P_l[\mathbf{e}^x(t)\cdot\mathbf{e}^x(0)]\rangle \qquad [5\text{-}3]$$

In Figure 5-26 the results from the 288 K bulk water simulations are plotted in the form $[l(l+1)]^{-1} \ln C_l^x(t)$. This type of presentation has been found useful in evaluating the merits of models of molecular reorientation.

The four functions plotted in Figure 5-26 have the same basic features. Specifically, a glitch appears at times so short that they would correspond to almost free inertial motion in simple molecular fluids. This is followed by the onset of the diffusive, slowly decaying exponential regime.

Though the motion at long times may be described as diffusive, the behavior is not Debye-like since the functions, as plotted, do not coincide. The form in which the results are shown also disguises the fact that the amplitude of the glitch increases rapidly with increasing l.

In most dynamical models of liquid water, each molecule is assumed to reside as part of a relatively long-lived cage of four tetrahedrally coordinated neighbors. This is the same approach used by Walrafen to describe the low frequency Raman scattering of liquid water. In this approach the glitch in the orientational correlation functions is taken to reflect the librational motion of the central molecule in the cage and can therefore be linked to the prominent librational features which appear in both the infrared and Raman spectra. In contrast, the exponential regime is associated with the structural breakup of the cage. The rate of decay largely determines the NMR relaxation time and its smooth character accounts for the simplicity of the dielectric dispersion in the microwave region[86].

In Figure 5-27 the l=2 autocorrelation functions for the bulk water simulations at 288 K are plotted for the molecule-fixed x, y and z directions. The three functions have the same general shape and the position of the glitch is nearly the same in every case, in fact the y and z functions are nearly identical.

Orientational correlation functions such as these were fit to an exponential at large t (0.8 to 1.5 ps) from which an estimate of the reorientational relaxation time is obtained. These have been tabulated (Table 5-3) along with calculated self-diffusion coefficients which were obtained by monitoring the displacement of a labelled atom i as a function of time, averaging over all atoms and all choices of time origin, and exploiting the Einstein relation

$$6D = \lim_{t\to\infty} \frac{d}{dt} \langle | \mathbf{R}_i(t) - \mathbf{R}_i(0) |^2 \rangle \qquad [5\text{-}4]$$

The agreement with experimental data is only fair, the calculated reorientation times are consistently high but their temperature dependence is relatively good.

The peaks which appear in the calculated Raman spectra at frequencies greater than about 300 cm^{-1} arise from the same physical processes which lead to the glitch in the orientational correlation function. These features are in good agreement with experiment in several respects. First, the peak positions are almost independent of temperature. Experimentally, this observation has led to the suggestion that liquid water contains clusters of well-defined structure.

However, they may be associated with short lived features in the orientational correlation function.

Secondly, the decrease in intensity of the bands with temperature increase is in semi-quantitative agreement with experiment. This reflects the fact that the depth of the glitch decreases as the temperature rises because the cage surrounding a given molecule relaxes more rapidly at high temperatures.

The suggestion that the low frequence Raman scattering of liquid may indicate well defined water clusters has been developed by Walrafen[87]. Figure 5-28, modified from his discussion, displays a five-molecule, fully hydrogen-bonded structure taken from the ice I_h lattice. The overall symmetry of the structure is C_2. However, in terms of the central oxygen atoms, the tetrahedral nearest-neighbor oxygen atoms, and the four intervening protons, the symmetry is C_{2v}. Then the symmetry may be described as intermolecular C_{2v} symmetry, provided the conformations of the outer protons are excluded.

In this model nine intermolecular vibrations must be considered, the intermolecular vibrations being excluded. Of these, six refer to restricted translations and three to restricted rotations, i.e., librations.

Two of the six restricted translations are equivalent to the hydrogen bond bending motions. They are the totally symmetric deformations belonging to the A_1 vibrational species and are designated ν_3A_1 and ν_4A_1. The remaining four restricted translations, hydrogen bond stretching motions, involve the A_1, B_1, and B_2 vibrational species and are designated ν_1A_1, ν_2A_1, ν_7B_1, and ν_9B_2. The hydrogen bond bending vibrations ν_3A_1 and ν_4A_1 are unresolved and occur near 60 cm^{-1}; the hydrogen bond stretching vibrations ν_1A_1, ν_2A_1, ν_7B_1, and ν_9B_2 are also unresolved and give rise to the broad band centered near 170 cm^{-1} for liquid H_2O.

The restricted rotational components include one designated ν_5A_2 which involves the restricted rotation that is symmetric only with respect to the C_2 axis. It is forbidden in all dipolar spectra, namely infrared and β_1 hyper-Raman spectra. The band designated ν_8B_2 is assigned to the libration that is symmetric with respect to the plane formed by the atoms of the central H_2O molecule of figure 5-28. That plane is arbitrarily designated B_2. The remaining libration, designated ν_9B_1 is symmetric only with respect to the B_1 plane (perpendicular to the B_2 plane and passing through the C_2 axis). Because none of the librations is totally symmetric to all symmetric elements (C_2, B_1, B_2), each is completely depolarized in the Raman spectrum for C_{2v} symmetry.

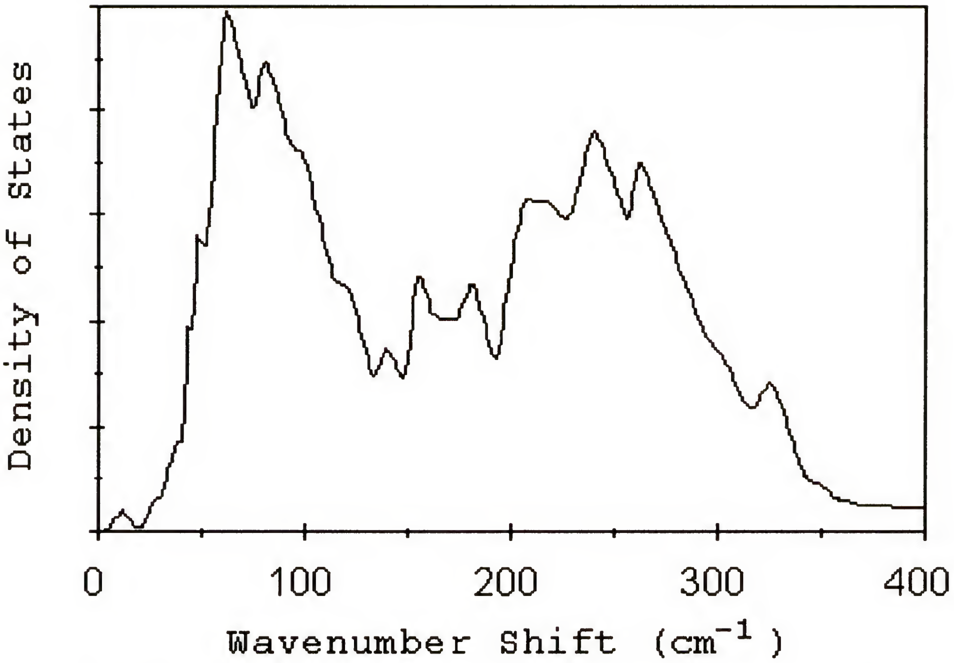

Figure 5-20. Power spectrum of water oxygen atoms obtained from simulated ethylene oxide hydrate.

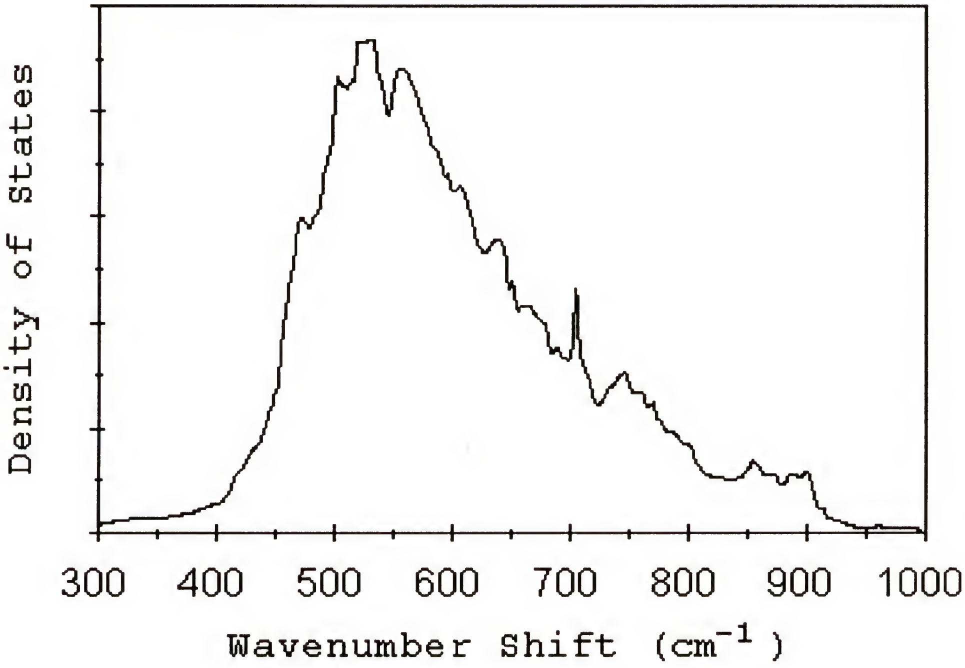

Figure 5-21. Power spectrum of water hydrogen atoms obtained from simulated ethylene oxide hydrate.

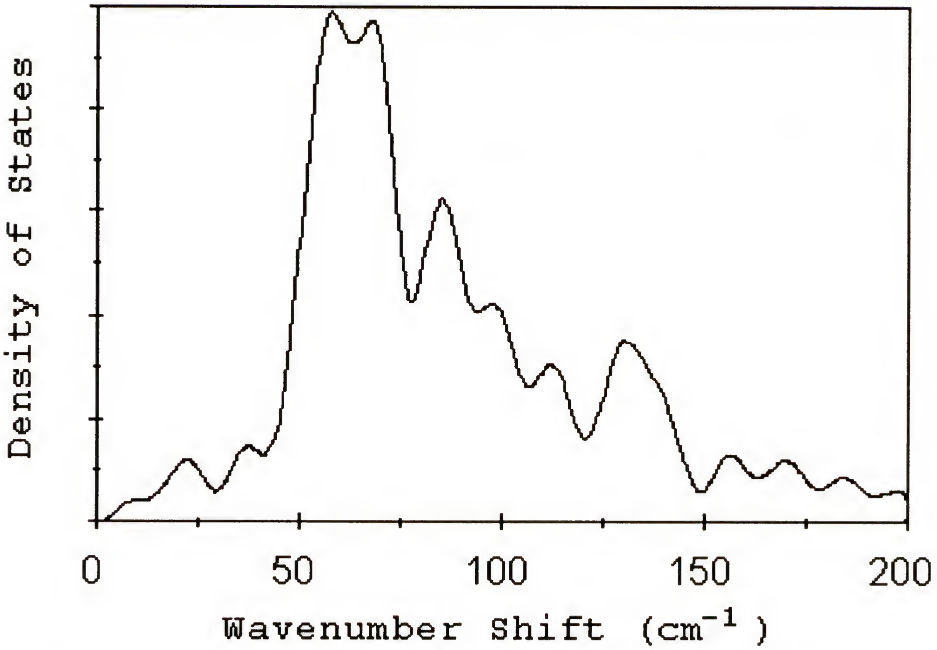

Figure 5-22. Power spectrum of ethylene oxide translational motion obtained from simulated hydrate.

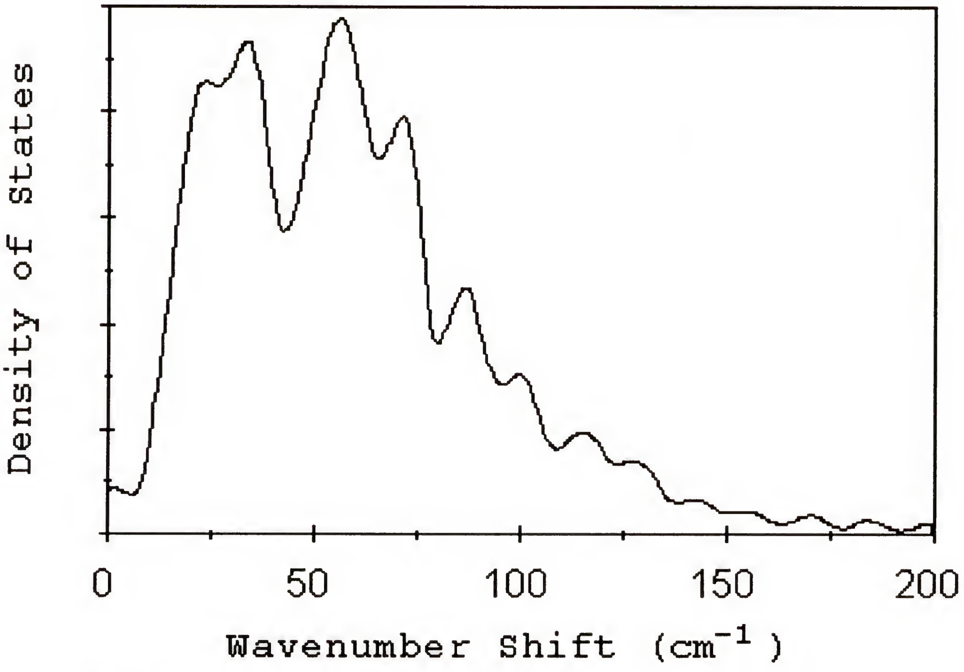

Figure 5-23. Power spectrum of ethylene oxide libration obtained from simulated hydrate.

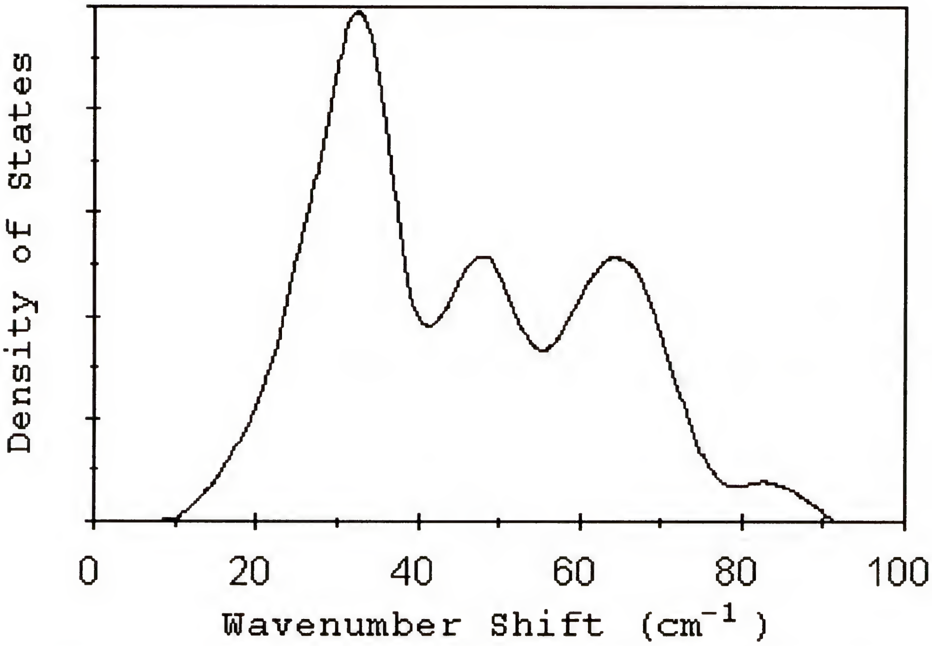

Figure 5-24. Power spectrum of methane translation obtained from simulated hydrate.

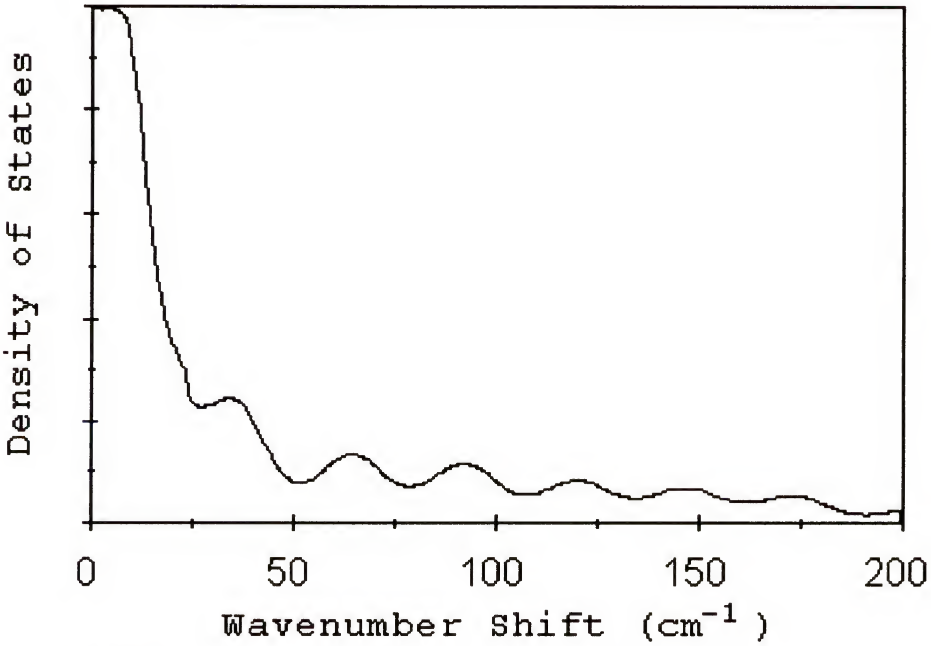

Figure 5-25. Power spectrum of methane libration obtained from simulated hydrate.

For liquid H_2O the ν_5A_2 librations are centered near 450 cm^{-1}, the ν_6B_1 librations are centered near 750 cm^{-1}, and the ν_8B_2 librations are centered near 550 cm^{-1}.

The structure is useful in making vibrational assignments, but it necessarily refers to an average configuration. Distortions from C_{2v} symmetry involving angles and distances are present in those molecules of the real liquid that are involved in the fully hydrogen-bonded structures, and these various distortions give rise to the breadth observed for the individual intermolecular components. Distortions are also present in the partially hydrogen-bonded structures.

A second, and even more significant, weakness in this approach is that it cannot be readily extended to solutions containing components in addition to water. This is particularly true for the systems considered here since even in the solid phase they contain unit cells that are rather large.

Quantitative analysis of the experimental low frequency Raman spectra is made problematic by the high noise levels and the broad background due to Rayleigh scattering and stray light. The spectra calculated from the simulations contain broad unresolved features which may not necessarily have well-defined Gaussian or Lorentzian profiles.

However, it is possible to take advantage of the clear break that occurs between the water translational and librational regions of the spectra. Thus, the following procedure was adopted: calculated and experimental spectra were decomposed into the minimum number of Gaussian components required to achieve a fit having a χ^2 value comparable to that obtained for the experimental water spectra; the "peaks" were then classified as belonging to the water translational or librational region according to whether they were centered above or below the break in intensity found in each spectrum. The integrated intensities are reported as a percentage of the total, excluding background contributions, in Table 5-3.

This classification is is not meant to indicate the physical origin of specific spectral components, since guest librations generally appear in the same spectral region as water translations, for example. More importantly, the DID model presupposses that the relevant polarizability fluctuations are due to motions involving several molecules so it is not physically meaningful to assign individual features to specific types of motion performed by specific molecules.

Recomendations for Further Study

Agreement between the experimental and computational results is semi-quantitative. This should not be taken for granted since the temperatures are low and the systems include light atoms; so that quantum effects should be non-negligible. There are a number of ways in which the experimental and computational aspects of these studies can be improved and extended.

The low water solubility of most clathrate hydrate guests presents a challenge to the experimentalists. Clathrate formation typically begins at the gas-liquid interface, but that interface is much more efficient at scattering light than the microscopic hydrate nuclei and thus is an important source of noise in the experimental spectra. Overcoming this difficulty would require a redesign of the scattering cell. Similarly, Raman studies of solids are best performed with a cell that rotates rapidly such that mesoscopic anisotropies are averaged and this would also require a redesign of the scattering cell.

The experimental studies reported here were obtained using a traditional monochrometer that scans through the wavelength range of interest. This is a slow process and the resulting spectra must be considered those of systems at equilibrium. A study directly addressing the kinetics of hydrate formation would require use of the much faster Fourier transform method of Raman spectroscopy. Fourier transform Raman instruments also typically yield spectra of higher resolution than available from the apparatus used here.

The SPC force field used to model water is as good or better than any of the other available effective-pair potentials for rigid water molecules. This is also the case for the intermolecular potentials used to model the guests. Only marginal improvement can be expected from models that permit intra-molecular bond flexibility since the temperatures are low, and the time-scales for intra-molecular vibrations in the guests modeled here are very fast. Furthermore, the DID model underlying the spectral calculations is appropriate only in the classical limit.

These models can be significantly improved upon only by incorporating many-body or quantum effects. There is currently a great deal of interest in incorporating many-body effects in molecular dynamics or Monte Carlo simulations of water and aqueous solutions. Inclusion of explicit three-body terms in the potential function was proposed by Wojcik and Clementi[87], though it is rather cumbersome to evaluate and parametrize the potential. Early attempts to include non-additive effects via a polarizability, required the use of a time consuming interative procedure for determining the induced dipole moments, which depend on each other in a non-linear fashion[88].

Wallqvist et al[89] modified the SPC rigid water model by adding a point polarizability and developed a new algorithm for calculating the induced dipole moments based on a predictive, instead of an iterative scheme. This study confirmed the importance of many-body effects, particularly with respect to the description of rotational dynamics, but did not significantly improve the description of the structure or internal energy of bulk water systems.

Van Belle et al[90] also started with the SPC model and applied the extended Lagrangian method to incorporate induced polarization effects in molecular dynamics simulations of pure water. The induced dipole on each molecule is treated as an additional degree of freedom and the Lagrangian of the system is extended with a fictitious kinetic term associated with this extra variable. Their study confirmed a significant improvement in the description of dynamical properties is obtained by using a polarizable model, and they developed an algorithm that requires less than twice the time as what is required by an equivalent non-polarizable system.

Work on improving the treatment of many-body effects is ongoing, and, to date, no polarizable water model has been used to calculate the Raman spectrum of water or any aqueous solution.

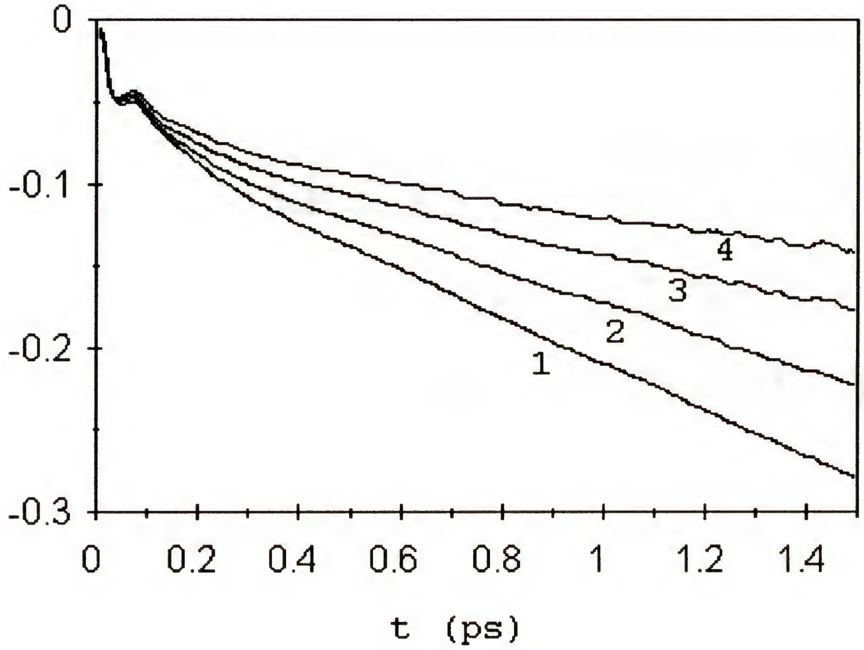

Figure 5-26. The functions $[l(l + 1)]^{-1} \ln C_l^x(t)$ for the bulk water simulation at 288 K and the values of l indicated.

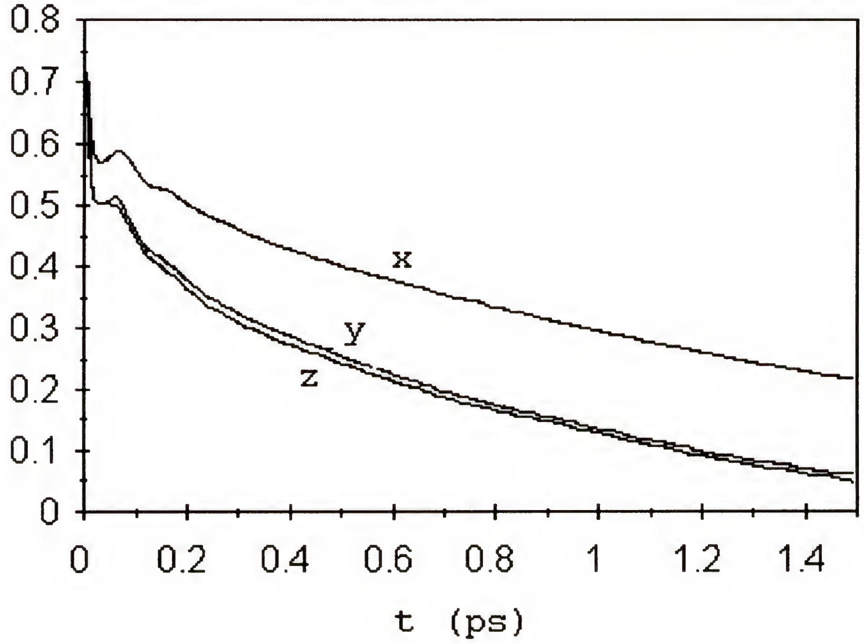

Figure 5-27. The functions $C2^x(t)$, $C2^y(t)$, $C2^z(t)$ for bulk water simulation at 288 K.

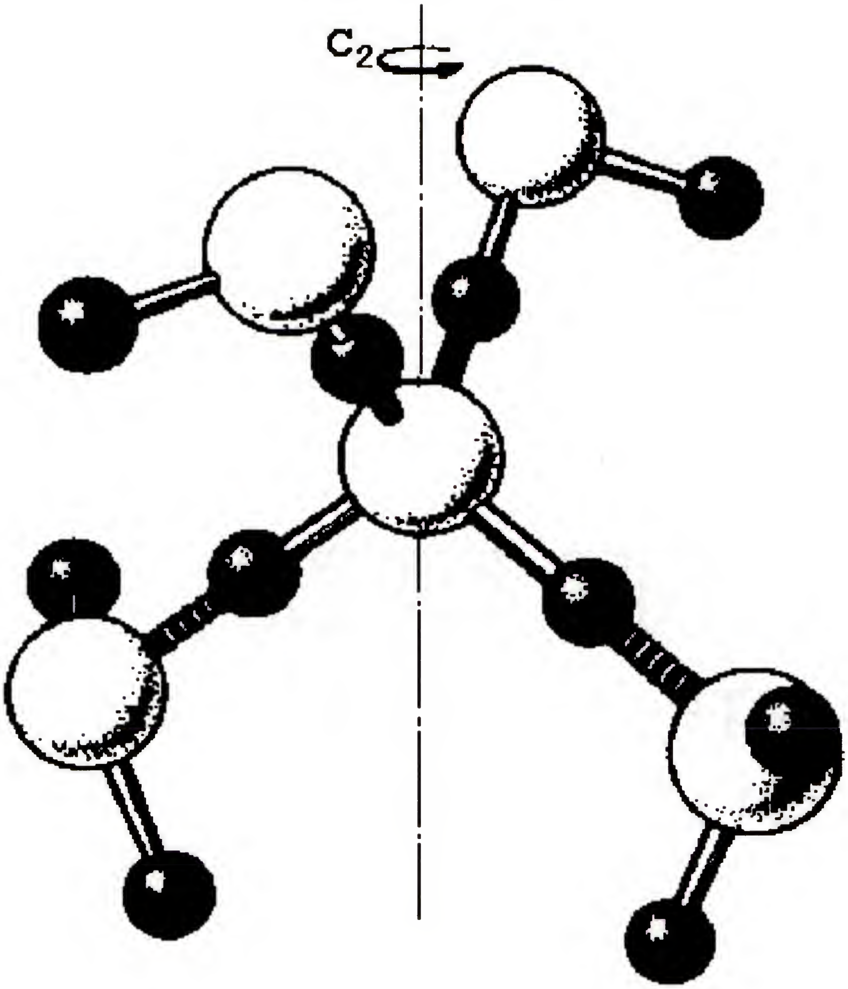

Figure 5-28. Five-molecule, fully hydrogen-bonded structure having intermolecular C_{2v} symmetry. Discs refer to hydrogen bonds. Modified from reference 73.

Table 5-3. Transport Properties

Experimental Water Self-Diffusion Coefficients and Rotational Relaxation Times

T /K	**D /10^{-9} m^2 s^{-1}**	**τ /ps**	**Reference**
259		8.0	58
298	2.3		59
300		5.0	60
350		0.9	60
363		0.9	61

Water Self-Diffusion Coefficients and Rotational Relaxation Times Calculated from Bulk Water Simulations

T /K	**D /10^{-9} m^2 s^{-1}**	**τ /ps**
255	3.8	12.8
288	4.1	6.2
298	4.3	5.0
350	4.6	2.0

Water self-diffusion coefficients and rotational relaxation times calculated from ethylene oxide/ water simulations

T /K	**D /10^{-9} m^2 s^{-1}**	**τ /ps**
290	3.8	10.1
299	4.1	6.5
312	4.3	5.4
330	4.6	3.0

Water self-diffusion coefficients and rotational relaxation times calculated from methane/ water simulations

T /K	**D /10^{-9} m^2 s^{-1}**	**τ /ps**
288	3.8	7.3
300	4.1	6.8
311	4.3	4.1
328	4.6	3.5

Ethylene oxide self-diffusion coefficients and rotational relaxation times calculated from simulations

T /K	**D /10^{-9} m^2 s^{-1}**	**τ /ps**
288	3.8	6.0
300	4.1	8.4
311	4.3	7.1
328	4.6	4.3

Table 5-4. Integrated intensity below translational/ librational break in depolarized spectra. Peported as percentage of total low frequency depolarized integrated intensity excluding background.

T /K	Water experiment	THF/Water experiment	Water simulation	ethylene oxide/ water simulation	Methane/ water simulation
255			32.33		
273	33.52	35.80			
275	29.95	35.41			
277	29.44	34.83			
279	28.94	31.87			
281	28.92	29.32			
283	27.94	28.89			
288	27.24	30.38	31.21		29.11
290				26.81	
291	25.93	28.15			
293	25.43	26.45			
298	24.66	24.71	25.90		
299				24.61	
300					24.10
311					23.22
312				19.18	
328				15.90	20.31
330					
350			12.29		

REFERENCES

1. Sloan, E.D. Jr., "Clathrate Hydrates of Natural Gases," Marcel Dekker Inc., New York, 1990.

2. Hammerschmidt, E.G., Ind. Eng. Chem., **26** (1934) 851.

3. Kvenvolden, K.A., Chemical Geology, **71**, (1988) 41.

4. Makogen, Y.F., Natural Gas Hydrates: The State of Study in the USSR and Perspectives for Its Use, paper presented at the Third Chemical Congress of North America, Toronto, Canada, June 5-10, 1988.

5. Powell, H.M., J. Chem. Soc. (London), **41** (1948) 61.

6. Davidson, D.W., "Clathrate Hydrates," in Water: A Comprehensive Treatise, Vol. 2, Chapter 3, Plenum, New York, (1973) p. 115.

7. Sloan, *Op. Cit.*

8. Stackelberg, M. von, and Muller, H.R., J. Chem. Phys. **19** (1951) 1319.

9. Ripmeester, J. A., Tse, J.S., Ratcliffe, C.I., and Powell, B.M, Nature, **325** (1987) 135.

10. B. Kamb, in "Structural Chemistry and Molecular Biology, Rich, A. and Davidson, N. eds, p. 507, Freeman, SanFrancisco (1968).

11. Davidson, D.W., *Op.Cit.*

12. Bjerrum, N., Science, **115** (1952) 385.

13. Mak, T.C.W., J. Chem. Phys., **43**, 2799 (1965).

    Mak, T.C.W., and McMullan, R.K.,J. Chem. Phys. **42**, 2732 (1965).

14. Davidson, D.W., *Op. Cit.*

15. Maas, O., and Boomer, E.H., J. Am. Chem. Soc. **44**, 1709 (1922).

16. Stackelberg, M. von, *Op. Cit.*

17. Davy, H., Phil. Trans. Roy. Soc. (London) **101**, 1, 1811.

18. Sloan, *Op. Cit.*

19. van der Waals, J.H., Disc. Faraday Soc. **15**, 261 (1953).

van der Waals, J.H., Trans. Faraday Soc. **52**, 184 (1956).

van der Waals, J.H. and Platteeuw, J.C., "Clathrate Solutions," Adv. Chem. Phys. Vol 2, p.1 (1959).

20. van der Waals, J.H. and Platteeuw, J.C., Mol. Phys. **1**, 91 (1958).

21. Onsager, L. and Runnels, L.K. J. Chem. Phys. **50**, 1089 (1969).

Haas, C., Phys. Letters, **3**, 126 (1962).

22. Auty, R.P. and Cole, R.H. J. Chem. Phys., **20**, 1309 (1952).

23. Bjerrum, *Op. Cit.*

24. Venkateswaran, A., Easterfield, J. and Davidson, D.W., Can. J. Chem. **45**, 884 (1967).

25. Davidson, D.W. and Ripmeester, J.A., in Inclusion Compounds, Vol 3, Chapter 3., Atwood, J.L., Davies, J.E.D. and MacNichol, D.D., eds., Academic Press, 1984.

26. Sloan, *Op. Cit.*

27. Davidson, *Op. Cit.*

28. Davidson, D.W., Davies, M. and Williams, K. J. Chem. Phys. **40**, 3449 (1964).

29. Christiansen, R.L., Sloan, E.D., Annals of New York

Academy of Sciences, **715**, 168 (1994).

30. Sloan, *Op. Cit.*

31. Sloan, *Op. Cit.*

32. Bertie, J.E., Jacobs, S.M., Can. J. Chem., **78**, 6430 (1983)

33. Impey, R.W., Madden, P.A., and McDonald, I.R., Mol. Phys., **46**, 513 (1982).

34. Marchi, M., Tse, J.S., Klein, M.L., J. Chem. Phys., **85**, 2414 (1986).

    Tse, J.S., Klein, M.L., McDonald, I.R., J. Chem. Phys., **81**, 6124 (1984).

35. There are many such studies, those relied upon most heavily include:

    Walrafen, G.E., "Raman and Infrared Spectral Investigations of Water Structure", in Water: A Comprehensive Treatise, Vol. 1, Chapter 5, Plenum, New York, (1972) p. 151.

    Rousset, J.L., Duval, E., Boukenter, A., J. Chem. Phys. **92**, 2150 (1990).

    Yeh, Y., Bilgram, J.H., Kanzig, W., J. Chem. Phys. **77**, 2317 (1982).

    Mizouguchi, K., Hori, Y., Tominaga, V., J. Chem. Phys. **97**, 1961 (1992).

    Mazzacurati, V., Nucara, A.,Ricci, M.A., Ruocco, G., Signorelli, G., J. Chem. Phys. **93**, 7767 (1990).

    Fontana, A., Nardone, M., Ricci, M.A., J. Chem. Phys. , **102** 6975 (1995).

    Madden, P.A., Impey, R.W., Chem. Phys. Lett. , **123**, 502 (1986).

    Brooker, M.H., Hancock, G., Rice, B.C., Shapter,J., J. Raman Spec., **20** 683 (1989).

36. Johari, G.P., Chew, H.A.M., Nature, **330**, 604 (1983).

Johari, G.P., Chew, H.A.M., Phil. Mag., **49** (1984) 281.

37. Szymanski, P.P., ed., "Raman Spectroscopy", Plenum Press, New York (1967).

38. McQuarrie, D.A., "Statistical Mechanics", Harper and Row, New York, N.Y. (1976), p. 476.

39. Wang, C.H., "Spectroscopy of Condensed Media", Academic Press, 1985.

Rothschild, W.G., "Dynamics of Molecular Liquids," J. Wiley, New York, N.Y. (1984).

40. C.H. Wang, *Op.Cit.*

Wilson, E.B.,Jr., Decius, J.C., Cross, P.C., "Molecular Vibrations: The Theory of Infrared and Raman Vibrational Spectra", Dover Publications, New York, N.Y., 1955.

Gordon, R.G., Adv. Mag. Resonance, **3**, (1968) 1.

41. Berne, B.J., Pecora, R., "Dynamic Light Scattering", Krieger, Malabar, Fl. (1990), Chapters 2 and 3.

42. *ibid*, Chapter 5.

43. *ibid*, Chapter 7.

44. *ibid*, Chapter 14.

45. Wang, *Op. Cit.*, Wilson, et. al. *Op.Cit.*

46. Yarwood, J., Arndt, R., in "Molecular Association", R. Foster, Ed., Academic Press, 1979, p. 267.

Jonas, J., Lee, Y.T., J. Phys. Condens. Matter, **3**, 305 (1991).

Perova, T.S., Adv. Chem. Phys. **87**, 427 (1994).

47. Buckingham, A.D., Adv. Chem. Phys., **12**, 107 (1967).

48. Murphy, W.F., Brooker, M.H., Nielsen, O.F., Praestgaard, E., Bertie, J.E., J. Raman Spec., **20**, 695

(1989).

Nielsen, O.F., Ann. Rep. Prog. Chem. Sect. Phys. Chem., **90**, 3 (1993).

49. Ponder, J.W., information and code distribution obtained from the world wide web at http://dasher.wustl.edu/tinker.

50. Allen, M.P., Tildesley, D.J., "Computer Simulation of Liquids", Clarendon Press, 1987.

51. Berendsen, H.J.C., Postma, J.P.M., van Gusteren, W.F., Herman, J., in "Intermolecular Forces", ed., Pullman, B., Reidel (Dordrecht), 1987.

52. Tse, J.S., Klein, M.L., McDonald, I.R., J. Chem. Phys.,**81**, 6124 (1984).

53. Tse, J.S., Klein, M.L., McDonald, I.R., J. Phys. Chem., **87**, 4198 (1983).

54. Tse, J.S., Klein, M.L., McDonald, I.R., J. Chem. Phys.,**81**, 6146 (1984).

55. McMullan, R.K., Jeffrey, G.A., J. Chem. Phys., 42, 2725 (1965).

    Jeffrey, G.A., Hollander, F., J. Chem. Phys., **66**, 4699 (1977).

56. Neder, R.B., Proffen, T., J. Appl. Cryst., **30**,171 (1997). The source code and more information is available on the world wide web at http://www.kri.physik.uni-muenchen.de /crystal/ discus/discus.html

57. Bernal, J.D., Fowler, R.H., J. Chem. Phys., **7**, 515 (1933).

58. Benassi,P., Mazzacurati, V., Nardone, M., Ricci, M.A., Ruocco, G., DeSantis, A., Frattini, R., Sampoli, M., Mol. Phys., **62** 1467 (1987).

    Ricci, M.A., Ruocco, G., Sampoli, M., Mol. Phys., **67**, 19 (1989).

59. Huiszoon, C., Mol. Phys., **58**, 865 (1986).

60. Murphy, W.F., J. Chem. Phys., **67**, 5877 (1977).

61. Bosma, W.B., Fried, L.E., Mukamel, S., J. Chem. Phys., **98** 4413 (1993).

62. Gray, C.G., Gubbins, K.E., "Theory of Molecular Fluids", Vol. 1., Fundamentals, Clarenden Press, 1984.

63. Bongard, M.P., Buckingham, A.D., Ritchie, G.L.D., Chem. Phys. Lett., **90**, 183 (1982).

64. De Lorenzi, A., De Santis, A., Frattini, R., Sampoli, M., Phys. Rev. A., **33**, 3900 (1986).

65. Gray, C.G., Gubbins, K.E., *Op. Cit.*

66. Applequist, J., Carl, J.R., Kwok-Keung, F., J. Am. Chem. Soc. **94** (1972) 2952.

67. J.A. Dean, ed., Lange's Handbook of Chemistry, McGraw-Hill, 1992.

68. Matousek, P., Parker, A.W., Towrie, M., RAL-95-028 (Council for the Central Laboratory of the Research Councils), Oxfordshire, UK. More information and the program itself may be obtained on the world wide web at http://www.nd.rl.ac.uk/lasers/

69. Palmer, A., Bissell, E.R., Spectrochimica Acta, **16**, 450 (1960).

70. Cates, D.A., MacPhail, R.A., J. Phys. Chem., **95**, 2209 (1991).

Bartoli, F.J., Litovitz, T.A., J. Chem. Phys., **56**, 404 (1972).

Tarjus, G., Bratos, S., Mol. Phys., **51**, 793 (1984).

Hills, B.P., Mol. Phys., **53**, 731 (1984).

71. Walrafen, G.E., J. Chem. Phys., **52**, 4176 (1970).

72. Walrafen, G.E., Hokmabadi, M.S., Yang, W.H., J. Phys. Chem., **94**, 2237 (1990).

73. Walrafen, G.E., "Raman and Infrared Spectral Investigations of Water Structure", in Water: A Comprehensive Treatise, Vol. 1, Chapter 5, Plenum, New York, (1972) p. 151.

74. Draegert, D.A., Stone, N.W.B., Curnutte, B., Williams, D., J. Opt. Soc. Am., **56**, 64 (1966).

75. Safford, G.J., Leunt, P.S., Naumann, A.W., Schaffer, P.C., J. Chem. Phys., **50**, 4444 (1969).

76. R. Zwanzig, Annu. Rev. Phys. Chem.,**16**, 97 (1965).

77. Bertie, J.E., Whalley, E., J. Chem. Phys., **67**, 2445 (1997).

78. Renker, K.B., Blanckenhagen, P.V., in "Physics of Ice", Riehl, N., Bullemer, B., Engelhardt, H., Plenum, New York (1969).

79. Walrafen, G.E., J. Chem. Phys., **44**, 1546 (1966).

80. Anaumann, A.W., Safford, G.J., J. Chem. Phys., **47**, 867 (1967).

81. Tse, J.S., Klein, M.L., McDonald, I.R., J. Chem. Phys.,**81**, 6146 (1984).

82. Renker, et al, *Op.Cit.*

83. Bertie, J.E., Jacobs, S.M., Can. J. Chem., **55**, 1977 (1977).

84. Wegener, W., Vanderhaeghen, Hauteder, S., van Gerven, L., Physica B, **95**, 71 (1978).

85. Lynden-Bell, R.M., McDonald, I.R., Mol. Phys., **43**, 1429 (1981).

86. Jonas, J., de Fries, T., Wilbur, D.J., J. Chem. Phys., **65**, 582 (1976).

Hasted, J.B., in "Water: A Comprehensive Treatise", Vol 1, ed. Franks, F., Plenum, 1972.

87. Wojcik, M, Clementi, E., J. Chem. Phys., **84** 5970 (1986).

88. Rullman, J.A.C., Van Duijnen, P.Th., Mol. Phys., **63**, 451 (1988).

89. Ahlstrom, P., Wallqvist, A., Engstrom, S., Jonsson, B., Mol. Phys., **68**, 563 (1989).

90. Van Belle, D., Froeyen, M., Lippens, G., Wodak, S.J., Mol. Phys., **77**, 239 (1992).

BIOGRAPHICAL SKETCH

Ralph Karl Zachary is the son of Ralph Kennish and Caryl Ann Zachary and was born on June 20, 1963. He has answered to "Karl" partly to avoid confusion and partly out of respect to the great economist that he has retroactively chosen as his namesake (Karl Menger). Born in Des Moines, Iowa, he has since had his pronunciation of that much maligned city corrected by residents from nearly 30 states.

Three years later the Zacharys moved from Ankeny, Iowa to Lisbon, North Dakota where they remained for five years. In 1972, the family moved to Cooperstown and, in 1974, Grand Forks, North Dakota. A year and a half later they followed the geese as far as Beresford, South Dakota. In the summer of 1980, they moved to Webb City, Missouri where Karl graduated from high school in May of 1981.

The author then attended Missouri Southern State College in Joplin for two years pursuing an English degree. After some reflection he decided to leave, at least temporarily, the liberal arts world to its fate. He then moved to Arlington, Texas where he completed his B.S. in Chemistry in May of 1991.

He then took the bold step of leaving his home time-zone and moved to Gainesville, Florida where he began graduate school in physical chemistry. After joining the research laboratory of Dr. Samuel Colgate, he studied acoustic techniques for exploring equilibria phenomena and turbulent flow. He then turned to Raman spectroscopy for the investigation of clathrate hydrate formation.

I certify that I have read this study and that in my opinion it conforms to acceptable standards of scholarly presentation and is fully adequate, in scope and quality, as a thesis for the degree of Doctor of Philosophy.

Samuel O. Colgate

Samuel O. Colgate, Chair
Professor of Chemistry

I certify that I have read this study and that in my opinion it conforms to acceptable standards of scholarly presentation and is fully adequate, in scope and quality, as a dissertation for the degree of Doctor of Philosophy.

David A. Micha
Professor of Chemistry

I certify that I have read this study and that in my opinion it conforms to acceptable standards of scholarly presentation and is fully adequate, in scope and quality, as a dissertation for the degree of Doctor of Philosophy.

Yngve N. Öhrn
Professor of Chemistry

I certify that I have read this study and that in my opinion it conforms to acceptable standards of scholarly presentation and is fully adequate, in scope and quality, as a dissertation for the degree of Doctor of Philosophy.

John R. Reynolds
Professor of Chemistry

I certify that I have read this study and that in my opinion it conforms to acceptable standards of scholarly presentation and is fully adequate, in scope and quality, as a dissertation for the degree of Doctor of Philosophy.

David

David Groisser
Associate Professor of
Mathematics

This dissertation was submitted to the Graduate Faculty of the Department of Chemistry, to the College of Liberal Arts and Sciences, and to the Graduate School and was accepted as partial fulfillment of the requirements for the degree of Doctor of Philosophy.

May, 1998

Dean, Graduate School